

# Progress in Surface Science

An International Review Journal

EDITOR: Professor Sydney G. Davison

<b>Obituary Erwin W. Mueller</b>	<b>i</b>
<b>T. T. TSONG</b>	
<b>Imaging atom-probe mass spectroscopy</b>	<b>219</b>
<b>J. A. PANITZ</b>	
<b>Errata</b>	<b>263</b>

ISSN 0079-6816

PSSFBP 8(6) 219-264 (1978)



**PERGAMON PRESS** Oxford · New York



Erwin W. Mueller with his energy focused time-of-flight Atom-Probe Field Ion Microscope.

## OBITUARY

### ERWIN W. MUELLER, HIS LIFE AND HIS WORK

Erwin W. Mueller, one of the earliest pioneers in surface science and the first man to see atoms as the building blocks of solid surfaces, was born on June 13, 1911 in Berlin, Germany. He studied physics at the Technical University in Berlin under Nobel Laureate Gustav Hertz, and obtained his doctoral degree in 1936. His habilitation was granted by the same university in 1950.

Mueller conceived the idea of the field emission microscope shortly after receiving his doctoral degree. The microscope enabled him to image the surface of submicroscopic metal tips with a resolution of about 20 Å. For the first time, diffusion and rearrangement of surface layers could be vividly seen. At that time, dynamical theories of various atomic processes on solid surfaces were just being developed. Thus, the direct observation made possible with the field emission microscope had a

great impact on the further development of these theories. In 1941, he discovered field desorption-evaporation of surface atoms at cryogenic temperatures by application of a high positive electric field.

Mueller's research work, greatly hampered by the Second World War, was completely halted at the end of the war. He worked between 1945 and 1947 as a high school teacher. Those were hard years, even for a creative scientist. To keep his family from starving, he made baking powder from gravestones and bartered this for flour from local farmers.

In 1948, Mueller was offered a position at the Fritz-Haber Institute of the Max-Planck Society in Berlin. There he could again pursue scientific work and his great desire of achieving atomic resolution of the Field Emission Microscope (FEM). There is, however, an intrinsic limit to the resolution of this microscope. Since the field emitted electrons originate near the Fermi level, their kinetic energies are comparable to the Fermi energy of the metal. This large kinetic energy limits the resolution of the FEM to about 20 Å. To overcome this limitation, he investigated the possibility of imaging surface atoms by adsorption and subsequent field desorption of gas atoms from the field emitter surface. This work led to his invention of the Field Ion Microscope (FIM) in 1951. The original Field Ion Microscope used hydrogen as an imaging gas and was operated at room temperature. Although the resolution was improved significantly, true atomic resolution was not yet achieved.

In 1952, he was invited by the U.S. Army Joint Chief of Staffs for a lecture tour in the United States. After presenting an inspiring colloquium to the physics department of The Pennsylvania State University, he was invited to stay as a professor.

At Penn State he explored the origins of the physical processes involved in the FIM and developed most of the techniques used today in field ion microscopy. In 1955, he achieved atomic resolution of the FIM by cryogenic cooling of the specimen. This achievement made him world famous as the first man to "see" atoms.

The FIM, while providing the atomic images of a solid surface, cannot ascertain the chemical identity of the atoms. To achieve this aim, he ingeniously combined an FIM with a time-of-flight mass spectrometer. The resulting instrument, known as the Atom-Probe Field Ion Microscope, is the most sensitive analytical tool in existence, being capable of analyzing a single atom. It thus opens up a whole new dimension in field ion microscopy.

Mueller's Field Emission Microscope, Field Ion Microscope and Atom-Probe Field Ion Microscope have been widely employed in surface and metallurgical investigations continuously for over four decades. Many modern experiments are carried out in atomic details unimagined possible before. The scope and impact of his work are not confined to these inventions, but extend also to many fundamental areas of surface science.

His work was appreciated by experts and non-experts alike. His beautiful field ion micrographs have been used in hundreds of elementary textbooks published around the world for both scientific illustrations and aesthetic attractions.

Mueller's vast scientific contributions are incorporated in his more than 200 papers, two books and many book chapters. His achievements were recognized by the scientific community with numerous awards, such as the Davison-Germer Prize of the American Physical Society, the first Medard N. Welch Gold Medal of the American Vacuum Society and the Gauss Medal of Germany. He was an elected and honorary member of many scientific societies, such as the National Academy of Sciences, National Academy of Engineering, Deutschen Akademie der Naturforscher, Leopoldina, and the Honorary President of the International Field Emission Symposium. In addition, he held two honorable doctoral degrees, one from the Free University of Berlin and one from the Claude-Bernard University of Lyon. He was awarded a National Medal of Science posthumously from President Carter in November, 1977.

Although Mueller retired from an Evan Pugh Research Professorship at the University in July, 1976, he was still active in research with undiminished energy,

when unexpectedly he suffered a stroke in April, 1977. On May 17, 1977 he died. Tragically, his wife Klara Mueller died two and a half months later, also by a stroke. It was a great shock to their many friends, his colleagues, and a great loss to the scientific community. Erwin Mueller will long be remembered for his energetic drive, stimulating and persuading personality, and most of all for his extraordinary scientific contributions.

T. T. Tsong  
Department of Physics  
The Pennsylvania State University

# IMAGING ATOM-PROBE MASS SPECTROSCOPY†

J. A. PANITZ

*Sandia Laboratories, Albuquerque, New Mexico 87115, U.S.A.*

## Contents

Forward	219
1. Introduction	219
2. Instrumentation	221
A. Basic principles	221
B. Vacuum system	222
C. Tip-to-detector distance	224
D. Desorption pulse considerations	225
E. Desorption pulse transmission	227
F. Desorption pulse generation	229
G. Desorption pulse measurement	230
H. Detector configuration	231
I. Detector efficiency	232
J. Time-gating the detector	234
K. Detector amplifier	236
L. Timing considerations	237
3. Mass Spectroscopy of Surface Species	238
A. Species identification	238
B. Time-of-flight measurements	240
C. "First layer" composition	241
D. Composition of one atomic layer	241
E. Average composition of the near surface region	243
4. Field Desorption Imaging	243
A. Image resolution	243
B. Time-gated imaging	246
5. Depth Profile Analysis	253
6. Future Applications	259
References	261

**Abstract**—Surface properties of metallic solids are of great technological interest. Their influence is felt in areas as diverse as catalysis, corrosion and the plasma stability in magnetic-confinement fusion reactors. In this paper a new surface analytic capability is reviewed which can provide a unique picture of a metallic surface by directly imaging, in atomic resolution, the spatial distribution of its constituent species and their depth distribution within the near surface region. After thoroughly reviewing the experimental technique and emphasizing design parameters and constraints, the analytic capabilities and limitations of the technique are discussed in detail. Examples are given of surface and near surface compositional analysis and the ability to obtain angstrom resolved depth profiles of implanted species having energies less than 100 eV. Although essentially a research technique requiring special sample preparation, the anticipated practical applications of Imaging Atom-Probe Mass Spectroscopy are numerous, ranging from metallurgical studies of grain boundary segregation and pre-precipitate clustering in alloys, to the direct imaging of constituent atoms within large, biologically active molecules.

## Forward

The author would like to dedicate this review to the memory of his thesis advisor, the late Erwin W. Müller, who pioneered the development of the techniques of field-ion microscopy and atom-probe field-ion mass spectroscopy upon which the Imaging-Atom-Probe technique is based. Those of us who worked with Erwin were always impressed by his knowledge, insight, creativity, experimental

ability, and unrelenting enthusiasm for an area of scientific inquiry which he founded, promoted, and contributed to substantially, throughout his long and productive career.

## 1. Introduction

Surface properties of metallic solids are currently of great interest, not only because the processes of adsorption, migration and diffusion are inherently interesting, but because the first few atomic layers of a solid form a barrier between the bulk of a material and an often hostile environment. This fact has far reaching consequences

†This work was supported by the U.S. Energy Research and Development Administration (ERDA) under Contract AT(29-1)789.

linking such diverse practical problems as the stability of the vacuum chamber wall in fusion reactors, and the corrosion resistance of steel alloys. In some cases (catalysis is an example) the surface may even assume prime importance with the bulk of the material merely serving as a support for those first atomic layers which interact with the ambient environment to produce beneficial products.

The practical importance of surface related problems has recently translated into a desire to characterize, as completely as possible, the composition and structure of a surface, its morphology, and the depth distribution of species within the near surface region of the bulk. As a result, a plethora of analytical techniques have been introduced in the last few years to study the surface properties of metallic solids. The commercial availability of analytical instruments, such as Auger spectrometers, has greatly encouraged world-wide study of surface processes while establishing performance levels which have promoted reproducible results. However, a particular class of analytical instruments has been almost neglected in the rush to apply as many conceivable techniques as possible to the study of surface phenomena. These are the instruments based on the atomic resolution of the low temperature Field-Ion Microscope,<sup>(1)</sup> and the physical processes of field desorption<sup>(2)</sup> and field evaporation<sup>(1,3)</sup> which can controllably remove surface species of a metallic solid with angstrom precision.

The field desorption process is particularly attractive as the basis of a surface analytical instrument, because it acts only on the first atomic layer of a solid, and provides a method to remove surface species whose individual identities, locations and depth profiles within the near surface region can, in principle, be uniquely determined. Unfortunately, the apparatus which can provide such capabilities is not commercially available, so that those groups wishing to apply the technique must design and construct their own instruments. This situation defines a major problem which has been generally associated with the whole area of Field-Ion Microscopy since its inception, and which has discouraged widespread application of its techniques: each research group must, in effect, become instrument designers, builders and "improvers" leaving little time (at least initially) to use their instruments to solve problems of general interest.

It is the intended purpose of this review to attempt to improve this situation by devoting a major portion of the following discussion to a description of the author's Imaging Atom-Probe<sup>(4)</sup> and constraints on its design. The opportunity provided by this review to discuss instrumentation seems timely. The Imaging Atom-Probe technique, introduced by the author in 1973,<sup>(5)</sup> is now beginning to be adopted by other groups, so that a description of the instrumentation should be useful at this time, especially since the detector time

gating<sup>(6,7)</sup> requires careful attention to design parameters, which have not been previously discussed in the literature.

In the following pages, the instrumentation of the Imaging Atom-Probe will be described in detail. First, the vacuum system will be discussed and the concept of a dual-chamber vacuum system introduced. Then the factors affecting the choice of a tip-to-detector distance,  $R$ , will be examined which result in either a "conventional" Atom-Probe,<sup>(8)</sup> or an Imaging Atom-Probe mass spectrometer. Next, the importance of the desorption pulse shape, its generation, and its transmission to the tip will be discussed. This will be followed by a discussion of the imaging detector, its efficiency, and the time-gating procedure. A description of the detector amplifier and a discussion of system timing will conclude the sections on instrumentation.

The remainder of the paper will be divided into four major parts. The first, "Mass Spectroscopy of Surface Species", will discuss three types of measurements which can be made with the Imaging Atom-Probe to determine the composition of the tip. A brief discussion of the effect of the acceleration region in front of the tip on species identification will be included. The second section, "Field-Desorption Imaging", will contain examples of time-gated desorption images. A review of recent theories which attempt to explain variations in ion density observed in multilayer desorption images will be included, as well as a discussion of desorption-image resolution. The next section will deal with depth profile analysis using the Imaging Atom-Probe and the final section, "Future Applications", will discuss those areas in which the author believes the Imaging Atom-Probe can make significant contributions.

The "theory" of the field-desorption process has been excluded from this review, not only because its current status has been discussed in detail in many other places,<sup>(1,9-13)</sup> but also because the theory is still in its infancy.<sup>(12,13)</sup>

## 2. Instrumentation

### A. Basic principles

With the introduction of the Field-Desorption Microscope in 1972,<sup>(14)</sup> imaging of surface species (removed as positive ions during the application of a high electric field) became a practical reality. This occurred despite the fact that the field desorption process was (and still is) not well understood, although it can be pictured as thermal activation of surface species over a field reduced energy barrier.<sup>(15)</sup> Since thermal desorption was, itself, a widely used technique to characterize adsorption states on metallic solids,<sup>(16)</sup> the possibility of reducing the substrate temperature (to minimize species migration) and field desorbing the surface, became attractive as a possible basis for a surface analytic tool. This was particularly true because the sample (or tip) in the desorption

microscope displayed many different crystal facets of unique orientation, so that crystallographic distributions of surface species could, in principle, be directly obtained from the desorption image.

The desorption microscope is similar to its established predecessor, the Field-Ion Microscope, in that a high electric field produced at the surface of a sharply curved specimen is needed for imaging. However, unlike the Field-Ion Microscope which requires a very high field to ionize ambient gas atoms above the surface, the Field Desorption Microscope requires a field sufficient only to ionize and desorb the species of interest from the surface. Practically, this means that weakly adsorbed surface species, which can be easily ionized, should be imageable in the desorption microscope, whereas in the Field-Ion Microscope, they might desorb from the surface well before the imaging field of even hydrogen ( $\approx 2 \text{ V/\AA}$ ) was reached. Furthermore, since the species producing the image in the desorption microscope are equilibrated to the temperature of the tip surface prior to desorption, the spatial resolution of the desorption image should be better than that obtained in the ion microscope at the same tip temperature. This improvement in resolution was qualitatively demonstrated by a comparison between room temperature field-ion and field desorption images of a tungsten substrate when the Field Desorption Microscope was introduced.<sup>(14)</sup>

The first-desorption images obtained by Walko and Müller<sup>(14)</sup> for tungsten necessarily displayed the dominant field evaporating lattice species ( $\text{W}^{3+}$ ), but also had to include image contributions from less abundant  $\text{W}^{4+}$ , impurity atoms in the bulk, and adsorbed residual gas species. The fact that several different species were removed from the surface to form a composite desorption image (in which the individual species were unidentifiable and indistinguishable) made it impossible to use the desorption microscope to determine the crystallographic variation in abundance associated with each desorbing species.

These difficulties were overcome by the Imaging Atom-Probe technique,<sup>(7)</sup> shown in the simplified drawing of Fig. 1. A vacuum system contains the specimen tip, cooled to cryogenic temperatures by conduction from a cryogenic liquid in a cold finger Dewar. A detector, capable of amplifying and displaying the impacts of individual field desorbed ions, is placed a distance  $R$  from the specimen ( $R$  defines a field-free or "drift" region). To create the field required for desorption, a positive d.c. bias,  $V_{dc}$ , and a positive pulse (of amplitude  $V_p$ ) are applied to the tip, desorbing as positive ions species which drift over the distance  $R$  with energy:

$$\frac{1}{2}mv^2 = q(V_{dc} + V_p) = ne(V_{dc} + V_p) \quad (1)$$

where  $m$  is the mass of the desorbed species,  $n$  is

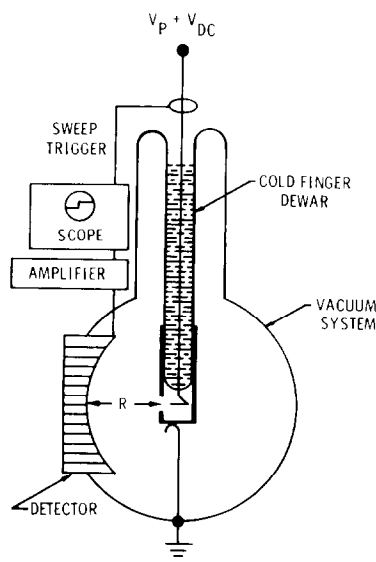


FIG. 1. A simplified schematic drawing of a field-desorption microscope, modified to measure the travel times of field-desorbed species. The specimen tip-to-detector distance,  $R$ , defines a field-free "drift" region for the desorbed species.

its charge state and  $v$  is its velocity at the entrance to the drift region.

Since the drift region is field-free, the ion arrives at the detector at a time  $T$ , where:

$$T = \frac{R}{v} = R \left[ 2e(V_{dc} + V_p) \frac{n}{m} \right]^{-1/2}. \quad (2)$$

If the desorption pulse triggers the sweep of an oscilloscope which displays the arrival of the ion (as an amplified voltage pulse), the ion travel time,  $T$ , can be directly measured. Since the specimen potential is known, the identity (or mass-to-charge ratio,  $m/n$ ) of the desorbed ion can be determined. From (2):

$$\frac{m}{n} = \frac{2e}{R^2} (V_{dc} + V_p) T^2 \quad (3)$$

or

$$\frac{m}{n} = \frac{0.193}{R^2} (V_{dc} + V_p) T^2 \quad (4)$$

where  $V_{dc}$  and  $V_p$  are measured in kilovolts,  $T$  is measured in microseconds, and  $R$  is measured in meters.

Although the identity of the desorbed species can be determined from this simple extension<sup>(5)</sup> of the desorption microscope using the techniques of Atom-Probe Field-Ion Microscopy,<sup>(8)</sup> the detector image will still be a composite of the individual images of all desorbed species. However, (4) predicts that the different species will not arrive

simultaneously at the detector, but sequentially in time (those with the smallest  $m/n$  will arrive first, those with the largest  $m/n$ , last). This simple fact permits the image of a preselected species to be separated from the composite desorption image by a process called "time-gating" in which the detector is activated coincidentally with the arrival of the species of interest.<sup>(6,7)</sup>

### B. Vacuum system

An Imaging Atom-Probe vacuum system is shown in Figs. 2 and 3. The main feature of the system is two isolatable chambers, separately pumped, which permits the specimen to be changed without exposing the detector and cold finger to the atmosphere. Although "quick specimen change" systems are not new (the author saw

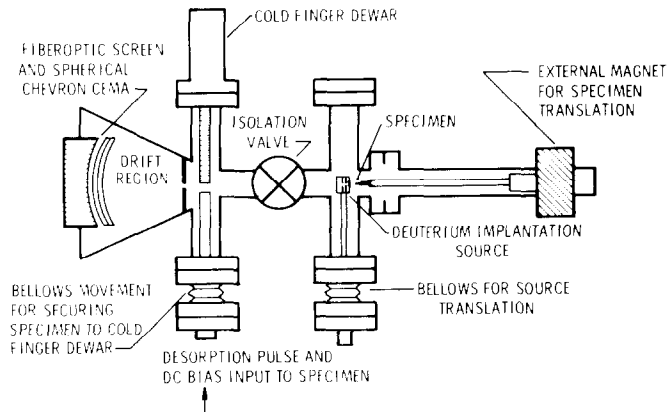


Fig. 2. Schematic diagram of the Imaging Atom-Probe vacuum system, which consists of two separately pumped chambers, isolated by a high vacuum valve.

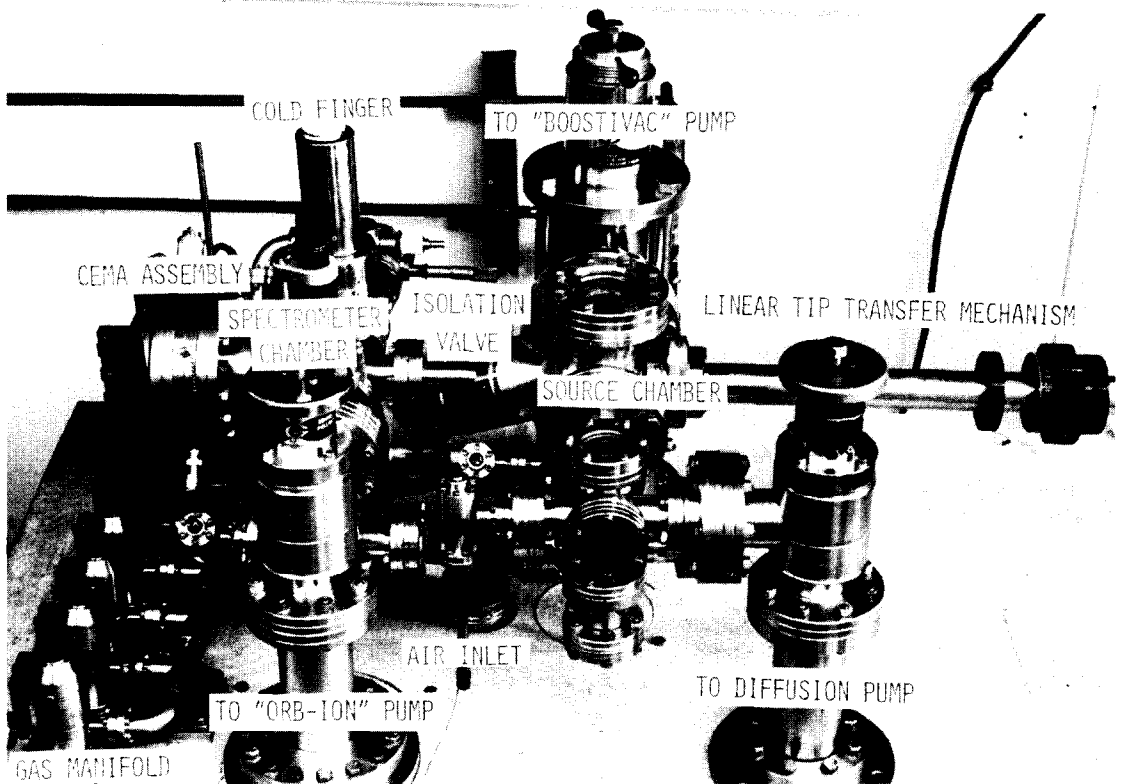


Fig. 3. Photograph of the Imaging Atom-Probe vacuum system of Fig. 1.

the advantages demonstrated by R. Waugh at Cambridge University in 1974), the present version is somewhat unique in that it uses no elastomer seals and provides a working volume in which interaction with the specimen (i.e. gas adsorption or implantation) is possible. As can be seen in Fig. 2, the "spectrometer chamber" contains the specimen "tip", the detector (Chevron CEMA), a high voltage pulse and d.c. bias line. It is pumped by an ionization-sublimation pump to less than  $8 \times 10^{-10}$  Torr which improves to  $4 \times 10^{-10}$  Torr with liquid nitrogen in the cold finger. The second, or "source chamber", is independently pumped by a noble gas ion pump and a double trapped oil diffusion pump. The ultimate pressure in this chamber is  $1 \times 10^{-9}$  Torr which improves to  $4 \times 10^{-10}$  Torr with liquid within 30 min of exposure to atmosphere with no bakeout. A metal-sealed isolation valve separates the spectrometer chamber from the source chamber.

The tip is spotwelded to a 1.5 mm diameter stainless steel rod (10 mm long) which is inserted into a beryllium copper spring finger holder (Fig. 4). This holder, in turn, plugs into a beryllium copper support at the end of a linear transfer rod which is magnetically coupled to the outside of the chamber. Following specimen insertion, the source chamber is evacuated. After pumpout to the desired pressure, the isolation valve is opened, and the linear transfer mechanism used to place the beryllium copper tip holder in contact with the curve bottom of the cold finger. A bellows on the pulse line permits the tip holder to be clamped between the cold finger bottom and the end of the rigid line. Following this operation, the transfer rod is unplugged from the tip support, and withdrawn into the source chamber. Closing the isolation valve completes the transfer procedure. During the 1 min transfer operation, the

spectrometer chamber pressure never rises above  $2 \times 10^{-9}$  Torr, and quickly recovers following the closure of the isolation valve.

Tip heating is accomplished by means of an electron bombardment filament located in the source chamber coaxial with the tip and transfer rod when the latter are withdrawn into the source chamber. Twenty watts of power supplied to the tungsten ribbon filament (biased to  $-5$  kV) easily heats the tip and its stainless support rod to the melting point of stainless steel, even though the grounded transfer rod provides a massive heat sink.

The dual chamber vacuum system concept is important for more than just tip interchange. It provides a way to interact with the tip in the controlled environment of the source chamber prior to, or following, analysis in the spectrometer chamber. For example, the tip can be exposed to the flux from an *in situ* ion implantation source (seen in Fig. 2) after which transfer to the spectrometer chamber, for analysis, can be accomplished. It has been the author's experience that the extra complexity of the dual chamber system is more than offset by the experimental flexibility it provides, and should be considered as an important feature of any general purpose Imaging Atom-Probe instrument.

Figure 5 is a cutaway view of the spectrometer chamber showing a glass cold finger (with kovar bottom), the rigidly clamped tip holder, and the pulse line connected to a pulse feed-through which is capable of supplying the total tip potential ( $V_{dc} + V_p$ ). As can be seen, coaxial pulse line geometry is maintained to the tip with the vacuum chamber wall forming the coaxial ground of the pulse line. An isolation valve keeps the imaging detector un-



FIG. 4. The tip holder and transfer rod. The specimen "tip" is spot welded to a stainless steel support rod (extreme left) flattened to facilitate spot welding and inserted into a beryllium copper holder. This holder plugs into a second beryllium copper holder, which is mounted at the end of the linear transfer rod.

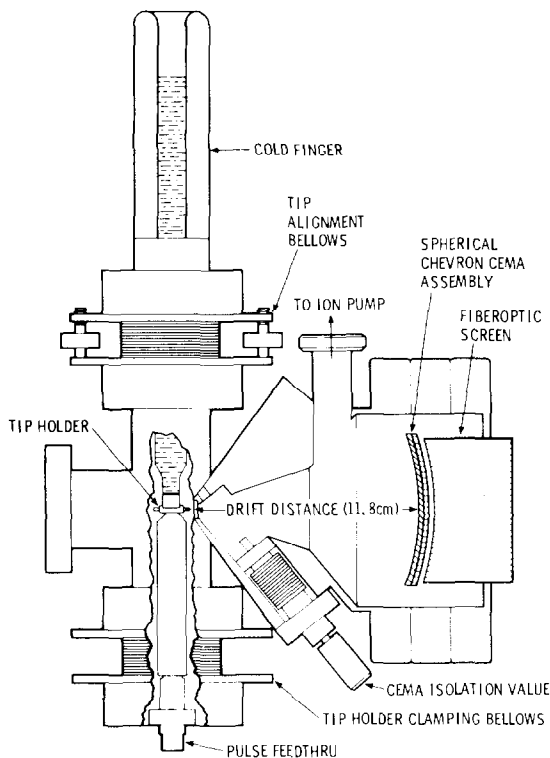


FIG. 5. Schematic drawing of the "spectrometer" chamber. A high vacuum isolation valve (not shown) connects this chamber to the second, or "source", chamber. The tip and beryllium copper holder are shown in their clamped position. The tip is positioned at the radius of curvature of the spherically curved detector using the linear transfer mechanism of Fig. 4. Tip position is routinely controlled to within  $\pm 0.05$  mm of its optimum position, using a telescope and calibrated reticle (not shown).

der vacuum during those infrequent times when the spectrometer chamber may be exposed to the atmosphere.

### C. Tip-to-detector distance

The choice of a tip-to-detector distance will depend, for a detector of given active area, on a compromise between the portion of the tip surface to be observed, and the mass resolution desired. To observe an appreciable fraction of the tip surface, a small tip-to-detector distance must be used. However, for a given ion kinetic energy, small tip-to-detector distances mean short drift distances, short travel times and, consequently, short time intervals between the arrival of successive species. When the difference in arrival time of two different species becomes comparable to the accuracy of the time measurement in a time-of-flight instrument, the two species cannot be unambiguously resolved, and mass resolution will suffer. The problem is aggravated when a flat, rather than a spherically curved, imaging detector is used. Flat detectors cause an inherent time spread in the arrival of each particular species due to the difference in travel distance for the same ion

following an axial and extreme trajectory to the detector. The use of a spherically curved grid placed in front of a flat detector, followed by acceleration of the ions between the grid and the detector, will only marginally improve the situation. Consider the geometry shown in Fig. 6, where FOF is the active diameter of a flat detector and COC is a section of a spherically curved grid of radius  $R$  equal to the axial drift distance of the ion. For a tip placed at  $T$ ,  $\theta$  is the angle which determines the fraction of the tip area observed at the detector. For example, to image the entire tip apex,  $\theta \approx 45^\circ$ .

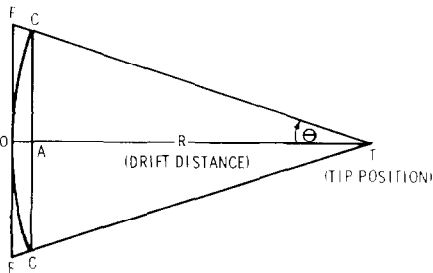


FIG. 6. Tip-to-detector geometry. A flat detector is placed at FOF and a spherical grid at COC.  $\theta$  is the image half-angle defined by the axial distance,  $R$ , and the detector radius,  $OF$ .

From (2) the on-axis travel time of a particular species is

$$T_{on} = KR(V_0)^{1/2} \quad (5)$$

where  $K$  is a constant,  $R$  is the axial travel distance, and  $V_0 (= V_{dc} + V_p)$  is the total difference in potential through which the ion has accelerated prior to drifting over the distance,  $R$ . For the extreme ion trajectory,  $TCF$ , the ion will drift over the distance  $TC (= R)$  with energy  $qV_0$ , where  $q$  is the ionic charge. It will then accelerate over the distance  $FC$  gaining additional energy  $qV$  where  $V$  is the potential difference between the curved grid and the flat detector. The resulting off-axis travel time is:

$$T_{off} = \frac{KR[\sec(\theta) - 1]}{(V + V_0)^{1/2}} + T_{on} \quad (6)$$

The fractional difference in travel time between axial and extreme ion trajectory is then:

$$\frac{T_{off} - T_{on}}{T_{on}} = [\sec(\theta) - 1](1 + V/V_0)^{1/2} \quad (7)$$

Table 1 shows the result of solving (7) for several values of  $\theta$  and  $V/V_0$ . Note that for  $V/V_0 = 0$ , or no acceleration between grid and detector, the ion will drift over the distance  $FC$  with its initial energy,  $qV_0$ , and the presence of the grid can be neglected. In this case, (7) predicts the inherent spread in the arrival time of a single species at a flat detector.

TABLE 1. The fractional difference in travel time for a given species following an axial ( $T_{on}$ ), and extreme ( $T_{off}$ ), ion trajectory to a flat CEMA detector.  $\theta$  is the image half-angle (see Fig. 6).  $V_0$  is the total specimen potential and defines the ion's energy over the drift distance,  $R$ .  $V$  is a negative (post acceleration) potential applied between the input web of the CEMA and a grounded, spherically curved, grid placed in front of it. When  $V = 0$ , the presence of the grid can be neglected, and the last column will predict the effect of using a flat CEMA detector.

$\theta$	Sec $\theta$	$V/V_0$	$(T_{off} - T_{on})/T_{on}$
10°	1.0154	0	1.5 per cent
10°		1	1.1 per cent
10°		2	0.9 per cent
18°	1.0515	0	5.1 per cent
18°		1	3.6 per cent
18°		2	3.0 per cent
45°	1.414	0	41.4 per cent
45°		1	29.3 per cent
45°		2	23.9 per cent

Several interesting observations emerge from an examination of Table 1. For viewing half-angles of 10° or less, flat detectors can usually be used, since the inherent time spread will be only 1.5 per cent. However, such small viewing angles are generally undesirable in imaging applications, since 3 per cent or less of the total surface area would be observed. An obvious exception is the conventional Atom-Probe,<sup>(8)</sup> where the detector is purposely apertured so as to observe only a few atom locations on the surface.

A 45° half-angle is desirable in order to observe the entire surface area from which ions are produced, but this would make a spherically curved detector mandatory if reasonable mass resolution is needed. The use of a spherical grid and a flat detector at such a large viewing angle, even with an appreciable acceleration bias, of say  $2V_0$ , would not be an acceptable alternative, since a large difference between the on and off-axis travel time would be observed for the same species. In general, Table 1 indicates that applying a bias between a spherical grid and a flat detector is, at best, a marginally successful alternative to a spherically curved detector, unless low mass resolution ( $\approx 10$  a.m.u.) is acceptable.

The 18° half-angle adopted by the author in the Imaging Atom-Probe is a compromise between a minimum acceptable viewing angle, adequate mass

resolution and ease of detector fabrication. For a spherical detector of reasonable diameter (7.6 cm), an 18° half angle fixes the radius of curvature (and ion drift distance) at 11.8 cm. Table 2 shows the difference in travel time,  $T(A, B)$ , of two species of  $m/n = A$  and  $m/n = B$  as a function of tip potential  $V_0$  and radius  $r_t$ . If a minimum accuracy in a travel time measurement of 5 nsec is assumed, Table 2 indicates that all species with  $m/n \leq 16$  can be resolved, with single a.m.u. resolution, over a large range of tip potentials. For species with larger  $m/n$  values mass resolution will suffer. For example,  $m/n = 60$  can just be resolved from  $m/n = 62$  (at 20 kV) if a 5 nsec time resolution is assumed. Of course, the calculations shown in Table 2 assume that the ion accelerating potential is well defined and known. The use of a high voltage desorption pulse to partly establish the accelerating potential complicates this assumption, as will be shown in the next section. Invariably, it is an energy spread caused by a poorly defined desorption pulse, and not a timing instrument with inadequate time resolution, which will ultimately limit mass resolution in all Atom-Probe instruments.

#### D. Desorption pulse considerations

If the specimen tip is placed at the end of a properly terminated pulse transmission line, a desorption pulse shape similar to that shown in Fig. 7(a) would be obtained. Such a pulse would be expected to have minimal amplitude fluctuations, with a rise time determined by the switching characteristics of the pulse generator. Since the pulse amplitude would be constant in time, species would be expected to desorb with equal probability over the entire duration of the pulse,  $T_p$ , assuming that the number of species at the surface, available for desorption, was not limited. For adsorbed species, or for a tip whose voltage "end-form"<sup>(17)</sup> had almost been reached, the number of field desorbed species could be limited and the duration of the desorption event would be confined to a small time interval early in the pulse. In either case, a species which desorbs at  $A$  (Fig. 7(a)) would experience full tip potential,  $V_0$ , throughout its travel in the acceleration zone between the tip and the entrance to the drift region. However, an identical species desorbing near  $B$ , would experience full tip potential for only a

TABLE 2. The difference in arrival time at the CEMA,  $T(A, B)$ , of two species of  $m/n = A$  and  $m/n = B$  calculated from (35) and (37) of the text.  $V_0$  is the total tip potential in kilovolts.  $r_t$  is the tip radius in angstroms, which corresponds to a helium best image voltage (BIV) of  $V_0$ .  $r_t$  was calculated by iterating (50) of the text with  $F_0 = 4.5$  V/Å and  $d_0 = 0.0005$  m.

$V_0$	$r_t$	$T(2,1)$	$T(3,2)$	$T(4,3)$	$T(6,4)$	$T(12,6)$	$T(16,12)$
4	150	56	43	36	61	137	72
6	230	46	35	29	50	112	59
12	500	32	25	21	35	79	42
16	690	28	22	18	30	69	36
18	790	26	20	17	29	64	34
20	890	25	19	17	27	61	32

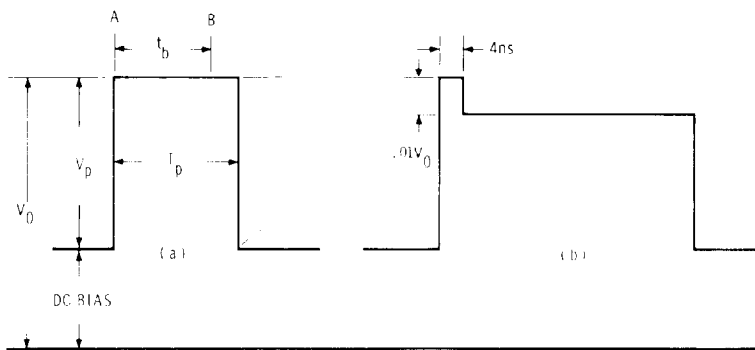


FIG. 7. (a) An expected electrical desorption pulse shape, if the transmission line to the tip could be properly terminated. (b) A desorption pulse shape that can be obtained experimentally, and will optimize mass resolution.

portion of its travel in the acceleration region, since shortly after its desorption the pulse would terminate. The result would be two identical species with different kinetic energies at the entrance to the drift region and, therefore, two different arrival times at the detector. The sequential arrival of these identical species at the detector could not be distinguished from the arrival of two *different* species having the same energy, leading to an ambiguity in species identification. To minimize this possibility, an optimum desorption pulse width,  $T_p$ , can be chosen by assuming that the ion desorbed at A always experiences full tip potential, but that the ion desorbed at B travels a distance,  $d$ , from the tip with full tip potential before the desorption pulse terminates. If the spatial potential at  $d$  was  $V$  before the pulse terminated, and  $(V - \Delta V)$  after, the ion's final kinetic energy at the entrance to the drift region will be:

$$\begin{aligned} \frac{1}{2}mv_t^2 &= ne(V_0 - \Delta V) + ne[(V - \Delta V) - 0] \\ &= ne(V_0 - \Delta V) \\ &= neV_0\left(1 - \frac{\Delta V}{V_0}\right) \end{aligned} \quad (8)$$

where  $m$  is the mass of the ion,  $v_t$  its terminal velocity,  $ne$  its charge,  $V_0$  the total tip potential before the pulse terminated, and  $\Delta V$  the change in potential, at  $d$ , resulting from the termination of the pulse. The change in spacial potential at  $d (= \Delta V)$  can be calculated by assuming a paraboloidal geometry for tip and counter electrode.<sup>(18,19)</sup> For paraxial ions:

$$C = \frac{\Delta V}{V_0} = \frac{V_p}{V_0} \frac{\ln\left[\frac{d}{d_0} + \frac{r_t}{2d_0}\right]}{\ln[r_t/2d_0]} \quad (9)$$

where  $r_t$  is the tip radius, and  $d_0$  is the tip-to-counter-electrode distance.

Since the ion desorbing at B will drift over the distance  $R$  with velocity,  $v_t$ , its travel time,  $T_B$ , will be given by

$$T_B^2 = \frac{R^2}{v_t^2} = \frac{mR^2}{2neV_0(1-C)} \quad (10)$$

But  $(mR^2/2neV_0)$  is just the square of the travel time of the identical ion desorbed at A, which traveled through the acceleration region with full tip potential. That is, for a pulse duration  $T_p$  long compared to the travel time (in the acceleration region) of the ion which desorbed at A:

$$mR^2/2neV_0 = T_A^2 \quad (11)$$

and for  $C \ll 1$ , (10) becomes:

$$\frac{T_B}{T_A} = (1-C)^{-1/2} \approx 1 + \frac{C}{2} \quad (12)$$

if time is measured from the desorption event at A, corresponding to the rise of the desorption pulse, the species which desorbs at B, actually desorbs at a time,  $t_b$ , after the ion which desorbs at A. Therefore, (12) actually should be written:

$$\frac{T_B - t_b}{T_A} = 1 + \frac{C}{2} \quad (13)$$

The worst mass resolution will occur when the pulse terminates as the species at B desorbs. Then  $d = 0$  in (9), and  $t_b$  in (13) becomes the pulse width  $T_p$ , so that:

$$\frac{T_B - T_p}{T_A} = 1 + \frac{V_p}{2V_0} \quad (14)$$

For the best mass resolution in this extreme case,

$$\frac{V_p}{2V_0} \ll 1 \quad (15)$$

or:

$$T_B - T_A = T_p. \quad (16)$$

But the difference in the desorption time ( $T_B - T_A$ ) of the two identical species desorbing at  $B$  and  $A$  must also be less than the arrival time difference (at the detector) of two different species, of the same energy, which are just to be resolved. If their arrival time difference is  $\Delta T$ , (16) can be written:

$$T_p < \Delta T. \quad (16a)$$

If the ion which desorbs at  $A$  is to acquire full tip potential, we recall that the pulse duration,  $T_p$ , must be longer than its travel time,  $T_A$ , in the acceleration region in front of the tip. That is:

$$T_p > T_A. \quad (17)$$

Combining (16a) and (17) gives the inequality:

$$T_A < T_p < \Delta T \quad (17a)$$

which is the condition that defines the optimum pulse width,  $T_p$ , that must be satisfied in order to achieve optimum mass resolution.

To estimate the optimum pulse width, assume species of  $m/n = 60$  and  $61$  are to be resolved at a tip potential,  $V_0 = 10$  kV (tip radius,  $R \approx 400$  Å). For a drift distance of 11.8 cm, and an acceleration region,  $d_0 = 0.0005$  m in extent:

$$T_A = 3 \text{ nsec (for } m/n = 61), \text{ and } \Delta T = 5 \text{ nsec}$$

so that (17a) becomes:

$$3 \text{ nsec} < T_p < 5 \text{ nsec}$$

or:

$$T_p \approx 4 \text{ nsec.} \quad (18)$$

It should be noted that the calculated separation in time of these two species (5 nsec at  $V_0 = 10$  kV) is of the order of the expected accuracy in making travel time measurements, so that these species could not be expected to be resolved at greater tip potentials.

There are actually two conditions on the desorption pulse which must be satisfied for optimum mass resolution. The first is the condition just discussed (17a), the second is the condition on the pulse amplitude given by (15). Together, these two conditions require:

$$T_p \approx 4 \text{ nsec and } V_p \ll 2V_0. \quad (19)$$

Although a 4 nsec desorption pulse width is readily obtained, the condition on the desorption pulse amplitude may be difficult to achieve. This is simply

because (1) desorption must initiate at an amplitude close to the maximum pulse amplitude and, (2) the maximum pulse amplitude must be made a small percentage of the total tip bias  $V_0$ .<sup>(20)</sup> If no d.c. bias is used,  $V_0 = V_p$  and desorption *must* be initiated at the maximum desorption pulse amplitude. In practice, mass resolution can be improved by using a pulse such as shown in Fig. 7(b) provided that field desorption is initiated close to the maximum of the initial overshoot. In this case, the initial overshoot becomes the effective desorption pulse, and a species desorbing at its trailing edge will experience only a small percentage decrease in total tip potential as it desorbs and accelerates away from the tip.

The previous analysis leads, inescapably, to a single conclusion: *optimum mass resolution requires that desorption starts at an amplitude as close as possible to the maximum amplitude of a well defined desorption pulse.* Only in this case will all species experience an essentially constant acceleration potential upon desorption and, therefore, a minimum spread in initial energy.

The risetime of the desorption pulse appears to be important only in that it is usually used as a zero time (or fiducial) marker to indicate the instant of desorption. As such, the risetime must be less than the accuracy to which ion travel times can be measured, so that an accurate measure of each ion travel time can be obtained. There is no conclusive evidence to indicate that the rate-of-rise of the desorption pulse affects the desorption process, although such an effect has been suggested.<sup>(21)</sup>

### E. Desorption pulse transmission

Instrumental problems which are generally associated with the actual desorption pulse shape at the tip (poor mass resolution, "premature" field-evaporation) are usually caused by the method used to transmit the pulse to the tip. In general, the shorter the distance between tip and pulse generator output, and the closer to the generator's characteristic impedance the interconnecting line becomes, the more close to optimum (Fig. 7(b)) the desorption pulse shape will become.

Pulse transmission is usually complicated by the necessity to bias the tip to some large d.c. potential while simultaneously applying the desorption pulse. This requires the use of a high voltage coupling capacitor in series with the pulse line, to block the d.c. bias from the pulse generator's load resistor, a procedure often resulting in a distortion of the pulse shape. If the capacitor is placed outside the vacuum system, a vacuum feed-through capable of surviving full tip potential while having an impedance only minimally different from that of the pulse generator, must be used. If the capacitor is placed inside the vacuum system, a commercially available<sup>(22)</sup> pulse feed-through can be used, but the capacitor must be vacuum compatible. This requires the use of a low outgassing component, or encap-

sulation, in a low outgassing container such as a glass tube.

The unterminated portion of the pulse line between the capacitor and the tip must be kept as short as possible and have an impedance as close as possible to  $Z_0$ , the pulse generator's characteristic impedance. For a coaxial geometry, the ratio of the inner conductor diameter,  $a$ , to the diameter of the outer conductor,  $b$ , of the pulse transmission line must satisfy the relation:

$$Z = \frac{60}{\sqrt{\kappa}} \ln(b/a) \quad (20)$$

where  $Z$  is the desired impedance of the line and  $\kappa$  is the dielectric constant. Transitions from one diameter ratio to another, often required by constraints placed on the size of the line, must, ideally, be gradual and smooth. For fixed lines, such constraints are relatively easy to satisfy, but if flexible lines are required the design becomes much more difficult. Figure 8 shows a useful, rigid pulse line configuration, used by the author, when it is desired to place the capacitor outside the vacuum

system. The vacuum feed-through and inner conductor of the pulse line are mounted on a 7 cm o.d. vacuum flange (upper portion of Fig. 8). The diameter of the inner conductor was determined, for a  $50 \Omega$  system, from (20) with the diameter of the outer conductor taken as the inside diameter of the vacuum system wall (see Fig. 5). A brass housing contains the commercial coupling capacitor<sup>12,3)</sup> and the termination resistor. The resistor is composed of eleven  $550 \Omega$  (1 W) carbon resistors mounted symmetrically, and in parallel, on a circular glass epoxy printed circuit board. This termination resistor has proved to be very reliable, surviving repetitive pulsing at 10 ppsec with a 3.5 kV pulse amplitude. The resistor does not noticeably distort the pulse shape. As can be seen in Fig. 8, the distance from the termination resistor to the tip, at the end of the inner conductor, was kept short although no provision was made to minimize impedance discontinuities in the vicinity of the capacitor and feed-through.

The d.c. bias is applied to the tip through a  $5000 \Omega$ , in-vacuum resistor (not shown) which is connected to the center conductor of the pulse

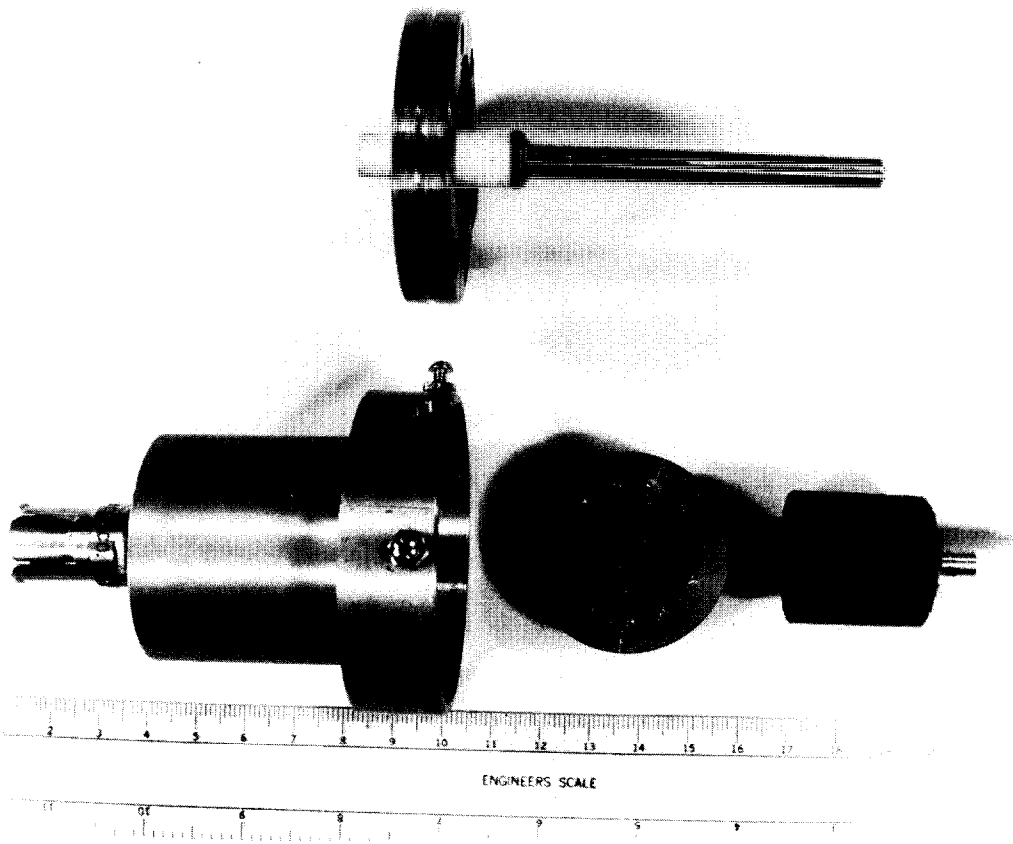


FIG. 8. Capacitive coupling assembly for transmitting the desorption pulse into the vacuum system. The feed-through and center conductor of the pulse line which clamps the tip to the base of the cold finger (see Fig. 5), is shown in the upper portion of the figure. The termination resistor of the pulse line, the coupling capacitor and the shielded enclosure (all mounted outside of the vacuum system) are shown in the lower portion of the figure.

line. This resistor prevents the pulse from traveling along the d.c. bias line, and must be placed within a few cm of the center conductor in order to minimize reflections. By carefully choosing the distance between this resistor and its connection to the center conductor, a form of primitive pulse shaping can be achieved.

#### F. Desorption pulse generation

The simplest (and probably the best) method for generating the desorption pulse is a cable-discharge pulse generator, shown schematically in Fig. 9. A length,  $L$ , of coaxial cable (of characteristic impedance  $Z_0$ ) is charged through resistor  $R_C$  to a positive d.c. potential,  $+V_{\text{charging}}$ . Then, a fast switch,  $S$ , is suddenly closed. As the contacts

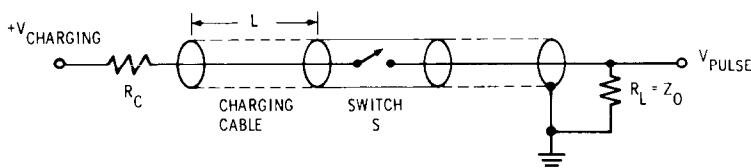


FIG. 9. Schematic diagram of a cable discharge pulse generator.  $V_{\text{pulse}}$  (the output pulse amplitude) will be one-half of the cable charging voltage,  $V_{\text{charging}}$ . The pulse width will be twice the electrical length of the charging cable,  $L$ .

of the switch approach each other, an arc, whose build-up time is measured in nsec, is established. Since the arc voltage drop is a small fraction of the total charging voltage, the switch is considered closed at this instant, and the charging line connected to the load resistor,  $R_L$ . The resulting positive voltage step propagates toward the load resistor,  $R_L$ , while a similar negative step travels along the charging cable (of length,  $L$ ) toward the charging resistor,  $R_C$ . Since  $R_C \gg Z_0$  when the negative step reaches  $R_C$ , it is reflected in phase, back to the load resistor extinguishing the arc as it passes through the switch contacts. At the load, this negative step becomes the trailing edge of the output pulse. Since the leading edge is generated by the positive voltage step, the rise-time of the output pulse is determined by the arc build-up time. The pulse width,  $T_p$ , is determined by the difference in arrival time at the load of the two voltage steps. This time difference is just twice the propagation time along the charging cable. For typical  $50\ \Omega$  charging cables (RG-58U or RG-213), propagation times are approximately 5 nsec/m. Therefore, a cable,  $L$  meters in length, will produce a pulse whose width,  $T_p$ , is given by:

$$T_p(\text{nsec}) = 10 L. \quad (21)$$

The pulse amplitude for a properly terminated cable ( $R_L = Z_0$ ) will be one-half of  $V_{\text{charging}}$  since the charging line impedance,  $Z_0$ , and the load resistor,  $R_L$ , can be considered to be a voltage divider with a total impedance of  $2Z_0$  (Fig. 10).

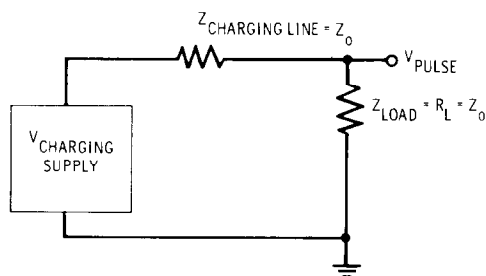


FIG. 10. Schematic diagram of the pulse generator showing the cable impedance  $Z_0$  as a resistor in series with the load resistor,  $R_L (= Z_0)$ . The terminated pulse generator can be considered to be a voltage divider, producing an output pulse with an amplitude one-half of the cable charging voltage.

That is, from Fig. 10:

$$V_{\text{pulse}} = V_{\text{charging}} \frac{Z_0}{2Z_0} = \frac{V_{\text{charging}}}{2}. \quad (22)$$

Since it is important to preserve the characteristic impedance of the pulse line over its entire length, the switch,  $S$ , must be housed in such a manner as to preserve  $Z_0$ .

The maximum pulse amplitude available with the generator of Fig. 9 will usually be determined by the electrical breakdown characteristics of the switch. For example, if a mercury-wetted relay is used,  $V_{\text{charging}}$  is usually limited to less than 8 kV, or  $V_{\text{pulse}}$  to less than 4 kV. To achieve higher amplitudes, two or more relays can, in principle, be inserted in the line in series, with identical resistors placed across each relay to equalize the voltage drops across them. Activating one switch will "over voltage" the others, causing electrical breakdown resulting in a conductive path through which the pulse can propagate.

Although producing a high voltage desorption pulse is a relatively simple operation, accurately measuring the true desorption pulse shape at the tip surface can be very difficult. Measurements of the pulse shape along the transmission line to the tip, or at the tip mount, using high frequency oscilloscope probes, can be used to estimate general features of the true desorption pulse shape at the tip, but cannot determine the actual pulse shape with accuracy.

### G. Desorption pulse measurement

To appreciate the error inherent in using measurements of the pulse shape along the transmission line, it is helpful to think of the true time dependent potential at the specimen surface as being caused by the superposition of the desorption pulse, and multiple secondary pulses reflected from impedance discontinuities encountered by the pulse as it propagates to the tip. Since these reflections will damp rapidly with time, only the initial portion of the pulse at the tip surface will differ significantly in shape from that measured by conventional probes or voltage monitors along the pulse transmission line. However, the shape of the initial portion of the pulse is of primary importance since the desorbing ions travel through the acceleration region in front of the tip early in the pulse.

To determine the true pulse shape at the tip surface, a procedure has been successfully developed,<sup>(24)</sup> which consists of generating a negative pulse (known to be identical in shape to the positive desorption pulse) and applying this pulse to the tip through the pulse transmission line. Since the negative pulse will encounter the same impedance discontinuities as its positive counterpart, it will produce the same pulse shape at the tip, but will initiate field-electron emission instead of positive ion desorption. The time-varying field emission current which results can be monitored at the detector, while the voltage pulse waveform appearing at some point on the pulse transmission line is simultaneously recorded. It is assumed that the average pulse amplitude *measured on the transmission line late in the pulse* is the same as that appearing at the tip late in the pulse, and is responsible for producing the average field-emission current measured at the detector during the same time interval. By changing the pulse amplitude, several average-voltage, average field-emission current measurements can be made late in the pulse, and each pair used to determine the constants *C* and *D* in the well-known Fowler-Nordheim<sup>(25)</sup> expression:

$$I = CV^2 \exp(-D/V). \quad (23)$$

The average values of *C* and *D* obtained are then used in (23) to convert, point-by-point, a measured field emission current waveform into the corresponding voltage waveform at the tip responsible for its production. Since the positive desorption pulse waveform is known, by measurement, to be identical in shape to the negative pulse at any point on the pulse transmission line, and both polarity pulses encounter the same impedance discontinuities when traveling to the tip, the shape of the negative voltage waveform calculated from (23) can be considered to be identical to that of the positive voltage pulse used to initiate field-desorption. Figure 11 shows a typical negative voltage

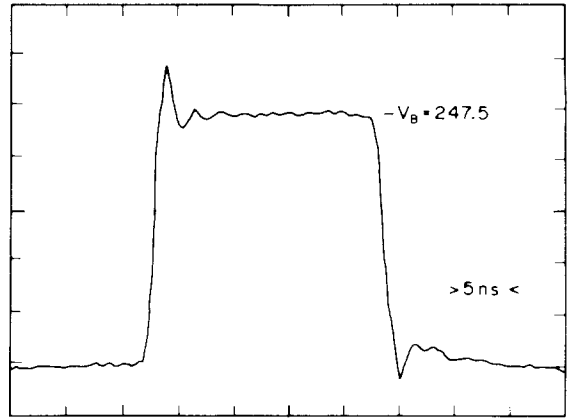


FIG. 11. A negative pulse (known to be identical in shape to the positive desorption pulse) applied to the tip to initiate field-electron emission. The pulse was measured on the transmission line to the specimen with a Tektronix CT-3 current viewing transformer, and recorded with a Tektronix W2221 waveform digitizing system. Horizontal scale is 5 nsec/div. Vertical scale is 50.5 V/div.

pulse as measured on the transmission line to the tip. The lower waveform of Fig. 12 shows the resulting field-emission current as measured at the detector. The upper waveform is the actual voltage pulse shape appearing at the tip as calculated by the method just described. The waveforms of Figs. 11 and 12 are negative, and have been inverted for clarity. As expected, the shape of the voltage pulse, which appears at the tip, is similar to that measured on the transmission line late in the pulse, but is significantly different from the transmission line measurement early in the pulse (the initial overshoot is smaller and broader).

To insure measurement accuracy and to reproduce the experimental field-desorption conditions as accurately as possible, it is important to use a small pulse amplitude superim-

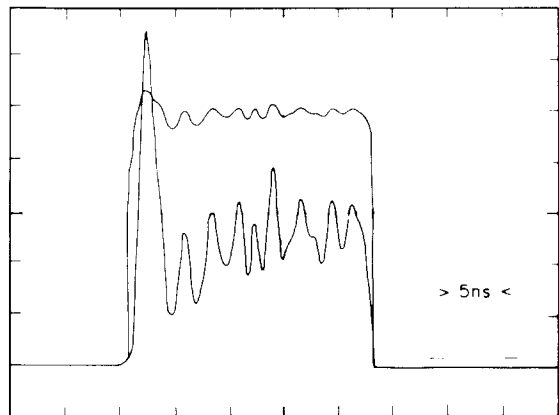


FIG. 12. Lower waveform: The field emission current pulse (monitored at the detector) resulting from the voltage pulse of Fig. 11 as recorded with a Tektronix W2221 waveform digitizing system. The upper waveform shows the actual desorption pulse shape appearing at the tip, obtained by the method described in the text.

posed on a larger d.c. bias so that (15) is satisfied ( $V_{\text{pulse}} \ll 2V_0$ ). Without a d.c. bias, the initial overshoot of the voltage pulse at the tip may produce a large current overshoot, which would dominate the current waveform so that small current variations later in the pulse could not be accurately measured. To insure adequate field-emission currents, a low work function area of the tip should be oriented toward the detector. It should be noted that optimizing the transmission line to the tip for best mass resolution means, essentially, producing a pulse with a minimal initial overshoot approximately 4 nsec in duration (18). Since this condition can be determined by observing the field emission current waveform, it is usually unnecessary to iterate (23) to find the true desorption pulse shape for most situations of practical interest.

#### H. Detector configuration

The detector used in the Imaging Atom-Probe is perhaps the most important part of the entire instrument. It must have low noise, high gain, a small inherent transit time spread, and an imaging capability which preserves the spatial distribution of the incoming ions. Ideally, it must be spherically curved to insure identical travel distances for all field-desorbed species, and have the ability to be time-gated (its gain switched from zero to maximum) in nanoseconds. Two spherically curved Channel Electron Multiplier Arrays (CEMA's) operating in tandem, the so-called "chevron" configuration, satisfy these requirements. Each CEMA of the chevron pair is composed of a myriad of glass capillaries (or "channels") whose inner wall, having a high

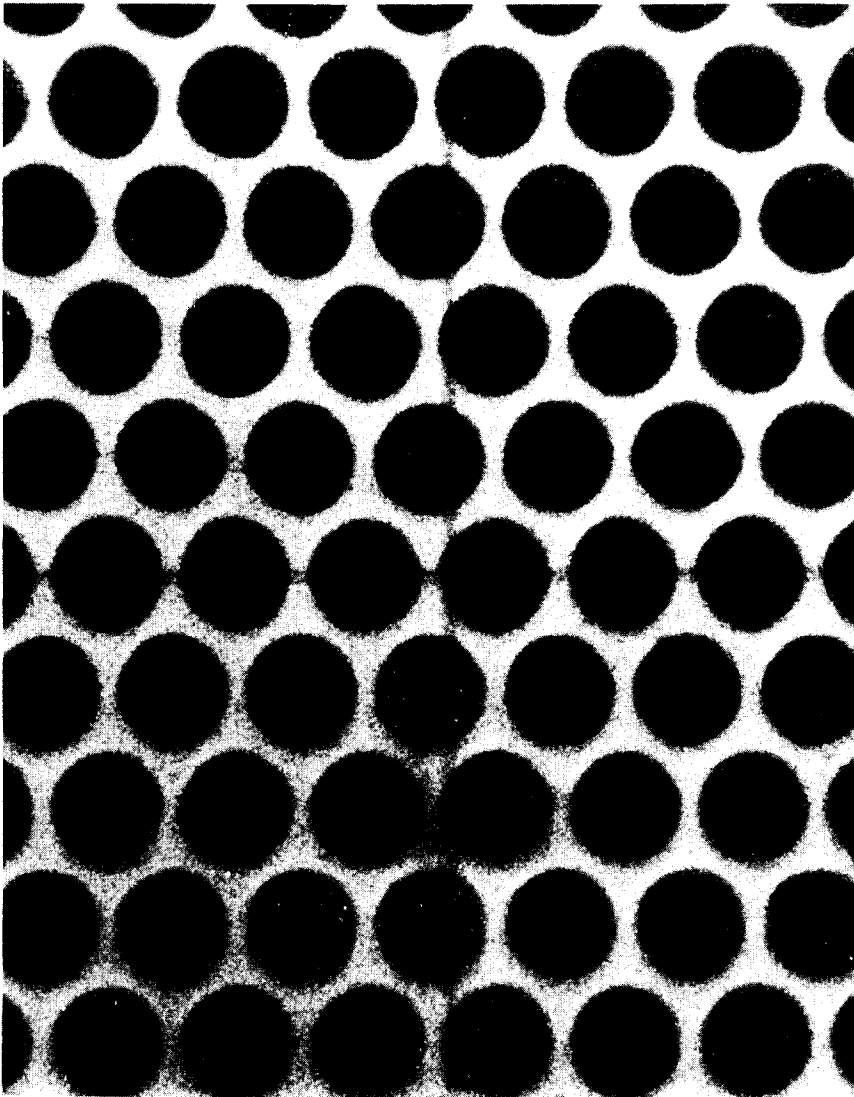


FIG. 13. An optical micrograph of the central region of a CEMA plate showing the active capillaries (as dark circles), and the conductively coated intercapillary (web) area. The capillaries are approximately  $40 \mu$  in diameter and are spaced on  $50 \mu$  centers.

secondary electron coefficient, is responsible for sustaining and amplifying the electron avalanche which provides high gain. Typically, these capillaries are  $40\mu$  in diameter and spaced on  $50\mu$  centers, in an orderly geometric array (Fig. 13), which is fabricated into a spherically curved "plate" less than 2 mm thick. Each face of the plate between the capillary openings is conductively coated so that a bias voltage can be applied across the plate. The bias causes the secondary avalanche in each active capillary to proceed deeper and deeper into the capillary until it finally emerges, greatly amplified ( $10^3$ – $10^4$ ), from the far surface. The second plate further amplifies the avalanche so that a total gain of  $10^7$ – $10^8$  is achieved. The electron "cloud" emerging from each active capillary of the second plate is accelerated to a phosphor screen placed in close proximity, causing the emerging electron cloud to become visible as a spot of light on the phosphor. Since the spacing of neighboring channels in each plate is usually smaller than the spatial separation of adjacent, incoming ions, the resolution of the desorption image on the phosphor screen will generally be limited by the physical process of desorption, and not by detector characteristics.

Figure 14 shows the spherical chevron CEMA assembly<sup>(26)</sup> used in the Imaging Atom-Probe. The two CEMA plates are sandwiched between two annular stainless steel rings, insulated from ground, which apply a bias voltage of  $+V_1$  and  $+(V_G + V_3)$  to the front surface of the first (input) plate and the rear surface of the second plate, respectively.  $V_G$  is the amplitude of the gate pulse

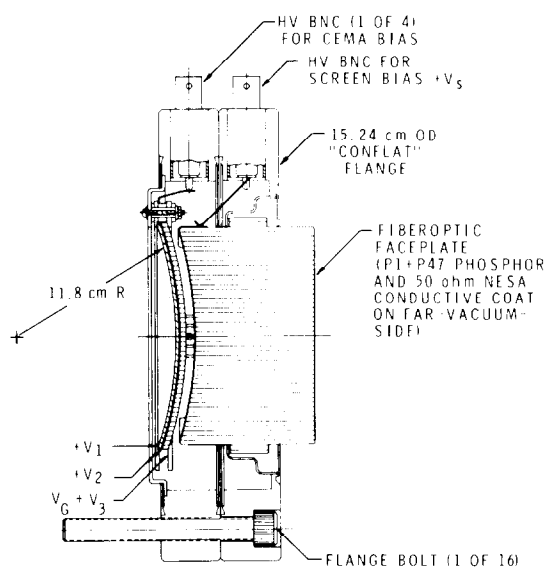


FIG. 14. The chevron CEMA detector assembly designed by the author for the Imaging Atom-Probe (manufactured by Galileo Electro-Optics, Sturbridge, Massachusetts). Typically,  $V_1 = 0$ ,  $V_2 = 1$  kV,  $V_G = 1$  kV,  $V_3 = 1$  kV and  $V_s = 6$  kV.

used for time gating the detector. A 0.05 mm thick stainless steel annular ring (at potential  $+V_2$ ) separates the two CEMA plates and defines a field-free region between them. The CEMA assembly, together with four high-voltage vacuum feed-throughs which supply the bias voltages, is mounted in a single 15.2 cm o.d. ("conflat") vacuum flange having a knife-edge seal on each side.

The phosphor screen of the detector is settled onto a spherically curved, conductively coated, fiberoptic faceplate, which is sealed into a spun Carpenter-49 alloy steel<sup>(27)</sup> adapter welded to a second conflat flange. A high voltage BNC feed-through makes electrical contact with the conductive coating to supply the required screen bias,  $V_s$ , and allow the electron pulses caused by arriving field desorbed ions to be recorded. The flat external surface of the fiberoptic faceplate permits the desorption image to be photographed by direct contact with Polaroid type 57 (ASA 3000) film. Typically,  $V_1 = 0$ ,  $V_2 = 1$  kV,  $(V_1 + V_G) = 2$  kV and  $V_s = 6$  kV.

### I. Detector efficiency

One of the most controversial, and apparently misunderstood, parameters of prime importance to Imaging Atom-Probe spectroscopy is CEMA detection efficiency. For an incoming particle to be detected, it must cause the release of at least one secondary electron within at least one channel of the CEMA plate. As a result, the detection efficiency of a CEMA might be expected to be given by the ratio of active channel area to inactive interchannel (or web) area. Using this simple geometric argument, several authors<sup>(14,28)</sup> have claimed the resulting detection efficiency of 50 per cent (or less) as an explanation for the less than perfect crystallographic regularity usually observed in single pulse desorption images. Without further clarification, such an explanation of image quality is misleading, since the detection efficiency of a CEMA can actually be much greater than 50 per cent, depending on the magnitude (and sign) of the bias voltage applied to the web of the first CEMA plate.<sup>(29)</sup>

Consider the requirements for producing an image spot caused by an ion which strikes the CEMA web between adjacent channels. The incoming ion, striking the web, will release secondary electrons. If these secondaries are collected in adjacent capillaries, an image spot will be produced. If they are not collected, an image spot will not be produced, and the geometric detection efficiency of approximately 50 per cent will prevail. But the collection of secondary electrons from the web will critically depend on the spatial distribution of the electric field emerging from the entrance of each active capillary. This electric field will, in turn, depend on the magnitude (and the sign) of the CEMA bias applied to the web.

A large negative bias applied to the input web will result in the loss of virtually all secondary electrons from the surface of the web, producing the geometric detection efficiency determined by the ratio of channel-to-web area. An excessively large positive bias on the input web will prevent the secondary electrons from leaving the web. Since they will not be collected in adjacent channels, the geometric detection efficiency will again prevail.

As the web bias is made less positive, secondary electrons which leave the web surface will be returned by the fringing fields emerging from the channels. Although these secondaries will tend to be collected in channels, the point of collection may be far from the point of impact of the original desorbed ion. The result will be a reasonably large detection efficiency (approaching 100 per cent), but an image on the CEMA screen which will not preserve the spatial distribution of the arriving ions. Since several secondary electrons may be produced for each ion impact, and these secondaries may be collected in different channels at various distances from the point of impact of the original ion, several distinct image spots may even be produced by a single ion impact.

Finally, at some optimum positive bias, secondaries will be collected entirely within adjacent channels, resulting in a high detection efficiency and an image which preserves the spatial distribution of the desorbing ions, but at the expense of some image resolution (see §4A). Figure 15 shows a computer simulation of optimum CEMA biasing in which all secondaries originating at the web at the point of an ion impact are returned to adjacent

channels. In this simulation, a potential of +22.5 V was applied to the conductive input web of a CEMA with ground potential fixed at 2.8 channel diameters from its surface. Channels were assumed to be  $36\ \mu$  in diameter, spaced  $50\ \mu$  center-to-center, and the secondary electrons were given an initial energy of 2.5 eV. Since the electric field emerging from each channel is responsible for collecting secondaries from the web, an average field strength at the web for optimum collection can be defined, such that:

$$F_{\text{optimum}} = 22.5\ \text{V} / 2.8\ (36 \times 10^{-3})\ \text{mm} \\ = 230\ \text{V/mm.} \quad (24)$$

Such a field can easily be established. For example, the input web can be biased to 230 V, and a high transmission grounded grid placed 1 mm from its surface. However, since secondaries created on the grid also have a probability of being collected by fringing fields from active capillaries, they could lead to an increase in random, background image spots. In addition, since spherically curved CEMA plates would require a high transmission spherical grid which is difficult to fabricate, it is usually expedient to ground the input CEMA web and work with a reduced detection efficiency. Grounding the input web may not ensure detection of virtually all field desorbed species, but it will preserve a well defined drift region. In order to minimize possible confusion resulting from random background, individual single pulse desorption images should be photographically integrated to "average-out" the random image spots and leave the reproducible features of the desorption image intact.

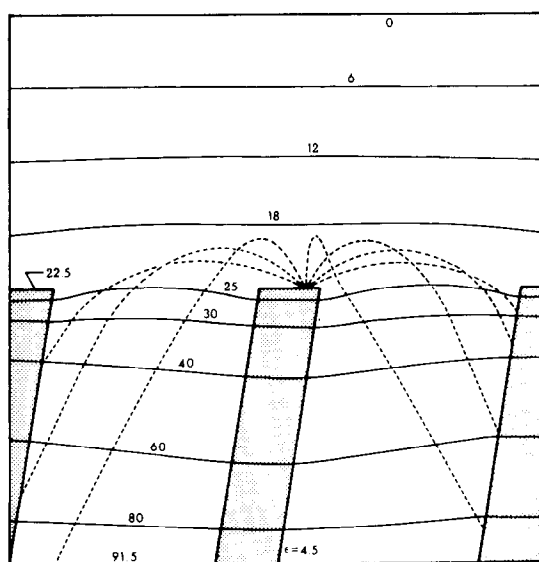


FIG. 15. Computer simulation of the collection efficiency of a CEMA detector (shown in cross section) when an optimum electric field (230 V/mm) is established at the input web. A bias of 22.5 V was applied to the web in this simulation. The channel diameter is  $36\ \mu$ , and the center-to-center channel spacing is  $50\ \mu$ . The vertical scale is compressed (the zero equipotential was actually placed 2.8 channel diameters from the input web).

### J. Time-gating the detector

Because the CEMA detector is operated at high gain, image spots appearing at random will always be present on its phosphor screen. These image spots, due to random electron avalanches initiated by cosmic rays, energetic photons and thermal processes within the CEMA, define an inherent detector noise level or "dark current." For well outgassed CEMAs in high vacuum, which are free from field-emission sources, the dark current at a gain of  $10^7$ – $10^8$  will appear as 30–60 image spots each minute, randomly located on its phosphor screen. In addition to this inherent detector background, random image spots will appear as the specimen potential  $V_0$  is increased. These spots are produced by the arrival of residual gas ions formed in the high electric field above the tip surface, and will constitute the major source of detector noise at elevated specimen potentials even at ambient pressures below  $10^{-9}$  Torr. As a result, an image recorded during a desorption event will be the sum of the actual desorption image and a background noise image. Obviously, if the "on-time" of the detector could be limited to a short interval centered on the desorption event, the background noise could be substantially reduced.

But this "time-gating" procedure can be made even more selective. During the desorption event, species will arrive at the CEMA consecutively in time. Those with the smallest  $m/n$  will arrive first and those with the largest  $m/n$  last. If the CEMA is time-gated coincidently with the arrival of only one species, a desorption image, due only to the distribution of that particular species on the tip surface, can be obtained. Although other authors considered selective time-gating possible,<sup>(6)</sup> they thought that acceptable mass resolution could not be achieved<sup>(10)</sup> and, consequently, did not selectively time-gate their images. Independently, as a logical extension of the Imaging Atom-Probe,<sup>(5)</sup> the author succeeded in selectively gating for a particular species with acceptable mass resolution<sup>(7)</sup> by applying a positive 1 kV, 10 nsec pulse to the rear surface of the second CEMA plate in a chevron pair ( $V_G$  in Fig. 14). Together with a d.c. bias  $+V_3$ , the gate pulse amplitude determined the CEMA gain. In order to generate the required gate pulse, a cable discharge pulse generator (employing a krytron<sup>(31)</sup> switch tube) was designed. A krytron tube is a high voltage, gas filled triode, which can be triggered into conduction by applying a high voltage pulse to its grid. Although the delay between input trigger and output pulse can be made as small as 150 nsec, with low jitter ( $\approx 2$  nsec is typical) the delay will be a function of cable-charging voltage. This may, at first, appear to be a limitation, but since the gate pulse amplitude does not have to be varied to adjust CEMA gain (the d.c. bias can be varied instead), the cable charging voltage can be held constant, and the delay fixed at some convenient

value. Figure 16 shows, schematically, the gate pulse generator developed by the author. Figure 17 is a detailed view of the shielded krytron enclosure, krytron switch tube, and trigger circuitry mounted on a small PC board to the right of the krytron tube. The two connections to the krytron switch, which are normally soldered to the enclosure's 50  $\Omega$  connectors are visible at the base of the krytron tube in the center of the Fig. 17. The complete assembly serves as switch, S in Fig. 9.

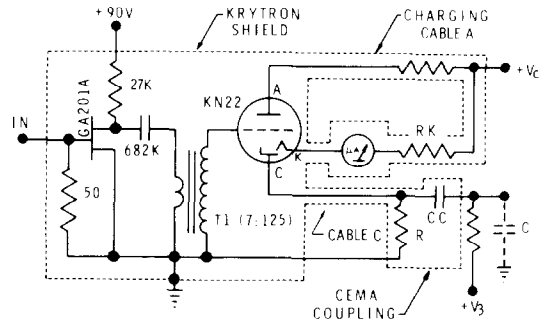


FIG. 16. A schematic diagram of the krytron gate pulse generator showing the krytron trigger circuitry, interconnecting cables and CEMA coupling. The krytron switch tube and trigger circuitry are equivalent to switch "S" in Fig. 9.

When designing a cable discharge pulse generator, one has the option of choosing the characteristic impedance of the system. For example, by paralleling two 50  $\Omega$  cables for use as the charging line (Fig. 16, charging Cable A), and for use as the transmission line to the tip (Cable C), a 25  $\Omega$  system is created. Resistor  $R$  (the cable termination resistor) is made equal to the system's characteristic impedance to properly terminate the pulse line. A low impedance system creates a higher current pulse to the CEMA during gating, which is necessary if a gate pulse of fast rise time is required. To illustrate the need for a high current pulse, consider the instantaneous current,  $i$ , which would be required to pulse a typical CEMA plate capacitance of 120 pF ( $C$  in Fig. 16) to 1000 V in 5 nsec:

$$i = C \frac{dV}{dt} = 120 \times 10^{-12} \frac{1000}{5 \times 10^{-9}} = 24 \text{ A.} \quad (25)$$

The maximum instantaneous current actually available is the gate pulse amplitude divided by the value of the termination resistor. For a 50  $\Omega$  system ( $R = 50$  in Fig. 16):

$$i = V_{\text{charging}}/2R = \frac{2000}{100} = 20 \text{ A} \quad (26)$$

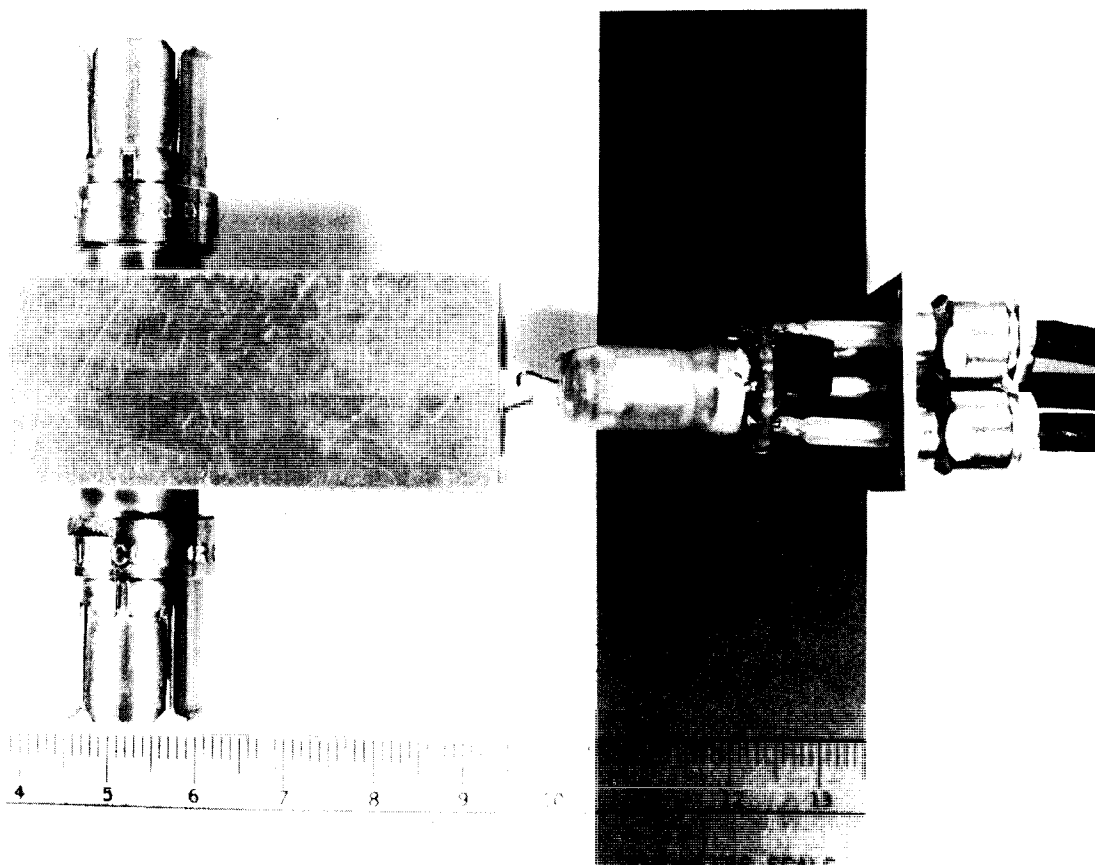


FIG. 17. The krytron enclosure of Fig. 16 containing the krytron switch tube and trigger circuitry. The 50Ω connectors on the enclosure connect to charging cable "A" and pulse transmission cable "C" of Fig. 16. The shielded krytron enclosure is equivalent to switch "S" in Fig. 9.

whereas a 25 Ω system could deliver:

$$i = V_{\text{charging}}/2R = \frac{2000}{50} = 40 \text{ A.} \quad (27)$$

The difference in the shape of the gate pulse for a 25 and a 50 Ω system is shown in Fig. 18, where the two upper waveforms result from a 25 Ω system, and the two lower ones from a 50 Ω system. Pulses A and C are 10 nsec in duration (Cable A of Fig. 16 has an equivalent, electrical length of 5 nsec). Pulses B and D are 30 nsec in duration (Cable A is 15 nsec in length). Gate pulses up to 200 nsec in duration have been successfully generated without cable losses affecting the pulse shape.

The rise-time of the gate pulse is equal to the "switch-on" time of the krytron which is typically 4–8 nsec. The fall time should be equal to the system time constant. It is apparent, from Fig. 16 that the system decay time,  $\tau$ , is just:

$$\tau = RC = R(120 \times 10^{-12}) \quad (28)$$

which is 6 nsec, for a 50 Ω system, and 3 nsec for a 25 Ω system. Since all decay times shown in Fig.

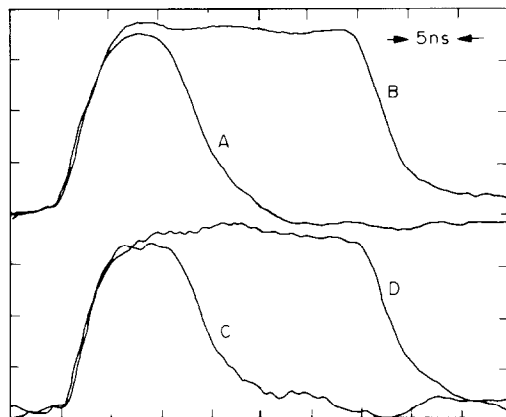


FIG. 18. Typical gate pulse waveforms from a krytron gate pulse generator of 25 Ω (upper waveforms), and 50 Ω (lower waveforms) characteristic impedance. Waveforms A and C result from  $L = 5$  nsec in Fig. 9. Waveforms B and D result from  $L = 15$  nsec in Fig. 9. The gate pulses were monitored by placing a high impedance (10 MΩ), 800 MHz, oscilloscope probe on the phosphor screen connection of the CEMA detector, while gating the CEMA with a 1 kV gate pulse. Capacitive coupling of the gate pulse from the second CEMA plate to the conductively coated phosphor screen permits the gate pulse shape to be monitored with great accuracy at a convenient attenuation.

18 are essentially 6 nsec, the "turn-off" time of the krytron tube must, itself, limit the decay of the gate pulse. It should be noted that the gate pulse coupling capacitor (CC in Fig. 16) is made large compared to C to minimize capacitive voltage division of the gate pulse. Typically,  $CC = 10C = 1200$  pF.

A similar analysis can be applied to the desorption pulse system, since the same method of pulse generation and capacitive coupling is used. But one important difference should be mentioned. The capacitance-to-ground, C, for the desorption pulse system is typically 10 pF. To see the significance of a smaller intrinsic capacitance-to-ground, consider the current requirements for a desorption pulse having a 0.5 nsec rise-time. From (25) the required current,  $i$ , for a desorption pulse 3 kV in amplitude, is:

$$i = (10 \times 10^{-12}) \frac{3000}{0.5 \times 10^{-9}} = 60 \text{ A.} \quad (29)$$

But since the available current into  $50 \Omega$  is

$$i = V_{\text{charging}}/2R = 6000/100 = 60 \text{ A} \quad (30)$$

a  $25 \Omega$  system is apparently not necessary. This is substantiated by the desorption pulse waveform of the author's  $50 \Omega$  system shown in Fig. 11. However, to achieve a 0.5 nsec rise-time, a mercury switch (rather than a krytron tube) must be used. A mercury switch has an additional advantage; it produces a pulse whose characteristics are independent of the cable charging voltage (at least above 1 kV). This means that the charging voltage can be changed as desired, in order to generate desorption pulses of different amplitude.

### K. Detector amplifier

When the Imaging Atom-Probe is operated as a non-gated time-of-flight (TOF) mass spectrometer, the CEMA detector is used only to amplify the current pulses produced by the sequential arrival

of field desorbed species. Background noise is eliminated by displaying the amplified pulses from the arrival of the desorbed species on an oscilloscope sweep initiated by the desorption pulse, and lasting only until the last species of interest has arrived at the CEMA. In effect, the oscilloscope sweep becomes a "time-window", open only to the species of interest. Since travel times, even at the lowest ion energies, are usually less than  $10 \mu\text{sec}$ , background noise will be effectively eliminated.

In order to convert the electron current pulses at the CEMA screen to voltage pulses capable of being displayed on an oscilloscope, a suitable buffer-amplifier must be used. The amplitude of the voltage pulses will depend on the input impedance of the buffer, while their decay time will depend on its input time constant. The rise-time of the voltage pulses produced by the buffer will be governed by the time during which charge is being deposited on the CEMA, providing the rise-time of the buffer-amplifier can be neglected. That is, the rise-time of a voltage pulse observed on the oscilloscope, corresponding to the arrival of a desorbed species, is a measure of the interval of time associated with the desorption of that particular species from the tip surface. For example, the rise-time of pulses associated with adsorbed surface species will, in general, be less than that observed for substrate species, simply because there is a finite number of adsorbed species on the surface (which are usually removed early in the desorption pulse), but there is an essentially infinite number of substrate species which can be removed throughout the entire effective desorption width. Since the interval of desorption is not generally of interest, it is convenient to use an amplifier whose inherent rise-time is greater than the effective desorption pulse width, so that the rise-time of all detected species will be identical.

Figure 19 shows an inexpensive buffer-amplifier, which can be made from a commercially available integrated circuit.<sup>(32)</sup> Its connection to the CEMA screen is also shown. Because of the high input impedance of the device, signal decay times are longer than the time between the arrival

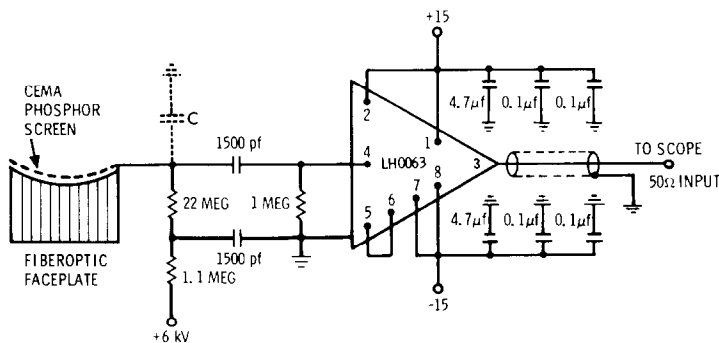


FIG. 19. The CEMA amplifier and its connection to the CEMA screen. The integrated circuit (National Semiconductor LH0063), and associated components, are mounted as close to the CEMA screen as possible to minimize the intrinsic input capacitance-to-ground.

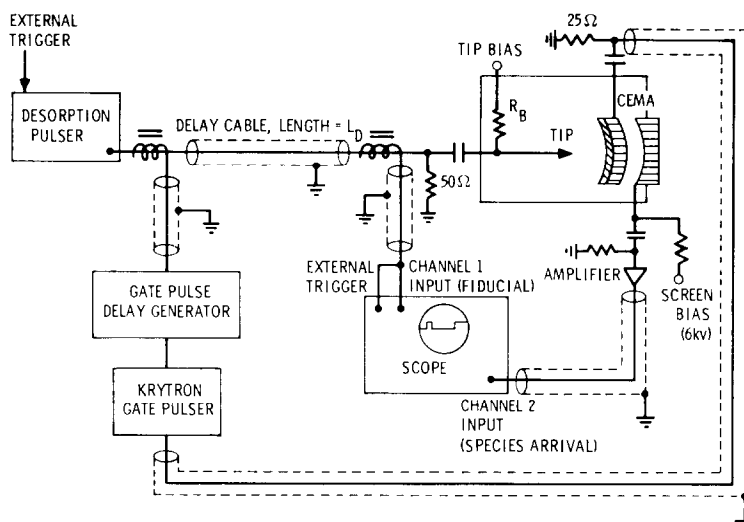


FIG. 20. Schematic diagram of the Imaging Atom-Probe showing the major components and interconnecting cables. The desorption pulse cable length,  $L_D$ , is adjusted to compensate for the inherent delay in the gate pulse circuit. This insures that the center of the gate pulse will coincide with the rise of the desorption pulse when the gate pulse delay generator is set to zero delay.

of successive species, and usually longer than the oscilloscope sweep. As a result, the oscilloscope will display a time integrated, or "stairstep", waveform in which the arrival of a species is indicated by a sudden (step-like) increase in signal level, which remains essentially constant until the arrival of the next species.

Since the input of the CEMA is operated near ground potential, the CEMA screen must be biased to a high positive potential, and the amplifier must be a.c. coupled. To insure that the amplifier rise-time is not degraded, the circuit shown in Fig. 19 is externally mounted on the fiberoptic screen flange of the CEMA assembly.

#### L. Timing considerations

A discussion of Imaging Atom-Probe Instrumentation would not be complete without some comments on system timing. Because of the necessity of precisely positioning the gate pulse in time, the length of the cables which interconnect system components (and the intrinsic delay of these components), must be carefully considered. Figure 20 is a schematic drawing of the Imaging Atom-Probe showing the major components and interconnecting cables. All cables are terminated in their characteristic impedance. Figure 21 shows a typical timing sequence. In Fig. 21(a), the actual ion travel time,  $T$ , is shown, measured from the leading edge of the desorption pulse at the tip to the leading edge of the electron pulse at the CEMA screen. The electron transit time in the CEMA has been neglected. The measured travel time differs from  $T$  in that it takes the output signal from the CEMA a finite time,  $T_D$ , to be displayed on the oscilloscope. This is shown in Fig. 21(b). To compensate for  $T_D$ , the fiducial pulse at the oscilloscope, whose rise indicates the zero of time, is

also delayed by  $T_D$ . The result, shown in Fig. 21(c), provides for an accurate measurement of the ion's true travel time on the oscilloscope sweep.

The gate-pulse delay generator, krytron gate pulser and interconnecting cables, shown in Fig. 20, have associated with them an intrinsic time delay,  $T_G$ . Since it is usually desirable to center the gate pulse of width,  $W$  on the rise of the desorption pulse at zero gate pulse delay, the circuitry must compensate for  $T_G$ . This is accomplished by inserting a fixed delay  $(T_G - W/2)L_D$ , into the desorption pulse line to the tip (Fig. 20). With the addition of this delay, the gate-pulse delay generator can be set to the actual travel time of a

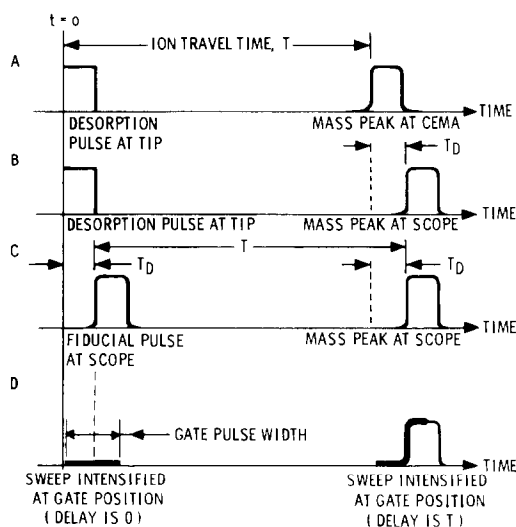


FIG. 21. Timing schematic for the Imaging Atom-Probe.  $T_D$  is the time between the arrival of a species at the CEMA and its recorded risetime at the oscilloscope.  $T$  is the true travel time of the field desorbed species.

preselected species, and the gate pulse will be assured of appearing at the proper time.

It is also convenient to have a visual display of the gate-pulse position, so that it can be adjusted to coincide with the appearance, on the oscilloscope sweep, of a species of interest. This is easily accomplished by Z-axis modulating the oscilloscope beam to maximum intensity at the position, and for the duration, of the gate pulse. But the Z-axis input of the oscilloscope does not usually include the delay  $T_V$  encountered by the signal from the CEMA, when it is routed through the oscilloscope's vertical amplifier. Therefore, a delay ( $= T_V + T_D$ ) must be inserted in series with the Z-axis input in order to correctly display the position of the gate pulse on the oscilloscope sweep. Figure 21(d) shows, schematically, the intensified portion of the sweep corresponding to the gate pulse position when the gate-pulse delay generator is set for zero delay, and when it is adjusted to coincide with the appearance of a species of interest.

Because the gate position can be visually displayed, it is not really necessary to know the travel time of a species in advance. Instead, the position in time of the selected species can be noted during a desorption event. Then, the tip voltage can be lowered, to prevent further desorption, and the gate-pulse delay adjusted, while pulsing the tip, until the intensified portion of the sweep is correctly positioned. Raising the tip voltage to its previous value, permits desorption to be continued, while recording a time-gated image of the selected species. It should be mentioned that ion travel times cannot be measured when the CEMA is time-gated, because capacitive coupling of the gate pulse to the CEMA screen will saturate the output amplifier circuitry.

### 3. Mass Spectroscopy of Surface Species

#### A. Species identification

Field desorbed species are identified by their mass-to-charge ratios, calculated from (4). Their travel time from the tip to the detector can be directly measured from the sweep of an oscilloscope initiated by the desorption pulse, provided a fiducial marker is also displayed. The fiducial marker defines the zero of time, which corresponds to the arrival of the desorption pulse at the tip, so that accurate travel time measurements can be made. Since the d.c. specimen bias,  $V_{dc}$  of (4), can be measured with great accuracy by use of a precision voltage divider, the only remaining parameters of (4) affecting the accuracy of species identification are the ion drift distance, and the desorption pulse amplitude,  $V_p$ .

Although the tip-to-detector distance,  $R$ , can be accurately measured (and assumed to be a constant), the ion drift distance will differ from  $R$  by the spatial extent of the ion acceleration region in front of the tip. To minimize (and define) the extent of this region, a grounded electrode

containing a small aperture through which the ions pass is placed a small distance,  $d_0$ , from the tip. If fringing fields in the vicinity of the aperture are neglected, the ion will drift in field-free space over a distance  $(R - d_0)$ . Then (4) can be written:

$$\begin{aligned} \frac{m}{n} &= \frac{0.193}{(R - d_0)^3} (V_{dc} + V_p) T_D^2 \\ &= \frac{0.193}{R^2(1 - d_0/R)^2} (V_{dc} + V_p) T_D^2 \end{aligned} \quad (31)$$

where  $T_D$  is the ion travel time in the drift region. If  $T_0$  is the travel time of the ion in the acceleration region and  $T$  its measured travel time:

$$T = T_0 + T_D. \quad (32)$$

Combining (31) and (32) yields

$$\frac{m}{n} = \frac{0.193}{R^2(1 - d_0/R)^2} (V_{dc} + V_p) T^2 (1 - T_0/T)^2. \quad (33)$$

In practice,  $d_0/R \ll 10^{-3}$  and, if  $T_0/T \ll 1$ , (33) becomes

$$\frac{m}{n} = \frac{0.193}{R^2} V_0 T^2 (1 - 2T_0/T) \quad (34)$$

where:

$$V_0 \equiv V_{dc} + V_p. \quad (35)$$

The ion travel time in the acceleration region,  $T_0$ , can be estimated for a confocal paraboloid geometry by integrating the ion's velocity over the distance  $d_0$  between the tip and an "apertureless" counter electrode at ground potential.<sup>(18,19)</sup> The result is:

$$T_0/T_t = F(r_t/d_0) \quad (36)$$

where  $T_0/T_t$ , plotted in Fig. 22, is a slowly varying function of  $r_t/d_0$ , and  $r_t$  is the tip radius.  $T_t$  is the ion's "terminal" travel time in the acceleration region, defined as the travel time of an ion of mass-to-charge ratio  $m/n$ , which has drifted over the entire distance  $d$  with maximum kinetic energy, i.e.  $E_{\max} = eV_0$ .  $T_t/(m/n)^{1/2}$  is plotted in Fig. 23 as a function of the total tip potential  $V_0$  for several values of  $d_0$ .

The last term in (34) can be evaluated using Figs. 22 and 23 to find  $T_0$ , and measuring the travel time  $T$  of the corresponding species. For  $V_0 = 6$  kV,  $d_0 = 0.0005$  and  $m/n = 1$  ( $H^+$ ),  $T_0 = 0.46$  nsec and  $T = 110$  nsec. For  $m/n = 103$  ( $Rh^+$ ),  $T_0 = 4.7$  nsec and  $T = 1113$  nsec. Therefore,  $T_0/T < 10^{-3}$  over a wide range of  $m/n$  values, and the last term of (34) can usually be treated as a constant. Combining this term with the other

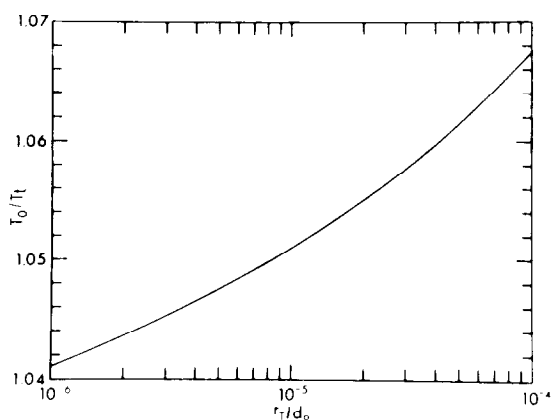


FIG. 22. The travel time,  $T_0$ , of an ion in the acceleration region in front of the tip relative to its "terminal" travel time  $T_1$ .  $T_1$  is defined as the drift time of the identical ion over an identical distance having its maximum (or terminal) kinetic energy ( $=qV_0$ ).  $T_0/T_1$  is plotted as a function of  $r_t/d_0$ , where  $r_t$  is the tip radius and  $d_0$  is the extent of the acceleration region. Concentric paraboloids of revolution were used to simulate the tip and an apertureless counter electrode spaced  $d_0$  apart.

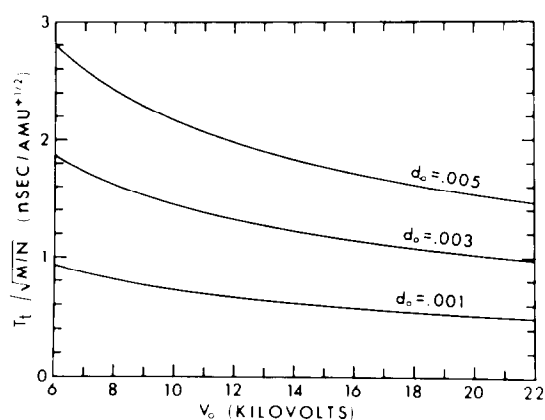


FIG. 23. The "terminal" travel time,  $T_1$ , of an ion of mass-to-charge ratio,  $m/n$ , for various distances,  $d_0$  (in meters). This figure plots (4) of the text with  $R = d_0$ .  $T_1$  is defined as the drift time of the ion over the distance  $d_0$ , assuming the ion has acquired its maximum or "terminal" kinetic energy ( $=neV_0$ ).

constants of (34), yields

$$\frac{m}{n} = 13.72(V_{dc} + V_p)T^2 \quad (37)$$

where a tip-to-detector distance,  $R = 0.118$  m, has been used,  $(V_{dc} + V_p)$  is measured in kilovolts and the travel time  $T$  is measured in microseconds.

The only other factor which can adversely affect mass identification is the measurement of the effective pulse amplitude  $V_p$ . Previously, it was shown that the measured amplitude of the desorption pulse overshoot (Fig. 12, upper waveform) is larger than the nominal pulse amplitude late in time. If a small number of surface species are removed during each desorption pulse ("gentle" desorption),

the desorption event can be inferred to have been initiated close to the maximum of the overshoot. Under such conditions,  $V_p$  can be considered equal to the maximum desorption pulse amplitude, and can be determined from the field emission method of §2. Alternatively,  $V_p$  can be determined<sup>(33)</sup> from a variation of an established calibration procedure,<sup>(34)</sup> by desorbing a known species from the tip. Hydrogen is a particularly suitable calibration species, since it is usually present in stainless steel, ion-pumped, vacuum systems and desorbs over a wide field range as  $H^+$ , below the evaporation field of most substrates, even at 80 K.

Because the mass-to-charge ratio of the calibration species is known ( $m/n = 1$ ) and all other parameters of (37) can be measured, an effective pulse amplitude,  $V_p$ , can be directly calculated from (37) for each desorption event, i.e.

$$V_p = \frac{0.073}{T^2} - V_{dc}. \quad (38)$$

Since  $H^+$  is removed from the surface over a wide range of fields, several values for  $V_p$  can be obtained by keeping the pulse amplitude constant and increasing  $V_{dc}$  in small increments. The average value of  $V_p$  obtained by this procedure can be associated with a specific pulse-cable charging voltage. Because experimental conditions often require the use of desorption pulses of different amplitude, an effective pulse amplitude  $V_p$  can be determined for several different values of the pulse cable charging voltage ( $V_{charging}$  of Fig. 9). Then, a so-called pulse-factor,<sup>(34)</sup>  $\alpha$ , can be defined in terms of the measured charging cable voltage such that:

$$V_p = \alpha V_{charging}. \quad (38a)$$

In the previous discussion, it was assumed that the effective desorption pulse amplitude  $V_p$  was independent of the nature of the desorbing species. In fact, this may not be the case. A species with a small  $m/n$  value (like  $H^+$ ) will travel quickly through the acceleration region in front of the tip. Therefore, it will experience less of the temporal variation in amplitude of the desorption pulse overshoot than a species which travels more slowly, e.g.  $Rh^+$ . The result is that the effective desorption pulse amplitude will actually depend upon the  $m/n$  value of the desorbing species.<sup>(35)</sup> By choosing a calibration species other than  $H^+$ , with an  $m/n$  value closer to that of a particular species of interest, a more accurate value of  $V_p$  can be obtained. However, since the variation of  $V_p$  with  $m/n$  is usually small over the range of species normally encountered,  $V_p$  can be considered to be independent of  $m/n$ . That is, the pulse factor,  $\alpha$ , in (38a) can be treated as a constant.

The accuracy of species identification using  $H^+$  as a calibration species can be demonstrated by

comparing  $m/n$  values calculated from (37), with those of species expected to be present on the tip during a desorption experiment. Figure 24 shows an oscilloscope sweep obtained during a desorption experiment designed to detect changes in the composition of a tungsten surface after deuterium ion implantation. A fiducial pulse is displayed before the arrival of  $H^+$ , as well as a time and  $m/n$  scale. A species arrival is indicated by an abrupt step in the waveform. Vertical markers extending from the baseline to the waveform were added at the position of these steps. The twelve species corresponding to the marked positions, with  $m/n$  ratios calculated from (37), are given at the left side of the figure. The abundance of an individual species is proportional to the height of its "step". It should be noted that several of the species marked in Fig. 24 have small, identical, abundances. Table 3 sum-

marizes these species and their abundances.

The identical signal levels observed for  $m/n = 3, 16, 18, 19$  and  $114$  in Fig. 24 correspond to the detection of one ion at the CEMA and can, therefore, be ignored. By comparison, the  $H^+$  signal corresponds to forty-seven detected ions. If the CEMA had a detection efficiency of 100 per cent, the number of detected ions, at a given  $m/n$ , would be equal to the absolute abundance of that species within the area of the tip observed at the CEMA. Since the detection efficiency will be less than 100 per cent, but is assumed to be independent of  $m/n$ , only relative abundances can be determined with the Imaging Atom-Probe technique.

### B. Time-of-flight measurements

There are three basic time-of-flight measure-

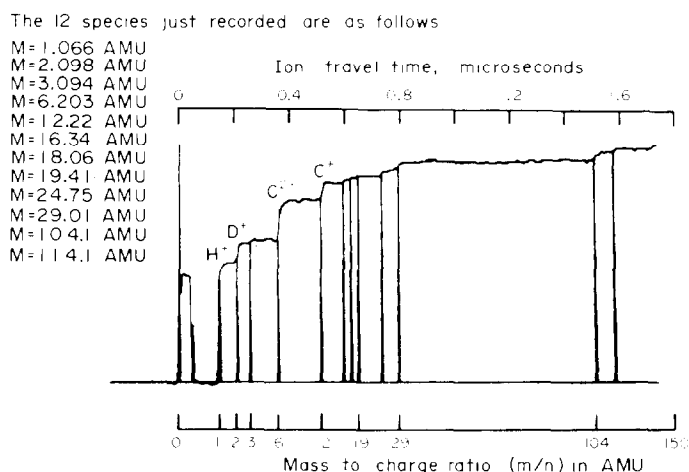


FIG. 24. A typical oscilloscope time sweep displaying the output of the amplifier of Fig. 19 during a desorption event. A mass scale and the calculated  $m/n$  ratios of the arriving species have been added for clarity. A fiducial pulse, coincident in time with the desorption pulse, is displayed to indicate the zero of time. The waveform was recorded at  $200 \text{ nsec/cm}$  with a Teletronix W2221 waveform digitizing system.

TABLE 3. The species recorded during the time sweep of Fig. 24.  $m/n$  values were calculated from (37) of the text. The most probable species corresponding to the calculated  $m/n$  value are given, together within  $m/n$ . Species abundance (in terms of number of ions detected) is also shown, based on a measured signal level corresponding to the detection of one ion.

Calculated $m/n$ (amu)	Number of ions detected*	Most Probable Species	Most Probable $m/n$ (amu)
1.1	47	$H^+$	1.0
2.1	7	$D^+, H_2^+$	2.0
3.1	1	$H_3^+, HD$	3.0
6.2	16	$C_2^+$	6.0
12.2	6	$C^+$	12.0
16.3	1	$O^+$	16.0
18.1	1	$H_2O^+$	18.0
19.4	1	$H_3O^+$	19.0
24.7	2	$C_2^+$	24.0
29.0	2	$CO^+$	28.0
104.1	2	$W_3O_3^{4+}$	105.0
114.1	1	?	

\*Based on a measurement of the signal amplitude corresponding to a simultaneous observation of one image spot at the detector ( $\approx 0.005 \text{ V/image spot}$ ).

ments which can be made with the Imaging Atom-Probe. Although travel time spectra are recorded for each type of measurement, the three measurements differ in procedure and ultimate aim. The first measurement is specifically concerned with determining the relative abundances of all species which reside *on* the first layer of lattice atoms, defining the "first layer" of the specimen surface. Since this layer will primarily consist of weakly bound residual gas species, desorption of this layer is assumed to be possible without disturbing the underlying substrate lattice. The second measurement is concerned with the relative abundance of each species contained within subsequent, individual atomic layers of the substrate. By field-evaporating the substrate, one layer at a time, and recording the abundance of each species within each layer, a depth profile of the near surface region can be obtained. The third measurement is concerned with determining an average composition for the near surface region of the lattice. In this case, the abundance of each species is averaged over all desorbed layers.

### C. "First layer" composition

In the absence of a desorption field, species characteristic of the ambient environment will adsorb on the tip surface with a probability that will generally depend on their background partial pressure, the tip temperature and the surface coverage. In addition, weakly bound lattice atoms may migrate over the surface with energy supplied, thermally. In turn, all species may migrate over the surface until their position is fixed by chemical or structural interactions with the lattice. In a very real sense, the first atomic layer of the tip is a microcosm of the ambient environment and, as such, its composition will often be of great interest.

The accuracy of the composition determination of the first layer is based upon the premise that the most tightly bound species of the first layer will always desorb at a field less than that necessary to field evaporate the lattice. In the case of strong chemical interactions with lattice atoms, as in chemisorption and the formation of chemical compounds with metal atoms, this assumption may fail; but, in general, it appears to be valid. The importance of this assumption lies in the ability to experimentally define the first layer of the specimen by distinguishing between species which reside *on* the first layer of lattice atoms and those which reside *within* the first layer of lattice atoms. Since the species which reside on the first layer are assumed to be weakly bound and relatively easy to ionize, they should desorb at characteristic fields well below the evaporation field of the lattice. Therefore, the analysis of the "first layer" begins by desorbing at a very low field ( $< 0.1 \text{ V/\AA}$ ) where the probability of removal of *any* species from the surface is known (from experience) to be

zero. A mass spectrum is recorded at this field, and the d.c. bias ( $V_{dc}$ ) raised<sup>(36)</sup> by an amount which is small compared to the measured overshoot of the desorption pulse. Typically,  $V_{dc}$  is incremented by 50–100 V before a new spectrum is recorded. Using a small increment in specimen bias increases the probability that species will desorb at a pulse amplitude only minimally different from the maximum amplitude of the initial overshoot. This, in turn, assures maximum mass resolution in each spectrum recorded. The d.c. bias is incremented, and a mass spectrum is recorded, for each new desorption field until a tip bias  $V_m$  is reached which is 50–100 V less than that previously measured for the evaporation of metal atoms of the lattice.<sup>(37)</sup> It is assumed that at this field all species which resided on the first layer of lattice atoms were desorbed. Since species were desorbed over a range of fields, the abundance of each species residing on the first layer is obtained by summing the abundance recorded for each species in the individual desorption spectra at each field.

If species abundance is desired as a function of desorption field, i.e. the binding of a species to the surface is wanted as a function of field, the abundance obtained for each species at each tip potential can be plotted as a function of tip potential ( $V_{dc} + V_p$ ). If the evaporation field for the lattice  $F_L$  corresponding to a measured evaporation bias  $V_L$  is known, the desorption field  $F$ , at each value of specimen potential, can be calculated, since

$$F = \frac{V_{dc} + V_p}{V_L} F_L. \quad (39)$$

### D. Composition of one atomic layer

The composition of an individual atomic layer of the lattice can be accurately obtained by summing the abundance obtained for each species recorded during the successive desorption events required to remove the layer *provided, of course, that all species which are contained within the layer are removed as positive ions and detected with the same efficiency*. For a refractory metal substrate, containing easily ionized, low  $Z$  impurities the high desorption field required to evaporate the lattice will probably guarantee the removal of all species within the layer as positive ions. However, for low  $Z$  substrates containing high  $Z$  impurities, the lower desorption field used to evaporate the substrate will probably guarantee the removal of all species by lattice dissolution, but may not be sufficient to insure complete ionization of all high  $Z$  impurities. Since little is known about the exact mechanism of field desorption, the possibility of selective ionization cannot be ignored, and since the CEMA cannot detect low energy neutrals, composition determinations made on materials containing species of widely different ionization potentials may be subject to large statistical errors. In the following pages, it will be tacitly assumed that all substrate species which are exposed to a field sufficient to evaporate the

lattice, will be desorbed as positive ions. This assumption guarantees that the measured composition of any atomic layer of the substrate will be a direct reflection of the species which were present.

The procedure used to obtain the composition of a single atomic layer of the specimen will be essentially that described in the last section, with the use of a tip potential large enough to establish the required evaporation field. In practice, a fraction of an atomic layer is removed with each desorption pulse, and the specimen bias slightly increased before the next desorption event is initiated. This procedure insures that desorption will occur close to the maximum pulse amplitude, so that mass resolution will be optimized. The removal of one atomic layer of the specimen can be determined by observing the collapse of a prominent net plane in the non-gated desorption image of the lattice which is simultaneously recorded. Since the layer spacing of prominent net planes are known, the depth probed into the lattice is also uniquely determined. Figure 25 shows a series of desorption images of tungsten in which the gradual collapse of the (110) net plane is followed. The last atoms of the plane are seen to evaporate at  $V_0 = 11.415$  kV. Of course, one atomic layer will not have been removed uniformly over the entire tip surface when the collapse of the net plane is noted. But, in the immediate vicinity of

the net plane, the assumption that only one layer has been removed will be quite accurate. It is this feature of Imaging Atom-Probe mass spectroscopy, i.e. "built-in" depth markers (the collapse of an identifiable net plane), which permits species abundance to be recorded as an extremely accurate function of depth, with essentially angstrom depth resolution. This depth profiling capability is absolutely unique to the Atom-Probe Technique, and has been demonstrated in an Imaging Atom-Probe study of deuterium implantation in tungsten which will be reviewed in a later section.

Often, the amount of lattice evaporation at a given specimen bias will be observed to be a function of the time between each desorption event. This effect is particularly noticeable if hydrogen is present on the substrate. In the presence of hydrogen, the desorption field is known to be lowered,<sup>138)</sup> due to a weakening of surface metal-metal bonds (perhaps encouraged by the formation of metal hydrides). If hydrogen preferentially absorbs in certain crystallographic regions of the tip, metal atoms in those regions may be seen to field evaporate before those in other regions. The result is the appearance of highly localized, regional desorption, which may move from region-to-region of the tip as appropriate desorption conditions are established.

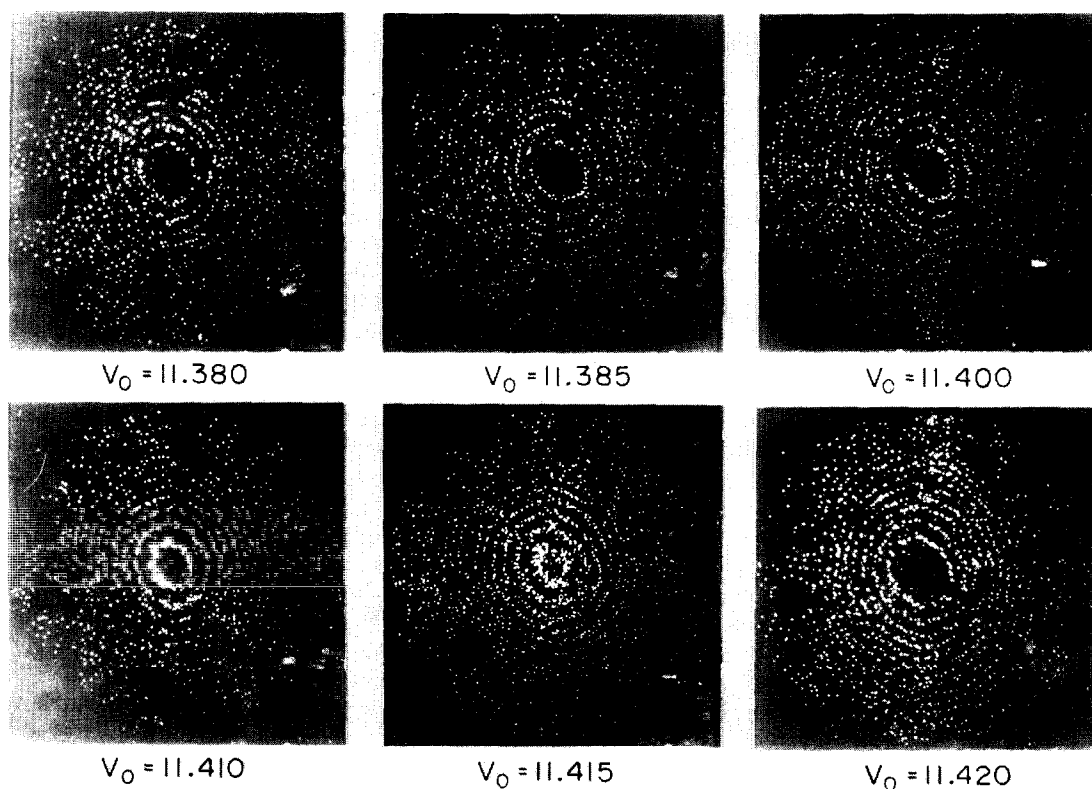


FIG. 25. A sequence of time-gated field desorption images of (110) tungsten in which the tip potential was incremented between each desorption event by increasing the d.c. bias. Each time-gated image includes only  $W^{3+}$  and  $W^{4+}$  image spots. The collapse of the (110) net plane can be seen at  $V_0 = 11.415$  kV.

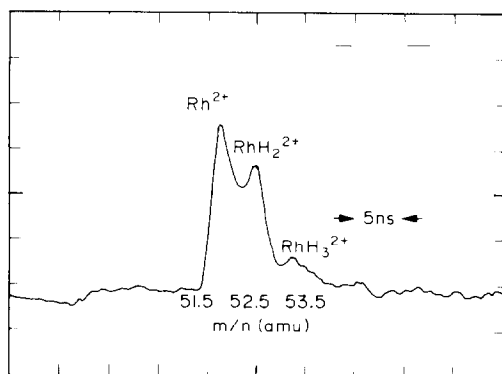


FIG. 26. An oscilloscope time sweep (expanded around the arrival of  $\text{Rh}^{2+}$ ) showing the species recorded during the desorption of one atomic layer of a rhodium specimen. A hydrogen pressure of  $8 \times 10^{-10}$  Torr produced the species at  $m/n = 51.5$  and  $52.5$ . Because chemically stable hydrides of rhodium are unknown, it is assumed that rhodium hydrides are unique to the high electric fields generated at field-ion specimen surfaces.  $V_{dc} = 7.1$  kV,  $V_{charging} = 2.0$  kV,  $T = 80^\circ\text{K}$ . The waveform in the figure was recorded with a Teletronix W2221 waveform digitizing system at a sweep rate of 5 nsec/cm.

Figure 26 shows the species recorded when a single layer of a rhodium specimen was field-evaporated in a residual gas pressure of  $8 \times 10^{-10}$  Torr of hydrogen. The usual oscilloscope time sweep has been expanded to 5 nsec/division around the arrival of the dominant substrate species,  $\text{Rh}^{2+}$ . Because a rapid signal decay was desired, and the signal amplitude was large, a 40 pF coupling capacitor and a  $50 \Omega$  input resistor were used in place of the 1500 pF and  $1 \text{M}\Omega$  resistor of Fig. 19. The species  $\text{RhH}_2^{2+}$  appears to be a field-induced hydride, since no naturally occurring hydride of rhodium is known. The small peak at  $m/n = 53.5$  is tentatively identified as another field-induced hydride,  $\text{RhH}_3^{2+}$ . When the ion pump of the spec-

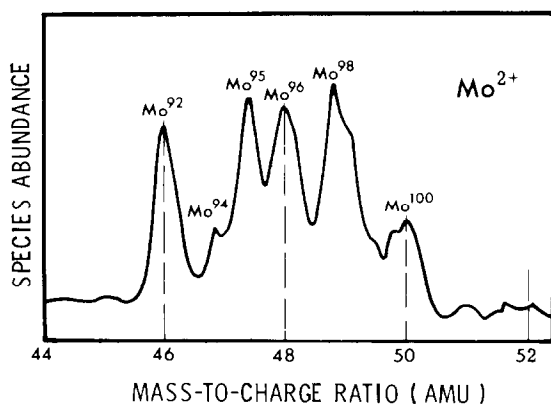


FIG. 27. A  $\text{Mo}^{2+}$  isotopic distribution. The evaporation rate was chosen to remove approximately one monolayer. Sixty consecutive evaporation events at a fixed specimen potential ( $V_{dc} = 6.65$  kV,  $V_{pulse} = 1$  kV) were recorded with Tektronix W2221 Waveform digitizing system. Time sweeps were added to form the composite waveform shown. Axes and labeling were subsequently added.

trometer chamber was valved off, both hydride species disappeared, leaving only  $\text{Rh}^{2+}$  in the desorption spectrum. Opening the ion pump caused the hydride species to reappear, confirming that gas phase hydrogen, regurgitated from the ion pump, and not hydrogen migrating from the tip shank was responsible for the production of these species.

Since lattice evaporation is usually observed to occur during several consecutive desorption events at the same desorption field, it is usually advisable to pulse the tip several times, and sum the resulting spectra, before increasing the tip potential. Figure 27 shows the result of summing sixty mass spectra of a field evaporated molybdenum tip taken at the same specimen potential. Here, the detector decay time was again chosen as 2 nsec (a 40 pF coupling capacitor and a  $50 \Omega$  input resistor in the amplifier of Fig. 19).

#### E. Average composition of the near surface region

By determining the abundances of all species in each atomic layer evaporated, and summing over many layers, an average composition of a volume of the near surface region can be obtained. This is an obvious extension of the previous type of measurement, but since the tip potential must be changed as the lattice is evaporated, to maintain a constant desorption field as the tip radius increases, ion travel times for the same species will become progressively shorter. This precludes the possibility of simply adding successive waveforms, as in Fig. 27. Instead, species must be identified, and their abundances recorded for each desorption event, and then the individual abundances added to form an abundance histogram characteristic of the volume probed.

In the previous paragraphs, the basic measurements resulting in time-of-flight mass spectra were described, with the desorption image used only in a general way to monitor the collapse of a prominent net plane, so as to obtain an accurate measurement of the depth probed within the lattice. Used in this way, the resolution of the desorption image is, itself, unimportant. But, if the imaging capability of the Imaging Atom-Probe is to be further exploited, image resolution becomes important, and an estimate of its magnitude becomes essential.

### 4. Field Desorption Imaging

#### A. Image resolution

In the absence of other constraints, the resolution of a field-desorption (or field-ion) image will ultimately depend on the spatial resolution of the detector used for imaging. Figure 28 is a schematic drawing of a CEMA detector, where  $D_0$  is defined as the distance between the centers of adjacent channels. For simplicity, the channels of the first plate have been drawn perpendicular to the input web. In practice, however, the channels of the

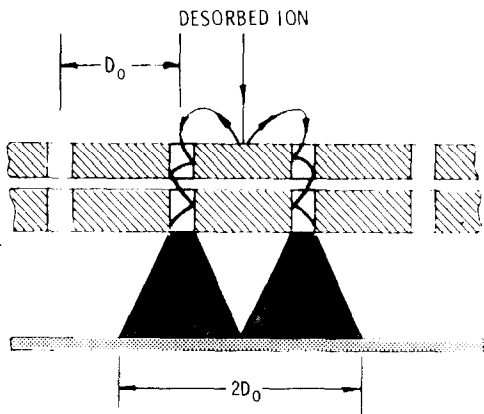


FIG. 28. A schematic drawing of the CEMA detector showing a desorbed species arriving at the input web between adjacent channels (spaced a distance  $D_0$  apart). The electron cloud emerging from each adjacent, activated channel of the second CEMA plate is assumed to diverge to produce an image spot of diameter  $D_0$ . The resulting image spot diameter will be  $2D_0$ , as shown.

first plate are usually inclined with respect to the surface of the input web to discourage incoming ions from passing through a channel of the first plate without striking its active wall. In Fig. 28, a "worst case" situation is illustrated in which a desorbed species strikes the input web between channels with the resulting secondary electrons initiating electron cascades in adjacent channels. If the electron cloud emerging from each active channel of the second plate diverges to produce an image spot of diameter  $D_0$  at the phosphor screen, the effective diameter of the image spot, associated with the desorbed species, will be  $2D_0$ . For most commercial CEMA's  $D_0 = 50 \mu$ , so that worst case image spot diameters should be of the order of 0.1 mm (in fact, this appears to be the average image spot diameter measured in typical desorption micrographs). It should be emphasized that the diameter of *all* image spots appearing in a single pulse desorption micrograph will be approximately  $2D_0$ . This means that random noise image spots will have diameters which are indistinguishable from those produced by desorbed species, so that the contribution of random noise to the desorption image cannot be determined by image spot diameter, alone.

It is apparent from Fig. 28, that in order to minimally resolve two adjacent surface species, the center-to-center separation of their impact positions at the input web of the CEMA must be at least  $2D_0$ . To find the equivalent minimum resolvable separation,  $D_t$  of the two species on the tip surface prior to desorption, their separation at the CEMA is divided by the image magnification, i.e.

$$D_t = \frac{2D_0}{R} \beta r_t \quad (40)$$

where  $r_t$  is the tip radius,  $R$  is the tip-to-CEMA distance and  $\beta$  is the "image compression factor",

which describes the desorbing species departure from exact radial projection.<sup>(39)</sup> For typical values of  $\beta = 1.5$ ,  $r_t = 250 \text{ \AA}$ , and  $R = 0.118 \text{ m}$ ,  $D_t = 0.3 \text{ \AA}$ . Since  $D_t$  is smaller than the expected separation of any two species of interest on the tip surface, the CEMA itself should not limit the resolution of a desorption image. What will limit the resolution of a desorption image is the finite component of velocity,  $V_t$ , parallel to the tip surface, which is associated with each desorbed ion. The effect of a tangential velocity component will be to introduce an uncertainty in the position of the desorbed species at the input web of the CEMA. If it is assumed that the transverse velocity component of the desorbed ion is independent of the position of the species on the surface prior to desorption, each desorbed ion will have traveled an identical distance

$$r = v_t T \quad (41)$$

parallel to the tip surface in the time  $T$  that it takes it to reach the CEMA. Practically, this means that a desorbed ion can strike the input web of the CEMA anywhere within a disk of diameter

$$D = 2r = 2v_t T = 2v_t R \left( \frac{m}{2neV_0} \right)^{1/2} \quad (42)$$

where the ion's travel time  $T$  (3) has been explicitly used.  $D$  defines the diameter of a "disk-of-confusion" associated with each surface species imaged at the CEMA.

In the field-ion microscope, many ionized ambient gas atoms will arrive each second at random locations within a similarly defined disk-of-confusion associated with each imaged surface species. As a result, the true diameter of each disk will be visible in the ion image, and the resolution of the field-ion image (which is determined by the degree of overlap of adjacent disks) will be directly observable. In the field-desorption microscope, the situation is quite different. Since all disk-of-confusion will contain only one image spot of identical diameter, the actual diameter of each disk can not be observed, so that the resolution of the desorption image cannot be directly determined. Stated in another way, the relative image spot positions which are observed in a desorption image, will be uncertain to within the diameter,  $D$  of the disk-of-confusion (42) associated with each desorbed species. Since each image spot position will be unknown to within a factor  $D$ , the relative positions of species on the tip surface cannot be determined to better than

$$D_s = D/(R/\beta r_t) \quad (43)$$

where the quantity in parenthesis is the magnification of the Imaging Atom-Probe.

One exception should be noted. If the diameter of the disk-of-confusion happens to be equal to, or smaller than the inherent spatial resolution of the

CEMA, the observed image spot positions will accurately reflect the relative positions of the species on the surface which produced them. Only in this particular case will the single pulse desorption image have the chance of providing an unambiguous mapping of the relative location of surface species.<sup>(40)</sup>

There are two major effects which will determine the disk-of-confusion diameter by contributing to the tangential velocity component of the desorbing ion as it leaves the surface.<sup>(40)</sup> The first is due to the finite de Broglie wavelength of the desorbing species. If a species is constrained to a region of lateral extent  $\Delta y$  on the tip prior to desorption, its transverse momentum at desorption,  $\Delta P_y$ , will be given by the Heisenberg uncertainty principle, i.e.

$$\Delta y \Delta P_y = m \Delta y \Delta v_t = \hbar/2 \quad (44)$$

where  $m$  is the mass of the desorbed species,  $\Delta v_t$  is the uncertainty in its transverse velocity, and  $\hbar$  is Planck's constant divided by  $2\pi$ . The diameter of the resulting disk-of-confusion due to diffraction effects alone will be given by (42) and (44), i.e.

$$D_H = 2v_t T = \frac{\hbar R}{M \Delta y} \left( \frac{M}{2neV_0} \right)^{1/2}. \quad (45)$$

The other contribution to the diameter of the disk-of-confusion results from a spread in the desorbing ion's thermal velocity component,  $\Delta v_{Th}$ , parallel to the tip surface. Since the species is assumed to be thermally accommodated to the tip at temperature  $T$  prior to desorption, its kinetic energy parallel to the tip surface at desorption will be

$$\frac{1}{2} m (\Delta v_{Th})^2 = kT \quad (46)$$

where  $k$  is Boltzmann's constant. Combining (42) and (46) yields

$$D_T = 2\Delta v_t T = R \left( \frac{8kT}{2neV_0} \right)^{1/2} \quad (47)$$

which is the diameter of the disk-of-confusion due to thermal effects, alone.

Because of the statistical nature of  $D_H$  and  $D_T$ , the total diameter of the disk-of-confusion,  $D$ , is best obtained from a vectorial sum<sup>(41)</sup> of the individual contributions, i.e.

$$D^2 = D_H^2 + D_T^2 \quad (48)$$

or

$$D = \frac{R}{(2neV_0)^{1/2}} \left( \frac{\hbar^2}{M(\Delta y)^2} + 8kT \right)^{1/2}. \quad (49)$$

The tip potential at desorption,  $V_0$ , can be related to the desorption field  $F_0$  and the tip radius  $r_t$  by the expression<sup>(18,19)</sup>

$$V_0 = \frac{-F_0 r_t}{2} \ln(r_t/2d_0) \quad (50)$$

where  $d_0$  is the extent of the acceleration region in front of the tip. Combining (49) and (50), gives

$$D = \frac{R}{(-F_0 n e r_t \ln(r_t/2d_0))^{1/2}} \left( \frac{\hbar^2}{m(\Delta y)^2} + 8kT \right)^{1/2}. \quad (51)$$

The first term in the parenthesis of (51), due to diffraction, will always be small compared to the second term, even for field desorbed hydrogen ( $m = 1$  amu, and  $\Delta y \approx 1$  Å). Therefore, an effective tip temperature,  $T_{eff}$ , can be defined above which diffraction effects can be ignored. Assuming that the diffraction contribution will be equal to the thermal contribution at this temperature, for  $H^+$

$$T_{eff} = \frac{\hbar^2}{8km(\Delta y)^2} \approx 6^\circ K. \quad (52)$$

Since  $T_{eff}$  is so small, the diameter of the disk-of-confusion will usually be determined entirely by the thermal contribution, i.e.

$$D = R \left( \frac{8kT}{-F_0 n e r_t \ln(r_t/2d_0)} \right)^{1/2}. \quad (53)$$

Consider three cases of interest: The desorption image of a tungsten lattice (assuming  $W^{3+}$  as the imaging species), the desorption image of field adsorbed helium on tungsten at the desorption field of tungsten (5.7 V/Å), and the desorption image of hydrogen ( $H^+$ ) at a very low desorption field, 1 V/Å. Table 4 lists the disk of confusion

TABLE 4. The disk-of-confusion diameter (at the CEMA) for three desorbed species at four tip temperatures and three tip radii. The numbers in parenthesis are the equivalent uncertainty in species position at the tip (in angstroms) surface obtained by dividing the diameter of the disk-of-confusion by the magnification of the instrument. All other image spot diameters are given in millimeters.

	10°K	21°K	78°K	300°K
$R = 100\text{Å}$ BIV (helium) = 2.6 kV				
$W^{3+}$	0.07(0.09)	0.10(0.13)	0.19(0.24)	0.38(0.48)
$He^+$	0.12(0.15)	0.17(0.22)	0.34(0.43)	0.66(0.84)
$H^+$	0.29(0.37)	0.42(0.53)	0.81(1.0)	1.6(2.0)
$R = 250\text{Å}$ BIV (helium) = 6.0 kV				
$W^{3+}$	0.05(0.16)	0.07(0.22)	0.13(0.41)	0.25(0.79)
$He^+$	0.08(0.25)	0.11(0.35)	0.22(0.70)	0.44(1.4)
$H^+$	0.19(0.60)	0.27(0.86)	0.53(1.7)	1.0(3.2)
$R = 400\text{Å}$ BIV (helium) = 9.1 kV				
$W^{3+}$	0.04(0.20)	0.05(0.25)	0.10(0.51)	0.20(1.0)
$He^+$	0.06(0.30)	0.09(0.46)	0.18(0.91)	0.35(1.8)
$H^+$	0.15(0.76)	0.22(1.1)	0.43(2.2)	0.84(4.3)

diameter (in millimeters) for each of these cases at four different temperatures, and three tip radii. Each number in parenthesis in Table 4 is the equivalent, minimum resolvable separation of two species on the tip surface (in angstroms), calculated from (43) with  $\beta = 1.5$ . The helium best image voltage<sup>(42)</sup> (BIV) for a field-ion image at each tip radius was calculated using (50) with  $F_0 = 4.5 \text{ V/\AA}$ , and  $d_0 = 0.0005 \text{ m}$ . As in the case of the field-ion image, the desorption image disk-of-confusion decreases with increasing tip radius, while the minimum resolvable species separation on the tip surface correspondingly increases.

For a tungsten  $\text{W}^{3+}$  image, the disk-of-confusion diameter at temperatures below  $21^\circ\text{K}$  is less than the intrinsic spatial resolution of the CEMA referred to the tip ( $D_t$ , (40)). Since  $D_t$  is much smaller than the lattice constant of tungsten, the  $\text{W}^{3+}$  desorption image (below  $21^\circ\text{K}$ ) should accurately reflect the relative positions of the surface tungsten atoms prior to desorption. Consequently, any "randomness" in the observed position of individual image spots will be due to an effect other than image resolution. For example, non uniform field evaporation, or migration of species over the surface prior to desorption. For desorbed helium at the evaporation field of tungsten, and for  $\text{H}^+$  at a field of  $1 \text{ V/\AA}$ , Table 4 shows that image resolution is worse, but is still less than the lattice constant of most metals, at least at small tip radii. It should be recognized that the resolution requirements on a single pulse desorption image must necessarily be more severe than those imposed on repetitive images which can be integrated, i.e. images of adsorbed species which can be repeatedly adsorbed, presumably at the same surface locations, and then desorbed. If such adsorption-desorption cycles are repeated, and the resulting single pulse desorption images integrated, the disk-of-confusion associated with each adsorbate position will be "filled" with image spots, defining, at least in theory, the position of each adsorption site on the surface. Of course, this assumes that the adsorbate will desorb as a positive ion well below the evaporation field of the lattice

### B. Time-gated imaging

If many layers of a metal lattice are field evaporated, and the resulting desorption images integrated, the composite desorption image which results should display no detail, since metal atoms in successive layers will generally desorb from non-identical lattice positions. As expected, if the high detector gain required to record the single-pulse submonolayer desorption images of Fig. 25 is used to record multilayer desorption events, the photographic film is seen to saturate and display a uniform, contrastless white background. But if the CEMA gain is decreased from approximately  $10^7$  to  $10^4$  and a slow speed photographic emulsion used, an unexpected image emerges<sup>(28,43-45)</sup> which contains

more detail than single layer desorption images. This so called *multilayer* desorption image,<sup>(43)</sup> containing prominent ring structure, and a complex network of dark and light intersecting lines, displays a surprising variation in ion density over the surface.

In order to observe the largest possible fraction of the entire surface during multilayer imaging, the CEMA detector of the Imaging Atom-Probe can be placed closer to the tip than its optimum distance of  $0.118 \text{ m}$ . For example, by choosing a tip-to-CEMA distance,  $R = 0.038 \text{ m}$ , a  $45^\circ$  image half-angle can be subtended. If time gating is used only to separate metal atoms of the lattice from background CEMA noise, the poor mass resolution resulting from the non-optimum position of the CEMA is tolerable, and a  $250 \text{ nsec}$  gate pulse can be used to insure imaging of all metal species. Figure 29 shows a typical multilayer desorption image of (110) tungsten resulting from such an instrument modification under conditions of low detector gain. Two hundred desorption pulses were applied to the tip at a constant specimen bias of  $(V_{dc} + V_p) = 13.4 \text{ kV}$ . The resulting images, recorded at approximately  $18^\circ\text{K}$  and  $1 \times 10^{-9} \text{ Torr}$ , were integrated photographically. Although no exact measurement was made of the number of layers evaporated, the integrated image of Fig. 29 was estimated to represent the removal of 5-10 atomic layers. A prominent ring structure around the (110) poles is apparent, along with dark regions, indicative of low ion density. Figure 30 is another photographically integrated multilayer desorption image of the same tip, in which 20-30 (110) layers were estimated to have been removed, at an even lower detection sensitivity. Figure 31 is a helium ion image of the tip surface taken after the desorption image of Fig. 29.

There are two striking features of the multilayer desorption images of tungsten shown in Figs. 29 and 30. First, the images exhibit a prominent, bright ring structure about the (110) poles, with the innermost ring defining a dark, central region containing a few isolated image spots. Since these spots appear in an image which was gated for  $\text{W}^{1+}$  and  $\text{W}^{4+}$ , they cannot be caused by other species on the tip surface.<sup>(46)</sup> In addition to the ring structure, well defined dark regions of low ion density (only marginally apparent in Fig. 29, but obvious in Fig. 30) are present. These regions, always reproduced in multilayer desorption images of tungsten, can be considered to be a characteristic "fingerprint" of this metal. This latter feature of multilayer desorption images will be discussed shortly.

In the high gain, submonolayer desorption images of Fig. 25, the collapse of the (110) plane can be followed. Although a few image spots are always observed at the position of the plane center as the last atoms evaporate ( $V_0 = 11.415 \text{ kV}$ , Fig. 25), the image spot density appears to be greatest within a narrow annular ring about the plane center, with the region of greatest image spot

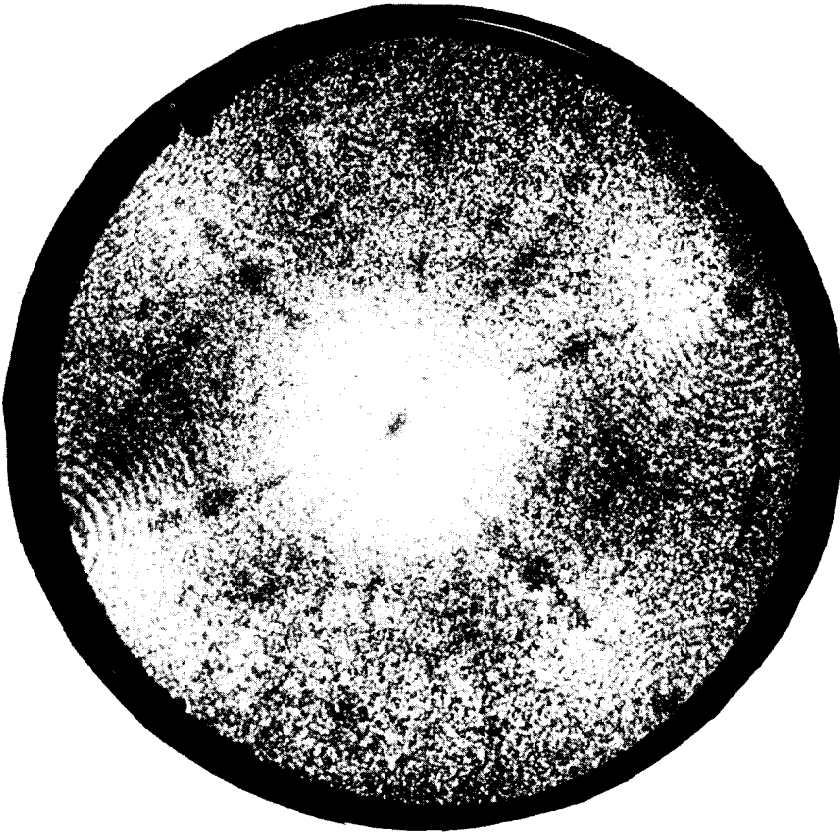


FIG. 30. A multilayer desorption micrograph gated for  $W^{3+}$  and  $W^{4+}$ . Ten desorption pulses were applied at a specimen potential ( $V_{dc} + V_p$ ) = 13.7 kV, followed by ten pulses at ( $V_{dc} + V_p$ ) = 13.75 kV. Approximately 10–20 layers were estimated to have been field-evaporated during the desorption sequence which immediately followed that of Fig. 29.

Experimental conditions were the same as for Fig. 29.



FIG. 29. A multilayer desorption micrograph gated for  $W^{3+}$  and  $W^{4+}$ . 200 desorption pulses were applied at a constant specimen potential ( $V_{dc} + V_p$ ) = 13.4 kV. Approximately 5–10 layers were estimated to have been field-evaporated during the desorption sequence. Tip-to-CEMA distance = 3.1 cm. CEMA gain  $\approx 10^6$ . The micrograph was recorded on Polaroid Type 55 (ASA 50) film.  $T = 18^\circ\text{K}$ ,  $p = 1 \times 10^{-9}$  Torr.

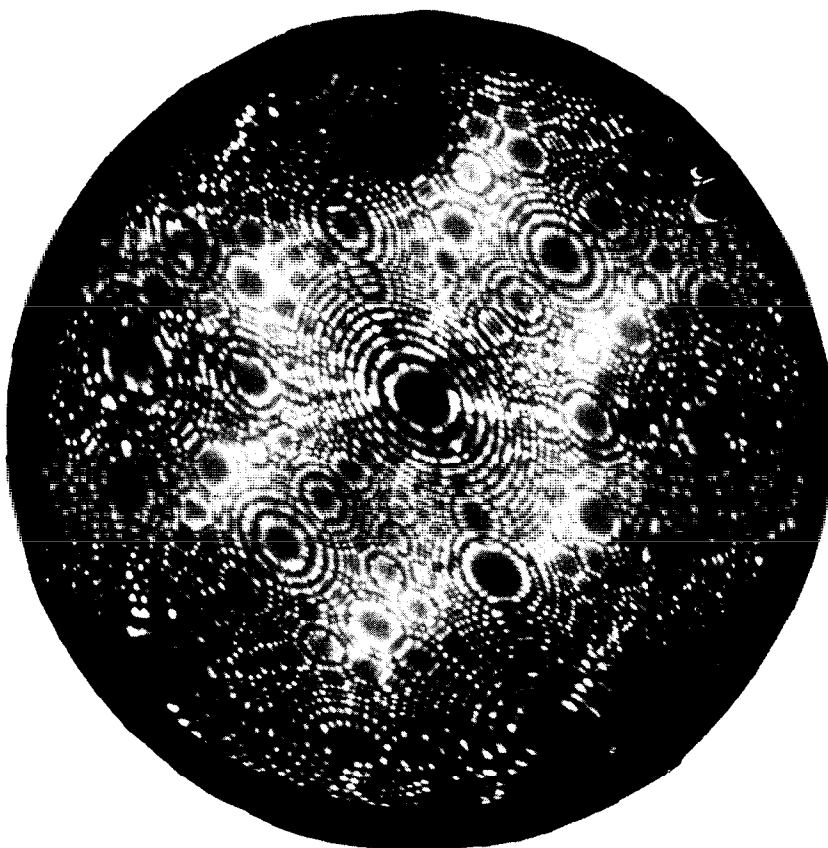


FIG. 31. A helium ion image of the tip shown in Figs. 29 and 30, taken after the multilayer desorption image shown in Fig. 29  $p_{\text{helium}} = 1 \times 10^{-5}$  Torr,  $T = 18^\circ\text{K}$ ,  $V_{\text{dc}} = 10.2$  kV.

density at the perimeter of the ring. An increase in spot density at the perimeter of a ring can also be observed in the prior micrograph of the sequence ( $V_0 = 11.410$  kV, Fig. 25), but not in earlier micrographs of the sequence. This suggests that the smaller the (110) plane becomes, the more an evaporated ion is deflected away from the plane center. Interestingly, this suggestion is not new, having been made almost 10 years ago in connection with probe hole "aiming" in the conventional, non-imaging atom probe.<sup>(18,47)</sup>

The inability to repeatedly detect evaporated metal atoms from the (110) plane after using a helium-ion image for probe-hole positioning in the Atom-Probe was originally<sup>(18,47)</sup> attributed to the electric field at the plane edge producing an anomalous ion trajectory in a general direction away from the plane center. But recently, in the first exhaustive discussion of desorption imaging, Waugh *et al.*<sup>(48)</sup> have expanded this concept to include directed, short range migration of a species over the surface *in a specific crystallographic direction prior to desorption*. Figure 32 shows, schematically, the postulated movement (due to polarization forces) of a desorbing species on a low index plane, from a kink-site position to a position on an adjacent ledge where it is more exposed to the applied field. Waugh *et al.* considered this

short-range field-induced migration to be a generalization of a concept, advanced by Muller,<sup>(49)</sup> to explain the existence of bright zone line decorations (due to displaced metal atoms of the lattice) commonly seen in field-ion micrographs.

If the directed migration hypothesis is correct, it might be expected to be a strong function of surface cleanliness and morphology, since foreign atoms adsorbed on the surface, or lattice atoms of different relative spacing, should directly affect the directed motion of a species on the surface prior to desorption. It is relatively easy to check the effect of adsorbed gas on the appearance of the desorption image, particularly for the case of helium field-adsorbed on tungsten. Tungsten can be field evaporated in the presence of helium, which will field adsorb at protruding kink-site atoms within the imaged area between each desorption event. Figure 33 shows a typical result, in which a multilayer desorption image of the tip of Fig. 31 is shown, taken in  $1 \times 10^{-5}$  Torr of helium. The image, gated for  $W^{3+}$  and  $W^{4+}$  alone,<sup>(50)</sup> shows almost complete randomization of the normally prominent ring structure around the close packed (110) poles. In Fig. 34, a similar effect is observed for iridium<sup>(50)</sup> (an f.c.c. metal), although the randomization of the ring structure at the center of the close packed (111) plane is not as pronounced. The lesser degree of

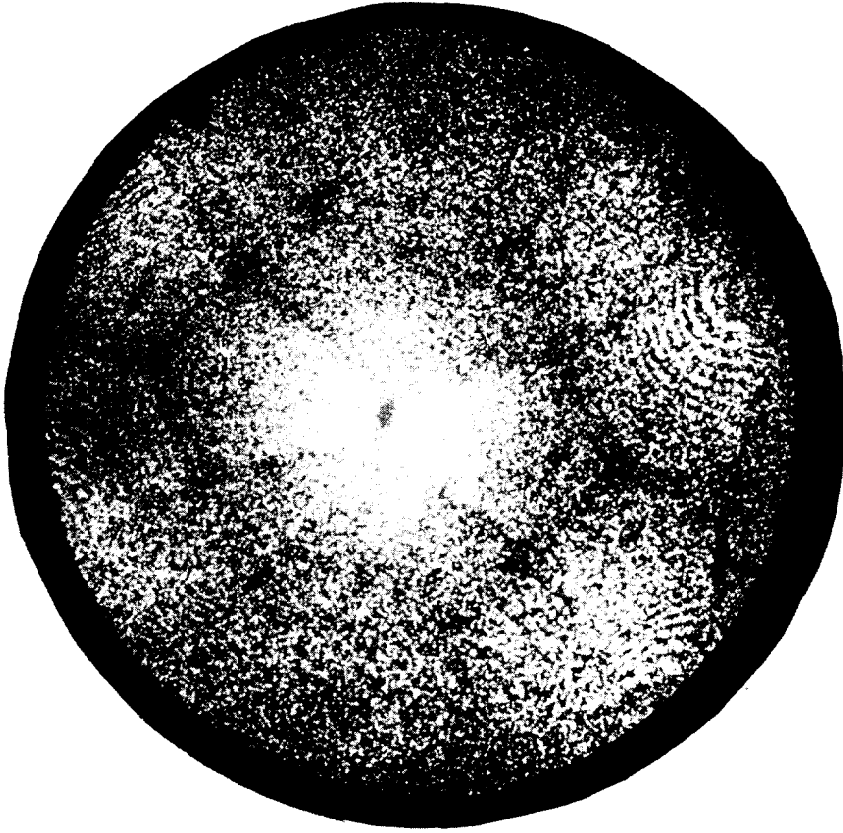


FIG. 33. A multilayer, time gated (for  $W^{3+}$  and  $W^{4+}$ ) image of the tip of Fig. 30, taken immediately after Fig. 30 by field evaporating in  $1 \times 10^{-5}$  Torr of Helium.  $He^+$  was observed in the mass spectra prior to time-gating for the tungsten species. Ten desorption images were superimposed (at  $V_{dc} = 11.10$  kV,  $V_{pulse} = 2$  kV) and then the d.c. tip bias was increased to 11.15 kV. Ten more images were then superimposed on the original ten. The detector gain was the same as for Fig. 30.

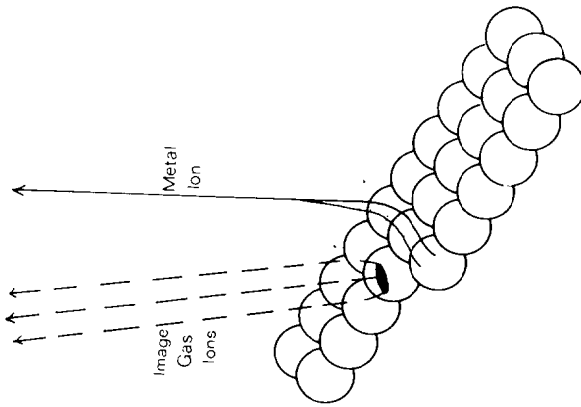


FIG. 32. The postulated "rolling" motion of an evaporating kink site atom up over the edge of the ledge in which it originates as a result of electrostatic polarization forces. "During this rolling motion it (the ion) will be channelled in a specific direction by its impenetrable near neighbors. The image gas ions from the atom originate in an ionization zone above the surface and follow a different trajectory to that of the metal ion, which moves on the surface and also may acquire tangential kinetic energy during this movement". This figure and the portion of the quoted caption is courtesy of A. R. Waugh, E. D. Boyes and M. J. Southon, University of Cambridge, Department of Metallurgy and Materials Science, Cambridge, England.

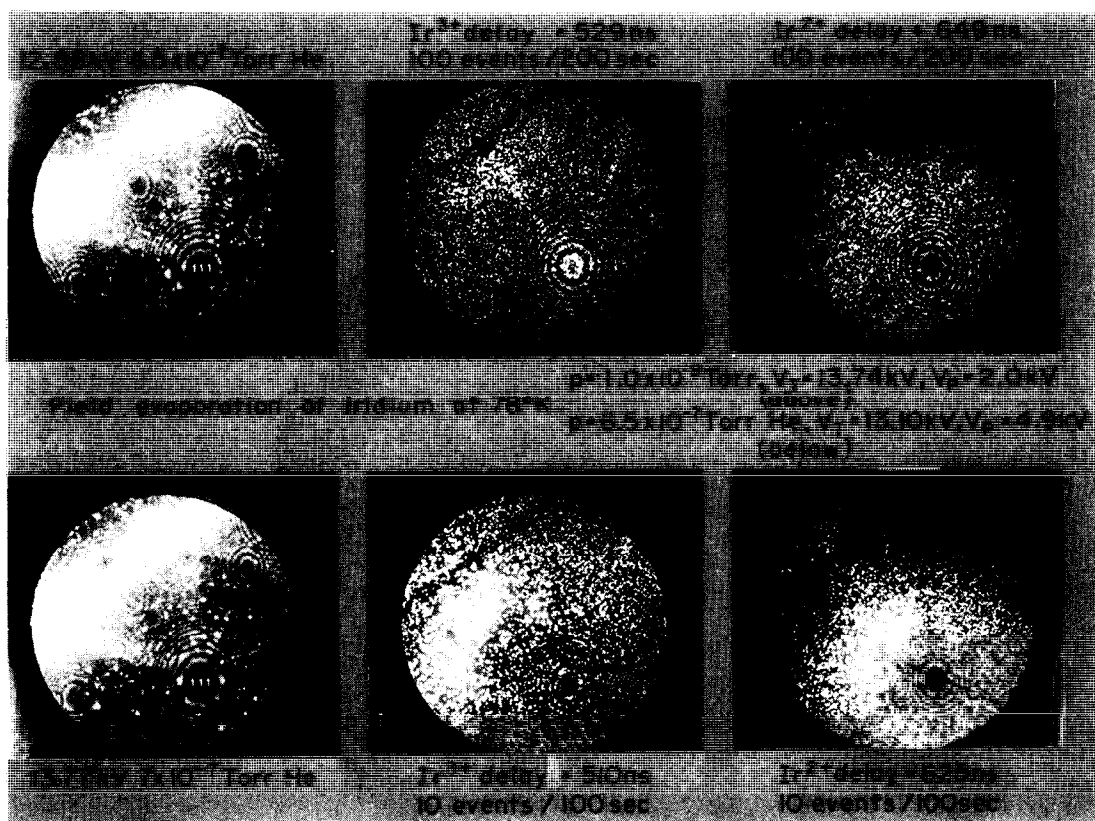


FIG. 34. A sequence of field evaporated, monolayer desorption images of iridium, time gated for each of the two dominant metal species,  $\text{Ir}^{2+}$  and  $\text{Ir}^{3+}$ , at  $78^\circ\text{K}$  in vacuum ( $1 \times 10^{-9}$  Torr) and in helium ( $6.5 \times 10^{-7}$  Torr).

randomization, in this case, may be due to the lower pressure of helium used during imaging, which would lower the degree of helium coverage on the surface between desorption events. Nevertheless, the observed randomization of the ring structure of low-index planes, observed during desorption of helium covered surfaces (Figs. 33 and 34), supports the hypothesis of metal atom migration prior to desorption *at least on low index planes*. However, this evidence for migration is not entirely conclusive, since it can be argued that the presence of field adsorbed helium at kink-site positions may cause an unavoidable alteration of metal ion trajectories by changing the local field configuration, independent of any surface migration which may occur.

Although the observation of the deflection of metal ions away from the center of the low index planes can be qualitatively described in terms of directed migration prior to evaporation, the reason for prominent ring structure in these regions has not been addressed. The effect must be due to the dynamic superposition, during multilayer imaging, of the annular regions of high ion density, which are observed during the collapse of low-index planes in high gain submonolayer desorption micrographs. But, if the individual submonolayer micrographs of Fig. 25, for example, are photo-

graphically superimposed to simulate a portion of the desorption sequence recorded in a multilayer micrograph, no ring structure is observed, although a dark region in the center of the (110) plane is seen. This may imply that a rapid rate of evaporation must be established in order to observe the ring structure, or simply that many more layers than represented by the desorption sequence of Fig. 25 must be superimposed.

The second striking feature of multilayer desorption micrographs (seen, for tungsten, in Fig. 30 and, to a lesser degree, in Fig. 29) is the appearance of a network of dark lines intersecting the image. Such structure, first reported by Waugh and coworkers,<sup>(43,44)</sup> and Moore and Spink,<sup>(45)</sup> form a pattern which appears to be characteristic of a particular metal rather than a particular crystal structure. For some metals, additional structure composed of bright intersecting lines (suggestive of increased ion density) is observed. For example, Fig. 35 shows a characteristic multilayer desorption image of platinum and Fig. 36 the corresponding field-ion image of the tip surface. Although Waugh *et al.*<sup>(48)</sup> have also chosen to explain the bright and dark lines in terms of directed surface migration, the dark regions are relatively unaffected by the presence of adsorbed helium (see Figs. 33 and 34). This suggests that another

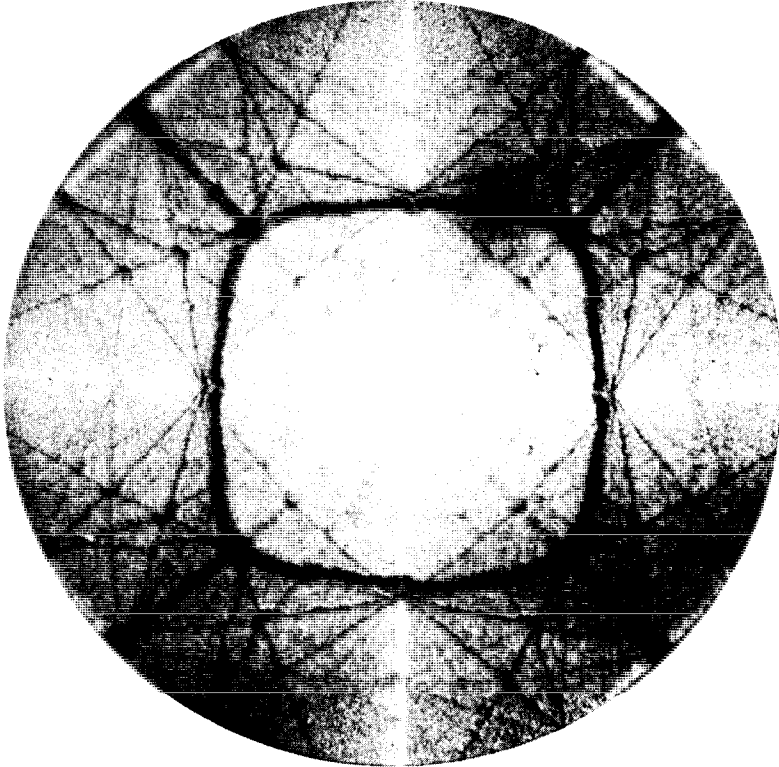


FIG. 35. A non-gated multilayer desorption micrograph of platinum taken at 21°K in high vacuum. Figure courtesy of S. V. Krishnaswamy, M. Martinka and E. W. Müller, Pennsylvania State University, University Park, Pennsylvania.

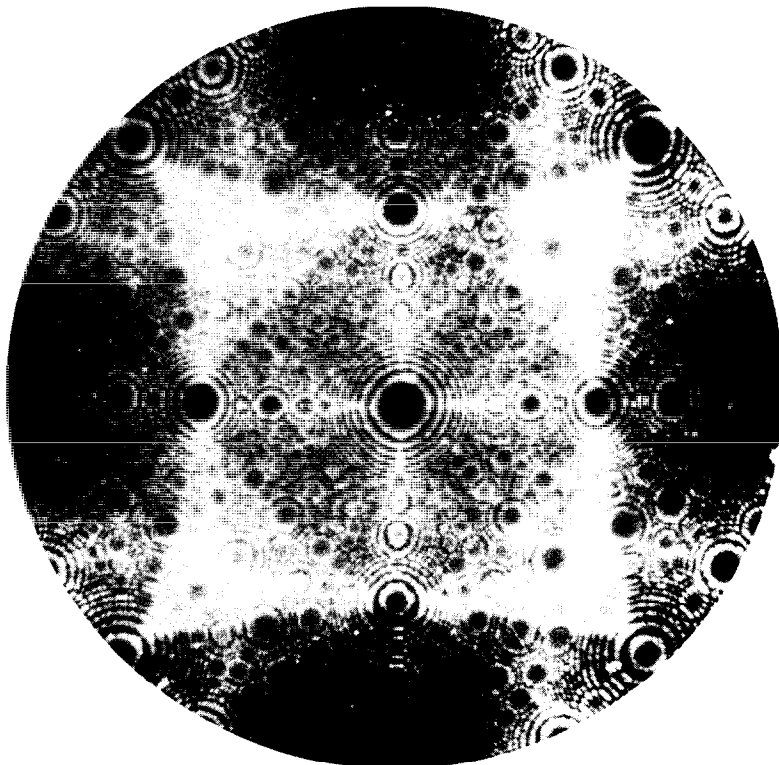


FIG. 36. The corresponding helium ion image of the tip of Fig. 35. Figure courtesy of S. V. Krishnaswamy, M. Martinka and E. W. Müller, Pennsylvania State University, University Park, Pennsylvania.

mechanism may dominate within these regions. For example, Krishnaswamy *et al.*<sup>(51)</sup> have assumed that the regions of the image in which there is a variation in ion density are caused by ion trajectory variations resulting from the polyhedral topography of the real tip surface. In such a view, depicted schematically in Fig. 37, bright lines in the desorption image are thought to be due to focusing by straight rows of atoms across prominent zones, whereas dark lines are interpreted as defocusing above geometric ridges between adjacent crystal facets. This explanation, which ignores the crystal structure of the lattice and concentrates on the multi-faceted nature of the real tip surface includes a more realistic description of actual tip morphology than the usual first order description of a smooth hemispherical tip from which exact radial projection of ions is expected. Since this explanation interprets all ion trajectories as being determined by local lattice morphology, desorption images of adsorbed species should also mirror the variations in ion density observed for metal lattice atoms. This is clearly shown in high-field desorption images of field-adsorbed noble gases,<sup>(52)</sup> where the characteristic multilayer pattern of low ion yield in the (111) region of tungsten (Fig. 38, top left) is reproduced in the desorption images of neon (Fig. 38, top right) and helium (Fig. 38, bottom left) at 5.7 V/Å. However, it is surprising that in general a decrease in ion density in one region is never complemented by an increase in ion density in an adjacent region, since ions defocussed from one region would be expected to increase the spot density somewhere else in the image. Similarly, desorption images which show highly localized

regions of increased ion density (for example, the bright lines of Fig. 35) never show a corresponding localized decrease in ion density in adjacent regions, although species are presumably focussed from one region to produce the observed increase in ion density in an adjacent region.

In order to test the validity of the ion focussing assumption, Krishnaswamy *et al.*<sup>(51)</sup> recorded multilayer field desorption images of metal lattices and field-ion images of the same lattice while it was field-evaporating (Fig. 39). They argued that both images should be qualitatively similar if focussing was a dominant mechanism, since both images are produced by ion projection from the same polyhedral tip shape. Recognizing that the ion image contained the additional confusing effects of inhomogeneous local gas supply and ionization probability, they proceeded to superimpose the locations of individual desorbed lattice atoms obtained directly from successive, individual field-ion micrographs in an evaporation sequence<sup>(51)</sup> (Fig. 40). The results of these measurements, clearly show the importance of focussing effects, and strongly support their interpretation of the origin of the main features of multilayer desorption images.

However, in all probability, several mechanisms will operate simultaneously to produce an actual multilayer desorption image.<sup>(53)</sup> For example, focussing and defocussing adequately explain the main features of the localized variations in ion density which are observed, i.e. bright and dark lines, whereas directed migration can help to explain the ring structure around low index planes, and perhaps even the lack of complementary structure in

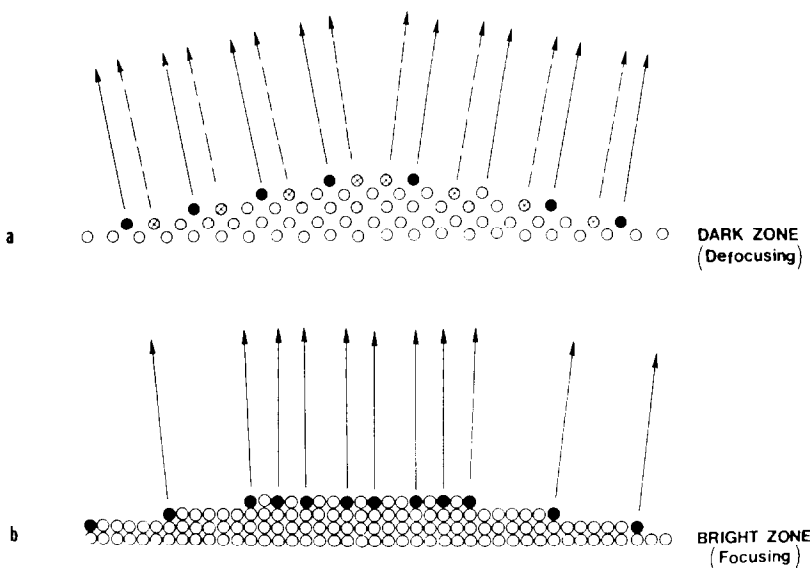


FIG. 37. (a) "A schematic diagram of the (postulated) defocussing of ion trajectories by a geometric ridge between adjacent crystal facets." (b) "A schematic representation of the (postulated) ion focusing effect above a straight atomic row across a prominent bright zone." Figure and caption (except portions within brackets) courtesy of S. V. Krishnaswamy, M. Martinka and E. W. Müller, Pennsylvania State University, Department of Physics, University Park, Pennsylvania.

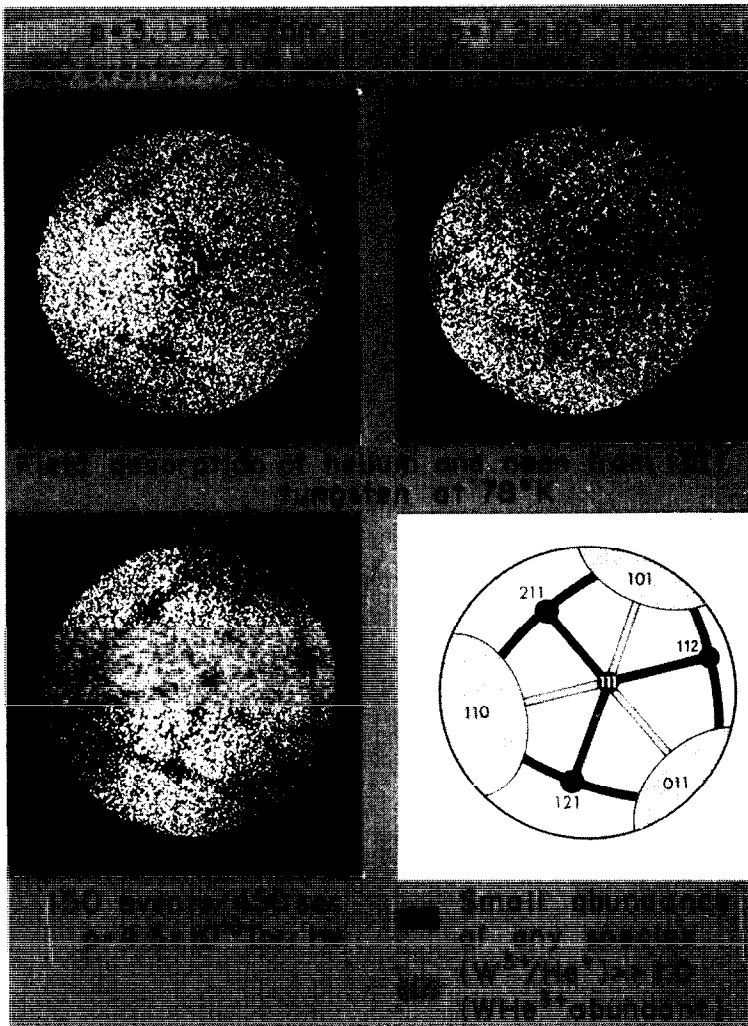


FIG. 38. Field desorption of helium and neon from (111) tungsten at 78°K. Top left: multilayer image of  $W^{3+}$  at  $4 \times 10^{-10}$  Torr. Top right: Image obtained by gating for  $Ne^+$  while evaporating the lattice in  $7.2 \times 10^{-10}$  Torr of neon. Bottom left: Image obtained by gating for  $He^+$  while evaporating the lattice in  $4.3 \times 10^{-10}$  Torr of helium. Bottom right: Interpretation of the previous images in which the inference of an abundant  $WHe^{3+}$  species in the (110), (011) and (101) regions and along major (shaded) crystallographic zones has been made (see Ref. 60). Both (field) adsorbed gas images display the same regions of low ion yield as does the  $W^{3+}$  image.

regions adjacent to those which display focussing effects.

Although the exact mechanism which produces the local variations in ion density is of intrinsic interest, it is not usually of practical importance in Imaging Atom-Probe mass spectroscopy, simply because the composition of each atom layer is averaged over a large spatial area of the surface. However, when an apertured photomultiplier is used to obtain the identity of species within a highly localized region of the surface,<sup>(5)</sup> the intrinsic ion yield must be considered. Similarly, the intrinsic variation in ion density must be considered<sup>(52)</sup> in conventional Atom-Probe analysis, where a small probe-hole limits the area of the tip surface which is examined. It will probably be necessary to reexamine the conclusions of previous Atom-Probe studies, undertaken at high desorption fields,<sup>(54)</sup> in which the intrinsic ion yield

of the substrate was not explicitly considered. For example, the studies in which atom-probe microscopy "identified" the invisible species in field-ion images of Pt<sub>3</sub>Co as cobalt.<sup>(55,56)</sup>

### 5. Depth Profile Analysis

The ability to identify the species contained within a single atomic layer of the substrate, while the substrate is dissected, layer by-atomic layer, is a unique capability of Atom-Probe analysis. All other depth profiling techniques either lack the depth resolution necessary to distinguish species within adjacent atomic layers, or have no reliable way of determining, in an absolute fashion, the depth penetrated. In addition, other techniques may not be able to detect species within the first few hundred angstroms of the surface, or not be able to detect many species of practical interest, such as hydrogen and helium, regardless of their location.

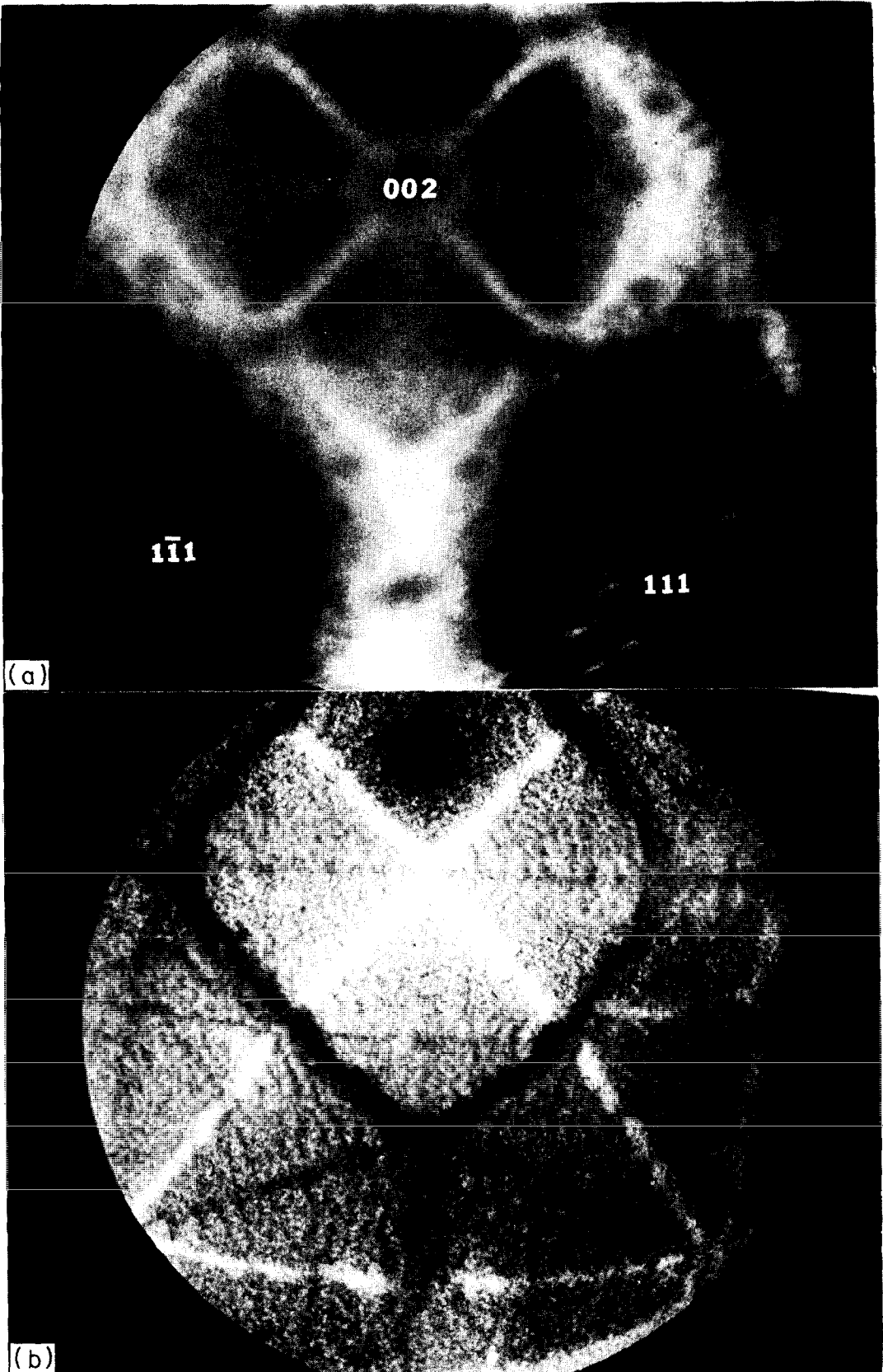


FIG. 39. (a) "A multilayer field-ion image of an evaporating iridium tip, fifteen layers of (002) at 78°K, showing persistent rings around the low index poles." (b) "A multilayer field-desorption image of the same Ir tip." Figure and caption courtesy of S. V. Krishnaswamy, M. Martinka and E. W. Müller, Pennsylvania State University, Department of Physics, University Park, Pennsylvania.

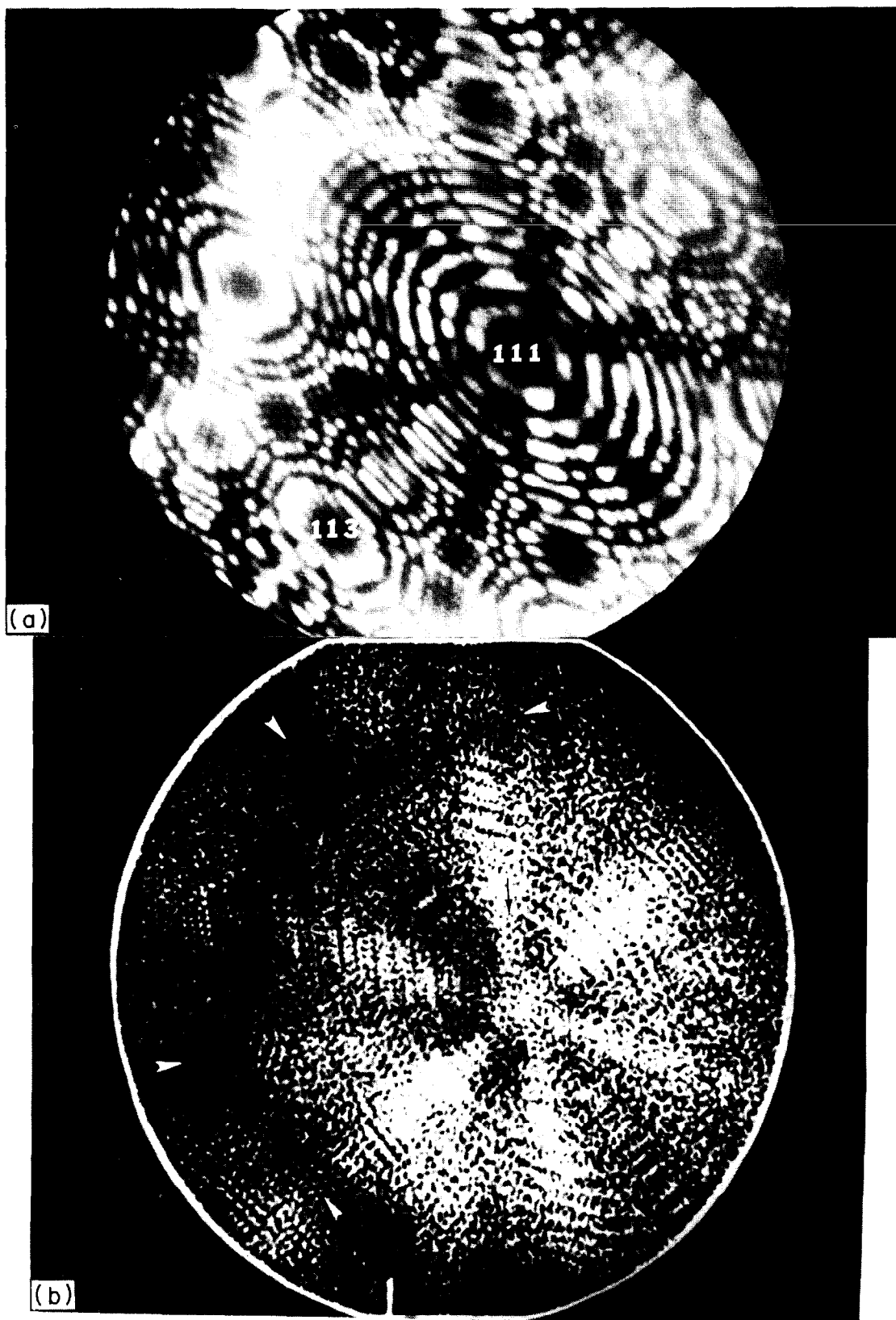


FIG. 40(a-b).

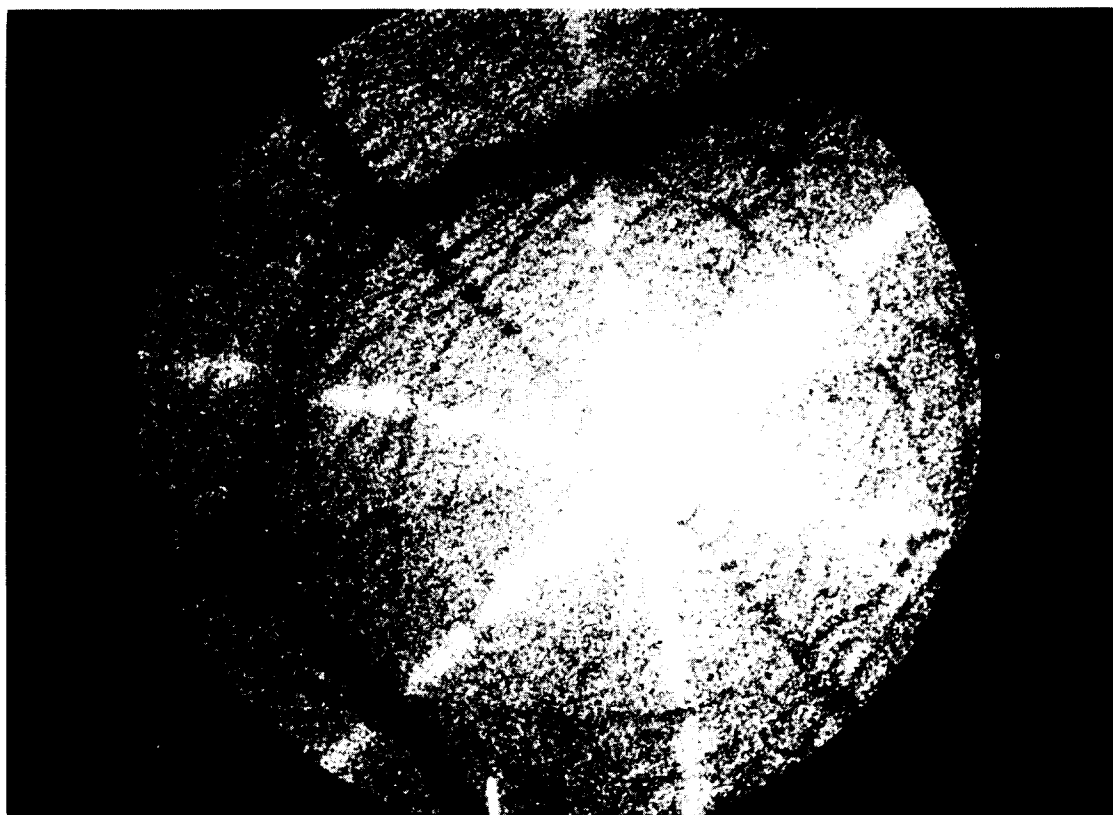


FIG. 40(c).

FIG. 40. (a) "He field-ion micrograph, 5.8 kV at 21K, of the (111) oriented Ir surface used." (b) "Simulated multilayer desorption pattern of the tip shown in (a), thirteen layers of the (111) plane evaporated from 6.8 to 8.0 kV." (c) "An actual multilayer desorption pattern of the Ir tip of (a), fifteen layers of the (111) plane evaporated at 9.5 kV." Figure and caption courtesy of S. V. Krishnaswamy, M. Martinka, and E. W. Müller, Pennsylvania State University, Department of Physics, University Park, Pennsylvania.

Despite the advantages of Atom-Probe analysis in obtaining near surface depth profiles, there are two major disadvantages: (1) only species within a very small area of the surface, typically 8000 square angstroms, can be examined, and (2) only species within a very limited depth from the surface can be examined. The consequences of the first limitation are fairly obvious, i.e. results may not be typical of macroscopic sized areas. To understand the second limitation, it must be emphasized that Atom-Probe analysis is destructive in that it removes substrate material during the analysis. As a result, the specimen radius can change substantially between the start and finish of a depth profile experiment. As the radius increases, the specimen potential must be increased, in order to preserve the required evaporation field of the substrate. But an increase in specimen potential means an increase in the kinetic energy of the desorbed species, and a corresponding decrease in the difference in arrival time of two consecutively arriving species at the CEMA. When this time difference becomes too small, the two species cannot be resolved, and the experiment may have to be terminated. If one asserts that all low-Z

species must be resolveable in an Imaging Atom-Probe experiment, and considers a conservative, minimum resolvable time separation of 20 nsec, a maximum tip potential of 16 kV is indicated by Table 2. This corresponds to a maximum tip radius of 690 Å.<sup>(57)</sup> In practice, a maximum specimen potential of 20 kV can often be achieved without a significant loss in resolution for most low-Z species, corresponding to a maximum useable tip radius of about 900 Å.

The maximum depth which can be probed is the difference between the final and initial tip radius, where the latter is determined by ease of tip fabrication and a desire to examine a reasonably large surface area. Conservatively, an initial radius of 230 Å (corresponding to a tip potential of 6 kV) is easily achieved, although 150 Å (4 kV) tips can sometimes be obtained. Figure 41 shows, schematically, a cross section view of a tip. As can be seen, the maximum depth which can be probed lies somewhere between 400 and 700 Å depending upon specific experimental conditions.

Figure 41 also shows that the surface area examined in the Imaging Atom-Probe will

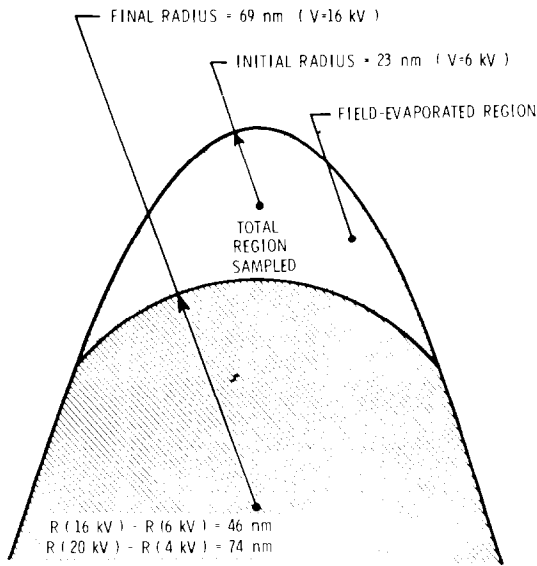


FIG. 41. A schematic, cross section view of a tip showing a change in radius as a result of field evaporation. The constraints on the initial and final tip radius are given in the text. The region sampled in the Imaging Atom-Probe increases in area as the tip radius increases because the detector-tip geometry is constant.

constantly increase as the tip radius increases, because the detector subtends a constant solid angle with respect to the tip. Although the surface area (and the number of surface atoms) examined will increase, the crystallographic region viewed at the CEMA will remain constant. This occurs because the angular separation of crystallographic features on the tip surface are, themselves, a constant. The increase in surface area during a profile experiment is a complication, because it will contribute to the observed abundance of species within successive layers. For example, if one assumes that the detector is centered on the (001) plane of tungsten, and the (112) plane appears at the edge of the imaged area, the linear distance on the surface from edge-to-edge of the imaged area will increase by 490 Å as the radius of the tip is increased. Ultimately, the increasing number of species examined as the tip radius becomes larger will adversely affect the statistics of the depth distribution, particularly if only a few implanted species are present in each layer. As a result, the maximum acceptable increase in tip area will ultimately limit the maximum change in tip radius that can be tolerated.

One final difficulty with Imaging Atom-Probe depth profiling must be mentioned. If the implanted species happens to form a stable molecular compound with a lattice atom which, in turn, does not dissociate during field desorption, the number of implanted species detected in each layer will be smaller than the number actually implanted. If the mass resolution of the spectrometer is not sufficient

to allow these molecular species to be unambiguously identified, the depth profiles which are obtained, as well as any information extracted from them, will be inherently inaccurate. For example, in high fields helium has long been known to form stable metal-helide molecular ions<sup>(58)</sup> with most metals, and, as a result, unambiguous helium depth profiles are very difficult to obtain. This is particularly true, since the formation of metal helides is known to depend on several parameters, including substrate temperature<sup>(59)</sup> and the magnitude of the applied field.<sup>(28)</sup>

As an illustration of the profiling technique, the results of a previously published study of deuterium implanted into tungsten<sup>(60)</sup> will be reviewed. The tungsten-deuterium system is attractive, because tungsten hydrides have never been observed in any atom-probe study. Presumably, therefore, tungsten deuterides will not form under high-field conditions so that complications due to molecular ion formation can be neglected. In an initial experiment,<sup>(60)</sup> 80 eV deuterium ions were implanted into a (110) tungsten specimen with a flux sufficient to insure that the ratio of surface tungsten atoms to deuterium ions was approximately 1:1. Since the energy transferred to a tungsten atom by an incoming deuterium atom (the ion will be neutralized with high probability near the surface) is not sufficient to induce lattice damage, the structure of the tungsten lattice will remain unchanged after implantation. *In situ* implantation at 300°K was carried out in the source chamber of Fig. 2. Using the "first layer" composition analysis techniques described previously, the surface layer of the tungsten specimen was characterized before and after implantation. Fig. 42 shows the resulting composite histograms. Three features are immediately ob-

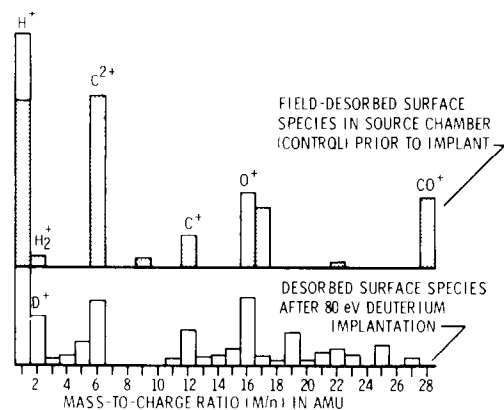


FIG. 42. A "first layer" composition histogram, obtained by the techniques described in the text, before and after implantation of a (110) tungsten specimen with 80 eV deuterium ions at 300°K. Each histogram gives the relative abundance of species residing on the first layer of the specimen. The upper histogram is a "control" showing the species which are present on the surface in the absence of deuterium ion implantation.

vious. First, a surface CO contaminant, appearing when no implantation occurred, disappears after implantation of the tip, although no change in the relative abundance of  $m/n = 12$  ( $C^+$ ) or  $m/n = 16$  ( $O^+$ ) is observed. Since  $C^+$  and  $O^+$  are characteristic fragment species of CO in field-desorption mass spectroscopy, their unchanged abundance implies that surface CO, missing after implantation, has not simply dissociated into surface carbon and oxygen. Although the missing CO could desorb from the surface by acquiring the necessary activation energy from a collision with an implanting deuterium ion, another explanation can be advanced based on the depth profiles to be discussed shortly.

The second feature of Fig. 42 is the presence of a species at  $m/n = 6$ , identified as  $C^{2+}$  (and characteristic of organic carbon contamination of the tip), which is greatly reduced in abundance after implantation.

The third feature of Fig. 42 is the small abundance of  $m/n = 2$  before implantation, due to  $H_2^+$ , and the much larger abundance of  $m/n = 2$  after implantation due, presumably, to  $D^+$ . The increase of the  $m/n = 2$  species after implantation implies that a significant amount of deuterium resides on the surface after implantation. This surface build-up is not surprising since it is highly probable that some of the implanting ions will have energies much lower than the nominal 80 eV and will, therefore, not penetrate into the lattice.

If the lattice is field evaporated layer-by-layer, the abundance of each species within each layer can be plotted as a function of the number of layers removed. This is the depth profiling technique discussed in §3, in which the number of layers removed is monitored in this instance by observing successive collapses of the (110) plane in the non-gated desorption image. The result for one of several 80 eV deuterium implantation experiments carried out at 300°K is shown in Fig. 43.

The first thing to notice from this figure is that the abundance of  $m/n = 13$  ( $C^+$ ) and  $m/n = 16$  ( $O^+$ ) each decrease from the surface and disappear after approximately ten atomic layers of the lattice have been removed (corresponding to a depth of 22.3 Å). Second, a species with  $m/n = 6$  ( $C^{2+}$ ), which appears close to the surface, disappears after ten layers have been evaporated. The  $C^+$  and  $O^+$  species seen during the depth profiling strongly suggest that the "missing" surface CO was recoil implanted into the tungsten. Likewise, the  $C^{2+}$  profile suggests that the decrease in the abundance of this species on the surface after implantation results from recoil implantation of this contaminant. Interestingly, the maximum depth observed for these species is too great if one thinks of the tungsten tip as an amorphous solid, but if channelling<sup>(61)</sup> is assumed (following a collision between the surface species and an incoming deuterium ion) the depth observed can be qualitatively explained.<sup>(62)</sup> It should be noted, however, that the

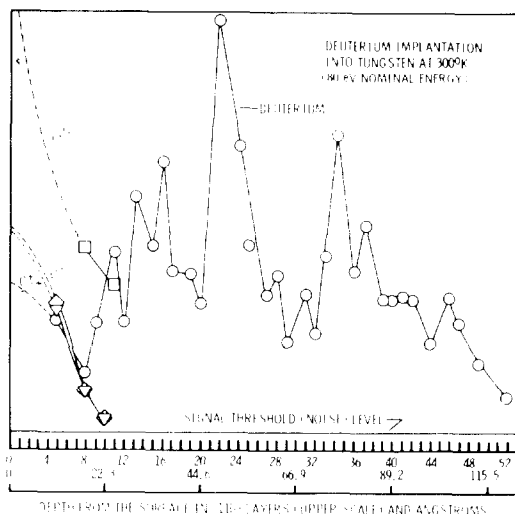


Fig. 43. Depth profiles of  $m/n = 2, 6, 12$  and  $16$  observed during a field-evaporation sequence into (110) tungsten after implantation with deuterium ions of 80 eV nominal energy. A signal threshold (or noise) level is also plotted, which corresponds to the signal level of  $m/n = 2$  observed prior to implantation in Fig. 40, due to  $H_2^+$  desorbing from the surface.

observed implantation of carbon and oxygen could have resulted from low energy contaminants in the ion source, whose beam was not mass filtered.

The third, striking feature of Fig. 43 is the wide, structured,  $m/n = 2$  distribution, associated with the implanting deuterium. Surprisingly, the distribution seems to contain two maxima at twenty-two and thirty-four (110) layers. If channelling of the deuterium is assumed, following a loss of energy by collision with surface carbon or oxygen atoms, the maximum extent of an 80 eV distribution should lie between twenty and thirty atomic layers from the surface. However, the distribution of Fig. 43 extends to at least 120 Å. This, and the two maxima, suggest that the incoming beam had two primary energies, which result in two overlapping depth distributions, each peaking at the nominal energy of an individual component. Although the implantation source was not mass analyzed, subsequent analysis disclosed that it did consist of two components, ionic and neutral, with the neutral component having a nominal energy consistent with the distribution of Fig. 43.

The sharply peaked structure of the deuterium distribution was also unexpected, but can be predicted with reasonable accuracy,<sup>(62)</sup> if the crystallographic structure of the surface region probed is considered in detail. Although the exact form of a calculated distribution will depend upon many parameters, a sharply peaked structure will result if deuterium is allowed to selectively dechannel into preferred crystallographic regions of the tip at well defined depths from the surface.<sup>(62)</sup>

The recoil implantation of surface species

suggested by the above interpretation of the data of Figs. 42 and 43 is particularly exciting because it is the first, direct indication of a phenomena which is of great practical importance. For example, transistor manufacturing techniques employ ion implantation to selectively dope semiconductors for optimum electrical characteristics. Often this implantation is performed through an oxide layer on the surface, which has been considered to be a "passivating" barrier between the semiconductor and the ambient environment. But the electrical characteristics of the devices implanted in this manner are often observed to be less than optimum, perhaps because of recoil implantation of an oxide impurity into the near surface region. The Imaging Atom-Probe technique offers the hope of direct observation, and quantification, of this effect.

### 6. Future Applications

It is clear that the depth profiling capability of the Imaging Atom-Probe is an application of the technique which can be extended to a wide range of problems of practical interest. However, it is not the only application which can be envisioned, particularly since the imaging capability of the instrument has hardly been explored. Consider, for example, possible applications of the Imaging Atom-Probe to problems of metallurgical interest.

A knowledge of the composition of small precipitate particles in metal alloys is of great interest, because of their effect on the structural and mechanical properties of the solid. Since precipitate particles cannot be observed by electron microscopy when they are less than 30 Å in extent, Field-Ion microscopy becomes the only available tool for observing the early stages of precipitate growth. Recognizing this fact, several experiments were performed by Brenner and Goodman<sup>(63,64)</sup> and others,<sup>(65-67)</sup> which combined low temperature Field-Ion and Atom-Probe microscopy to determine the size and composition of individual precipitate particles. However, because of the small probe hole which the Atom-Probe utilizes, only one precipitate particles composition could be determined at a time. Furthermore, since the field-desorption process destroys the specimen, and the number of precipitate particles is limited, only a few particles could actually be examined within each specimen. With the Imaging Atom-Probe, a much larger area of the specimen can be examined at one time and, following a determination of average composition, the two dimensional distribution within each atomic layer of a species of interest can be determined by selective time-gating. Since each desorption event applied to the specimen probes deeper into the near surface region, a complete three dimensional distribution of the selected species can be obtained. For example, Fig. 44 shows an integrated field-desorption image of a copper-I atomic per cent Iron alloy

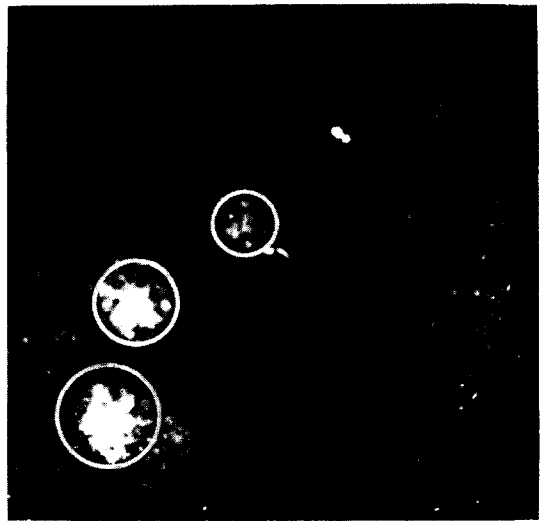


FIG. 44. Integrated field-desorption image (1000 evaporation pulses) of a Cu-1 at% Fe alloy aged for 150 min at 550°C, gated for Fe<sup>2+</sup>. The single image spots show the distribution of Fe in a Cu-layer of about 250 Å; the large circled areas shown Fe-precipitates. ( $V_{DC} = 8.2$  kV;  $V_{pulse} = 0.9$  kV). Note: The dark circular area in micrograph where no image spots are seen is an instrument artifact. Figure and caption courtesy of R. Wagner, The University of Göttingen, Institute of Metal Physics, Göttingen, Germany.

gated for Fe<sup>2+</sup>, obtained by Wagner, Pilliar and Brenner<sup>(68)</sup> in a novel instrument combining conventional Atom-Probe and Imaging Atom-Probe spectrometers.

Grain boundaries are structures of interest not only because they can affect the mechanical integrity of an otherwise perfect lattice, but because they may act as reservoirs for migrating impurities. Electron microscopy can be used to observe grain boundaries, but without the resolution necessary to determine the nature and extent of the transitional boundary adjacent to them. In fact, an early success of field-ion microscopy was the direct imaging of grain boundaries and the demonstration that on an atomic scale the ordered substrate lattice extended directly to them, without an amorphous transition region in between. By using the Imaging Atom-Probe, grain boundary studies can be extended to include direct visualization of impurity migration to the boundary after treating the specimen in some standard manner, e.g. heating in oxygen. By time-gating for the impurity of interest, its concentration gradient over the entire imaged area can be determined. The beauty of this method has recently been demonstrated by Waugh<sup>(69)</sup> who has obtained the first time-gated images of impurity segregation to a grain boundary by gating for oxygen in a molybdenum specimen (Fig. 45), a very impressive result.

The diffusion of gaseous species, such as hydrogen, into metallic solids is currently of interest, since the gas-solid system is a method of

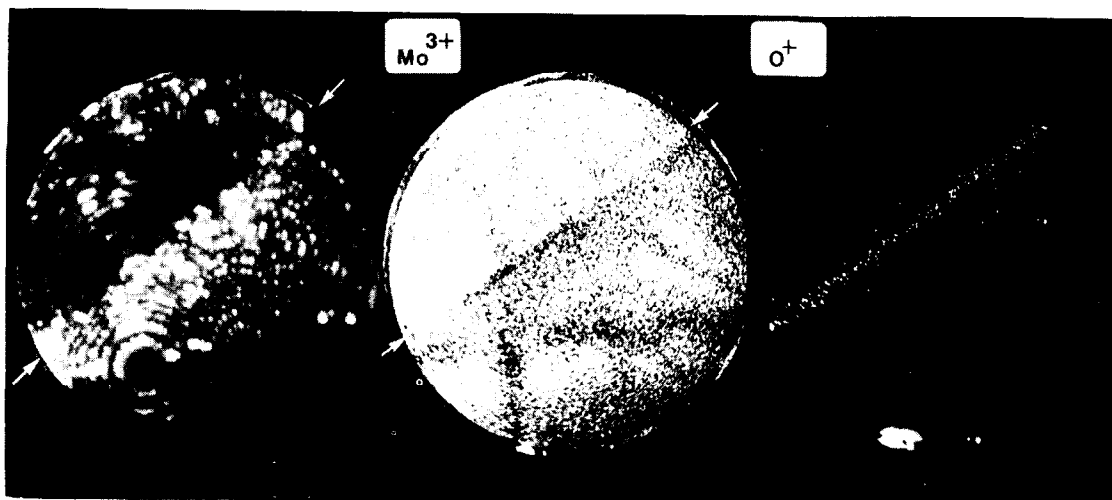


FIG. 45. "Field-ion,  $\text{Mo}^{3+}$  and  $\text{O}^+$  images from a molybdenum specimen containing a grain boundary (arrowed) at which segregation of oxygen has occurred. Some ten net planes were field-evaporated for the  $\text{Mo}^{3+}$  image and thirty for the  $\text{O}^+$  image. The majority of the  $\text{O}^+$  ions lie within a band of 1 nm width centered on the grain boundary." Figure and caption courtesy of A. R. Waugh and M. J. Southon, University of Cambridge, Department of Metallurgy and Materials Science, Cambridge, England.

storing energy (e.g. hydrogen produced by photoelectrolysis of water can be stored for future use as a metallic hydride). The Imaging Atom-Probe offers the possibility of observing the diffusion process on an atomic scale by selective time-gating for hydrogen following diffusion of hydrogen into the tip at a given temperature. Moreover, the effect of surface passivation layers (intentional, or unintentional as in the case of adsorbed residual gas) on the diffusion process can be directly determined.

In addition to problems of metallurgical interest, the Imaging Atom-Probe may have broad application in the area of surface chemistry. Since the imaged area of the specimen closely approximates the size of a catalyst granule, catalytic reactions can be followed in the Imaging Atom-Probe on specimens whose surface-to-volume ratio is near optimum. The reactivity of kink-site positions can, in principle, be directly observed by selective time-gating for reactants (and reaction products) following tip exposure in a reaction chamber. Changes in surface topography could be determined at low reaction rates, in an attempt to determine the initial conditions responsible for the preferential enhancement of certain crystallographic orientations observed in macroscopic experiments.<sup>(70)</sup> Since alloys can be examined in the Imaging Atom-Probe, it should also be possible to determine changes in the surface of alloy catalysts following induced catalytic activity with the chance of determining the location and identity of species at "active sites". Unfortunately, insulator catalysts cannot be examined, unless their electrical conductivity is large enough to permit the establishment of a desorption field in nanosecond time scales.

Finally, the virtually unexplored area of molecule-surface interaction can be addressed. By adsorbing simple molecules on field-evaporated substrates, whose structure has been determined by ion-imaging, information on the interaction of the molecule with the surface can be determined. Two different approaches may be fruitful. In the first, Imaging Atom-Probe spectroscopy can be used to mass analyze desorbed species as a function of surface temperature, coverage and orientation. For example, one finds<sup>(71)</sup> that chemisorbed benzene on (110) tungsten will desorb as  $\text{C}^+$ ,  $\text{H}^+$ ,  $\text{C}_2\text{H}_2^+$ ,  $\text{C}_3\text{H}_3^+$ ,  $\text{C}_4\text{H}_4^+$ ,  $\text{C}_5\text{H}_5^+$  or  $\text{C}_6\text{H}_6^+$  with relative abundances that depend on surface conditions. On the other hand, physisorbed benzene removed from condensed benzene layers at 78°K will always desorb as  $\text{C}_6\text{H}_6^+$ . The second approach involves time-gated imaging of a selected species to determine its position on the surface with respect to lattice species. For example, by gating for  $\text{C}^+$  in a chemisorbed benzene layer, a picture of the location of surface carbon can be obtained,<sup>(71)</sup> provided conditions can be established which assure total dissociation of the benzene molecule prior to desorption without rearrangement. Under favorable conditions, selective gating may even provide an "image" of the carbon ring in each adsorbed benzene molecule. This exciting possibility was recognized early in the development of the Imaging Atom-Probe-technique,<sup>(72)</sup> but the resulting images were disappointing. Although initially attributed to the diameter of carbon's "disk-of-confusion" at 78°K, it now appears that several other factors, including surface orientation and coverage, may have been primary constraints on image quality. Perhaps when such parameters are characterized in detail, successful

images of the spatial distribution of the atomic constituents of small molecules will be obtained. But regardless of the ultimate success of molecular imaging, Imaging Atom-Probe analysis promises a wealth of information on fundamental molecule-surface interaction.

Further extension of the time-gating technique to "image" large biological molecules is another exciting possibility, either by high field-desorption of molecular fragments or laser-induced desorption of selected constituent atoms.<sup>(73)</sup> The author sees no obvious reason why the Imaging Atom-Probe, using laser-induced desorption, for example, should not yield valuable information on the spatial distribution of species within large complex molecules, provided, that the molecule of interest can be placed on the tip apex, and the laser pulse does not induce thermal desorption of the entire molecule. Actually, laser induced desorption should have an additional benefit in Imaging Atom-Probe spectroscopy in that it may provide improved mass resolution during time-of-flight mass spectroscopy of desorbed species.<sup>(74)</sup> Upon laser induced desorption, surface species would be expected to encounter a constant d.c. potential sufficient to accelerate them to the CEMA. Since the high-voltage pulse normally required for desorption would no longer be necessary, the energy spread of the desorbing ions associated with the electrical pulse shape would be absent, and mass resolution should increase appreciably.

### References

1. E. W. MÜLLER, *J. appl. Phys.* **27**, 474 (1956).
2. E. W. MÜLLER, *Naturwiss.* **29**, 533 (1941).
3. *Field evaporation* is a term applied specifically to the removal of *lattice atoms* (as positive ions) in a high electric field at temperatures usually below one-half of the melting temperature of the substrate. Field evaporation is a specific case of *field desorption*, a process which describes the field-induced removal of any substrate species.
4. The "Imaging Atom-Probe" is a descriptive title for the author's instrument, suggested by A. J. WAUGH of the University of Cambridge, Cambridge, England.
5. J. A. PANITZ, *Rev. scient. Instrum.* **44**, 1034 (1973).
6. The possibility of a time-gated desorption microscope was mentioned by E. W. MÜLLER and R. J. WALKO in an abstract of a paper presented at the *19th Field Emission Symposium* (Erbana, Ill., 1972) but no instrument details or data were presented.
7. J. A. PANITZ, *J. Vac. Sci. Technol.* **11**, 206 (1974). U. S. Patent No. 3,868,507 (February 25, 1975).
8. E. W. MÜLLER, J. A. PANITZ, and S. B. McLANE, *Rev. scient. Instrum.* **39**, 83 (1968).
9. R. GOMER, *J. chem. Phys.* **31**, 341 (1959).
10. R. GOMER and L. W. SWANSON, *J. chem. Phys.* **38**, 1613 (1963).
11. L. W. SWANSON and R. GOMER, *J. chem. Phys.* **39**, 2813 (1963).
12. D. G. BRANDON, *Br. J. appl. Phys.* **14**, 474 (1963).
13. T. T. TSONG, *J. chem. Phys.* **54**, 4205 (1971).
14. R. J. WALKO and E. W. MÜLLER, *Phys. Status Solidi* (a) **9**, K9 (1972).
15. This is the so-called *image force* model of field desorption introduced by E. W. MÜLLER in 1956 (Ref. 1).
16. P. A. REDHEAD, *Vacuum* **12**, 203 (1962).
17. As the tip voltage is increased, a field,  $E_{\text{evap}}$ , will be established where removal of lattice atoms becomes highly probable. At such a field strength, field evaporation will continue until the tip radius has increased so as to lower the average field below  $E_{\text{evap}}$ . At this point, field evaporation will cease and the surface atoms will assume a stable configuration or "end form" at the applied tip voltage.
18. J. A. PANITZ, Ph.D. Dissertation, Pennsylvania State University, University Park, PA, 1969.
19. J. A. PANITZ, Sandia Laboratory report No. SAND75-0117, Sandia Corporation (Albuquerque, NM), 1975.
20. S. V. KRISHNASWAMY and E. W. MÜLLER, *Rev. scient. Instrum.* **45**, 1049 (1974).
21. R. S. CHAMBERS, Ph.D. Dissertation, University of Illinois at Urbana (Urbana, IL), 1976.
22. CERAMASEAL, New Lebanon Center, New York, Part No. 807B 7589-1.
23. SPRAGUE ELECTRIC COMPANY, High voltage "door-knob" capacitor, 500 pF 30 kVd.c., part No. 30DK-T5.
24. J. A. PANITZ and R. J. WALKO, *Rev. scient. Instrum.* **47**, 1251 (1976).
25. R. GOMER, *Field Emission and Field Ionization* p. 30. (Harvard U. Press, Cambridge, MA, 1961).
26. The author wishes to acknowledge the contributions of Mr. J. ABRAHAM and Mr. R. PIERLE, formerly of Galileo Electrooptics (Sturbridge, Mass.), who developed the technique which produces the spherically curve CEMA plates.
27. CARPENTER TECHNOLOGY CORPORATION, Reading, Pennsylvania.
28. E. W. MÜLLER and T. T. TSONG, *Prog. Surf. Sci.* **4**, 50 (1973).
29. J. A. PANITZ and J. A. FOESCH, *Rev. Scient. Instrum.* **47**, 44 (1976).
30. The time-gated desorption microscope was mentioned by MÜLLER (Lab. Practice **22**, 412 (1973)) along with the "impossibility" of achieving "acceptable" mass resolution in such an instrument.
31. E. G & G Inc., Salem, MA, part No. KN-22.
32. National Semiconductor's "Damm-Fast" operational amplifier, LH0063.
33. J. A. PANITZ, Sandia Laboratory report No. SAND75-0116, Sandia Corporation (Albuquerque, NM), 1975.
34. J. A. PANITZ, S. B. McLANE and E. W. MÜLLER, *Rev. scient. Instrum.* **40**, 1324 (1969).
35. J. A. PANITZ, *CRC Critical Rev. Sol. State Sci.* **158** (1975).
36. The tip is usually pulsed several times (and the resulting spectra added) before raising the d.c. bias. This insures that all species characteristic of this particular desorption field will be removed.
37. Usually the lattice is field evaporated prior to this type of experiment at some potential ( $V_{\text{dc}} + V_p$ ). The height of the mass peak corresponding to a dominant lattice species is monitored, and pulse evaporation is continued until the signal drops below the noise level of the system. At this point, the tip is assumed to have reached a stable voltage "end form", so that evaporation at some lower potential,  $V_m$ , would not be expected to cause field evaporation.
38. E. W. MÜLLER and T. T. TSONG In: *Field-Ion Microscopy: Principles and Applications* p. 169 (Elsevier, New York, 1969).
39. For ideal case of exact radial projection,  $\beta = 1.0$ . In practice,  $1.0 < \beta < 3$ .
40. Provided, of course, that short range migration of species on the surface (immediately prior to desorption) and focussing of the desorbing species into specific crystallographic directions can be ignored. It

- will be shown later that, although this may be the case at low desorption fields, at high fields (approaching the evaporation field of the lattice) such effects cannot be ignored.
41. E. W. MÜLLER *Adv. Electronics Electron Phys.* **13**, 118 (1960).
  42. Reference 38, p. 155.
  43. A. R. WAUGH, E. D. BOYES, D. A. COPPELL, A. J. WATTS and M. J. SOUTHON, *21st Field Emission Symposium*, Marseille, 1974.
  44. A. R. WAUGH, E. D. BOYES, and M. J. SOUTHON, *Nature* **253**, 342 (1975).
  45. A. J. W. MOORE and J. A. SPINK, *21st Field Emission Symposium*, Marseille, 1974.
  46. However, they may be due to secondary electrons from a distant ion impact at the CEMA. Because of the ambiguity introduced by this possibility, other consequences of these image spots will not be discussed further.
  47. S. S. BRENNER and J. T. MCKINNEY, *Surf. Sci.* **23**, 88 (1970).
  48. A. R. WAUGH, E. D. BOYES and M. J. SOUTHON, *Surf. Sci.* **61**, 109 (1976).
  49. E. W. MÜLLER, *Surf. Sci.* **2**, 484 (1964).
  50. Because of the width of the gate pulse, this image may contain (in addition to evaporated lattice atoms) image spots due to metal-helide molecular ions.
  51. S. V. KRISHNASWAMY, M. MARTINKA and E. W. MÜLLER, *Surf. Sci.* **64**, 23 (1977).
  52. J. A. PANITZ, *J. Vac. Sci. Technol.* **12**, 210 (1975).
  53. One mechanism which has never been considered in detail is the formation of neutrals during the desorption event. If such species were produced they might be expected to have very low energies and, consequently, may not be detected by the CEMA. Their effect would be the production of regions of apparently low ion density in the desorption image. A theoretical study of Auger or ion neutralization probability in high electric fields is needed, but unavailable at this time.
  54. Defined as the range of electric fields over which the substrate lattice is field-evaporating.
  55. T. T. TSONG, S. V. KRISHNASWAMY, S. B. McLANE and E. W. MÜLLER, *Appl. Phys. Lett.* **23**, 1 (1973).
  56. T. T. TSONG and E. W. MÜLLER, *J. appl. Phys.* **45**, 2367 (1974).
  57. The tip radius can be estimated by iterating Equation 50 at a field equal to the helium best image field,  $F = 4.5 \text{ V/\AA}$ , and  $d = 0.0005 \text{ m}$ . Obviously, this is only an approximation, but adequate for most purposes.
  58. E. W. MÜLLER, S. B. McLANE and J. A. PANITZ, *Surf. Sci.* **17**, 430 (1969).
  59. E. W. MÜLLER, S. V. KRISHNASWAMY and S. B. McLANE, *Phys. Rev. Lett.* **31**, 1282 (1973).
  60. J. A. PANITZ, *J. Vac. Sci. Technol.* **14**, 502 (1977).
  61. D. S. GEMMEL, *Rev. mod. Phys.* **46/1**, 129 (1974).
  62. D. K. BRICE, Sandia Laboratory report No. SAND 77-2052, Sandia Corporation, Albuquerque N.M. (1977).
  63. S. S. BRENNER and S. R. GOODMAN, *Scr. metall.* **5**, 865 (1971).
  64. S. R. GOODMAN, S. S. BRENNER and J. R. LOW, JR., *Metall. Trans.* **4**, 2371 (1973).
  65. A. YOULE, P. J. TURNER, and B. RALPH, *J. Microsc.* **101**, 1 (1973).
  66. P. J. TURNER and M. J. PAPAZIAN, *Met. Sci.* **7**, 81 (1973).
  67. P. J. TURNER, B. J. REGAN and M. J. SOUTHON, *Surf. Sci.* **35**, 336 (1973).
  68. R. WAGNER, J. PILLIAR and S. S. BRENNER, 24th International Field-Emission Symposium, Oxford, 1977.
  69. A. R. WAUGH, *24th International Field Emission Symposium*, Oxford, England, 1977.
  70. S. WONG, M. FLYTZANI-STEPHANOPOULOS, M. CHEN, T. E. HUTCHINSON and L. D. SCHMIDT, *J. Vac. Sci. Technol.* **14**, 452 (1972).
  71. J. A. PANITZ (unpublished data).
  72. J. A. PANITZ, *Am. chem. Soc.*, Chicago, Ill (1975).
  73. V. S. LETOKHOV, *Physics Today* **305**, 23 (May, 1977).
  74. T. T. TSONG, The Pennsylvania State University, University Park, PA (private communication).